Mechanisms of Spatio-Temporal Intermittency in Many-Body Systems

By

Guram Gogia

Advisor: Justin Clifford Burton, Ph.D.

An abstract of
A dissertation submitted to the Faculty of the
James T. Laney School of Graduate Studies of Emory University
in partial fulfillment of the requirements for the degree of
Doctor of Philosophy
in Physics

Spring, 2020

Abstract

Mechanisms of Spatio-Temporal Intermittency in Many-Body Systems

By Guram Gogia

Intermittent dynamics are ubiquitous in a wide variety of complex systems that are driven far from equilibrium. The most famous physical phenomenon that manifests intermittency is transitional turbulence in a pipe flow. The spatio-temporal patterns in wall-bounded flows that emerge at intermediate flow velocities have been a subject of active research for the last 140 years. In this thesis, I present a phenomenon that can serve as a many-body analogy to intermittent turbulence. Our findings relate how structural inhomogeneities and associated equilibrium properties can couple with external driving and give rise to novel spatio-temporal intermittent behavior.

Our research discovered that a dusty plasma crystal, made out of a few hundred microscopic colloidal spheres and under certain experimental conditions, continuously switches between crystalline and gas-like states. The switching persists over hours without changing any experimental conditions. Our findings led us on a two-fold path of investigation: one elucidating the origin of the spontaneous vertical oscillations and another characterizing the mechanism of emergent behavior.

Using single-particle experiments and accompanied numerical simulations, we found that the spontaneous vertical oscillations occur due to a delayed charging mechanism. These experiments also allowed us to characterize the plasma environment. Furthermore, our models let us calculate charging time for the microscopic particles in the plasma environment.

We performed molecular dynamics simulations, in which we disregarded plasma specific properties and found that emergent dynamics are a direct consequence of coupling between structural disorder arising from particle polydispersity and external dynamic conditions. More specifically, the particle polydispersity gives rise to localized vibrational modes, that are polarized in the vertical direction. These modes

are excited by external driving and the transfer of energy to other normal modes causes the system to melt.

With the intention of generalizing our findings, we modeled the orthogonal mechanical energies of the system using ODEs with both noise and coupling terms based on dynamical arguments. This surprisingly results in predator-prey-like interactions. The only non-dimensional number derived from our equations resembles the Reynolds number in fluid flow and accurately predicts where intermittent dynamics would be manifested.

Mechanisms of Spatio-Temporal Intermittency in Many-Body Systems

By

Guram Gogia
B.A., Colby College, Waterville, ME, 2014

Advisor: Justin Clifford Burton, Ph.D.

A dissertation submitted to the Faculty of the
James T. Laney School of Graduate Studies of Emory University
in partial fulfillment of the requirements for the degree of
Doctor of Philosophy
in Physics

Spring, 2020

Contents

List of Figures

Citations to Previously Published Work

Chapter 2 contains research from the following publication:

- *"The many faces of a Leidenfrost drop"*, **Guram Gogia**, Justin C. Burton, *Physical Review Letters*, **119 (17)**, 178004 (2015)

Chapter 3 contains research from the following pre-print:

- *"The origin of large amplitude oscillations of dust particles in a plasma sheath"*, Joshua Mendez, **Guram Gogia**, Bin Wu, Zachary Laseter and Justin C. Burton, *arXiv*, **1908.03138** (2019). Under review at *Physical Review Research*.

Chapter 4 and 5 contain research from the following pre-print:

- *"Intermittent turbulence in a many-body system"*, **Guram Gogia**, Wentao Yu, Justin C. Burton,*arXiv*, **1908.03138** (2020) Under review at *Physical Review Research*.

Acknowledgments

I would like to acknowledge the people who have played key roles in my life during my graduate studies at Emory University.

First of all, I wish to thank Prof. Justin C. Burton, my thesis advisor and a dear friend, for the wonderful research training and mentorship in the last five years. He supported my aspirations and taught me how to spot and appreciate the beauty of the physical world. Besides being an excellent academic advisor, he is a truly amazing human being, who increases levels of positivity in the universe. It is his patience, bright personality, research passion, immense knowledge and financial support that lead to this thesis, and the times with him at Emory will always be appreciated in the rest of my life.

I am especially grateful to the members of my committee, Professors Ilya Nemenman, Ajit Srivastava, Eric Weeks and Kurt Wiesenfeld, for their constructive suggestions and feedback on my research. Besides, I wish to acknowledge my colleague Dr. Juan-José Liétor-Santos for his mentorship and extensive discussions with me when I initially joined the Burton Lab. I also want to thank the current and past Burton Lab members: Leah Beanes, Nicholas Cuccia, Stephen Frazier, Yannic Gagnon, Dana Harvey, Tianshu Huang, Joshua Méndez, Asher Mouat, Kavinda Nissanka, Justin Pye, Dominic Robe, Toyin Thompson, Wentao Yu, Clay Wood, Bin Wu, Rui Wu, and Jiaqi Zheng for the awesome lab environment they created and useful discussions I have had with them over the last five years. Furthermore, I would like to thank other students and faculty at the Department of Physics at Emory for creating a collaborative and welcoming environment. I would also like to acknowledge my friends from other departments at Emory: Jonathan Basile, Alisina Bazrafshan, Bree Beal, Stephanie Koziej, Kelly McCormick, and Alex Viguerie for fun and insightful discussions.

Special thanks go to my friends in Atlanta, especially Nugzar and David Davitashvilis, Nino Khotivrishvili, Doug and Eliso Frutigers and Koba Lomashvili for helping me find a home in Atlanta. I really appreciate their generous support throughout my years in Atlanta. I also want to thank Brian Doolittle, George Gadrani, Dea Gigauri, Mark Gracyk, Peter Hamblett, Ben Hill, Max Hogue, Lasha Kalandadze, Levan Kantaria, Malia Kawamura, Pratap Luitel, John Taylor, Bowen Tretheway and Mike

Winters for their continuous friendship and willingness to transcend through discussions.

Finally and most importantly, I wish to express my heartfelt gratitude to my mother and grandmother, Cicino Kobakhidze and Leila Panjavidze, my brother, Zaza Gogia and my wife and best friend, Heather Saul. This thesis would certainly not have been possible without their love, unwavering support, and faithful encouragement.

Guram Gogia
Emory University, Atlanta, USA
Spring 2020

Dedicated to the loving memory of my grandmother
Leila Panjavidze

Chapter 1

Introduction

1.1 Turbulence as Spatiotemporal Intermittency

The dynamics of complex systems that are driven away from equilibrium are usually characterized by minor fluctuations around a steady state, abruptly punctuated by a "big jump" [3] that leads to a dramatically different state. The climate oscillates between hot and cold regimes over millennia [4], lakes switch between high- and low-nutrient regimes on decade-long time-scales [5], and rain showers pop up for a few minutes during summer afternoons. The emergence of intermittency is ubiquitous among complex systems and also lies at the heart of one of the oldest unsolved problems in classical physics: turbulence.

In the seminal experimental [6] and theoretical [7] works of Osborne Reynolds, Reynolds explored the conditions under which fluid flow is laminar or turbulent. Reynolds determined that the behavior of the pipe flow can be characterized using a single non-dimensional parameter, which would become known as the Reynolds number, and is given by

$$Re = \frac{\rho u L}{\mu}, \tag{1.1}$$

where ρ is the fluid density, u is the mean velocity and L is the characteristic length-scale for the flow, or the diameter of the pipe in this case, and μ is the dynamic viscosity of the fluid. The core question that Osborne Reynolds attempted to answer in his studies concerned the existence of a critical value of Re (Re_c) below which flow

would be laminar, and above it turbulent.

Unbeknownst to him, that question would continue to baffle scientists for decades to come. Reynolds found that Re_c was not well-defined and sensitively depended on the smoothness of the walls and other experimental conditions. Namely, in a well-controlled environment with smooth walls and tight pipe connections, laminar flow transitions to turbulence at $Re_c \approx 10000$, while for the pipes with rough walls, laminar flow can only be maintained up to $Re \approx 2000$. Furthermore, he found that the transitional regime between laminar and turbulent flows is characterized by the generation of distinct patches of turbulence (he called them "flashes") that travel downstream in the pipe and eventually decay back into laminar flow. Behind these seemingly simple observations hides Reynold's remarkable intuition pointing towards an intricate interplay between structural heterogeneities and large-scale evolution of the continuum. Understanding the nature of this interplay and the statistical properties of the resulting flow, remain active fields of research in fluid dynamics and nonlinear physics to this day. Similar to other complex systems, understanding the transition to turbulence requires identifying and isolating the constituents, then mapping the interactions between them and finally understanding how these interactions give rise to novel behavior on a global scale.

In this thesis, I present an unexpected experimental finding [1] and associated computational and theoretical framework [8], which can collectively serve as a minimal model for intermittent dynamics in spatially extended complex systems. A monolayer of dusty plasma crystal, made out of charged colloidal particles, experiences intermittent switching between crystalline and gas-like states, never settling to either state for several hours without modifying any experimental parameters. The experimental setup and findings are described in detail in Chapter 2. The energy source for this phenomenon is due to the spontaneous vertical oscillations that commence upon the reduction of plasma pressure below a certain threshold. This experimental discovery led down a dual path of exploration to explain this phenomenon. First, presented in Chapter 2, we characterize the mechanism of the peculiar emergent behavior. Second, presented in Chapter 3, we investigate the origin of the spontaneous vertical oscillations. Chapters 4 and 5 are dedicated to computational and theoretical

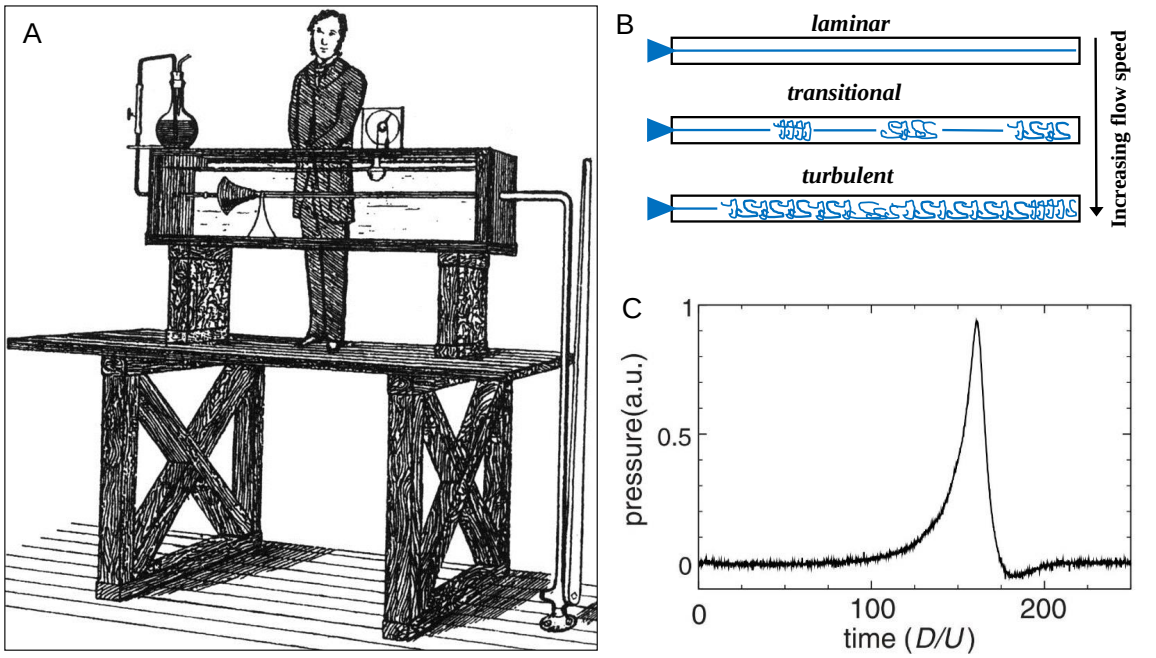

Figure 1.1: (A) Illustration of the experimental setup and Reynolds himself taken from the paper "An experimental investigation of the circumstances which determine whether the motion of water in parallel channels shall be direct or sinuous and of the law of resistance in parallel channels" . The image is reproduced from [6]. (B) Three different regimes observed in a pipe flow. Upon increasing the flow velocity, laminar flow (top) does not directly transition to turbulence (bottom), but rather experiences intermittent transitional regime. (C) Pressure signal from the experiment studying the turbulent puff generation in a transitional pipe flow. The image is reproduced from [9].

investigations of the phenomenon. I believe that our experimental discovery, along with numerical simulations and theoretical models, form a physical model that can be used as a framework for spatiotemporal intermittency that emerges in a large class of complex systems.

1.2 Attempts to Understand Transition to Turbulence

1.2.1 Stability of the Flow

Reynolds' original experiments along with his theoretical analysis spurred scientists to characterize the conditions for fluid stability. Most of the past century was marked by continuous attempts to understand the conditions for the transition to turbulence. The first two decades of the 20^{th} century were dominated by efforts to model turbulence as a growing linear instability. This was due to yet another of Reynolds' original observations that flow was stable for infinitesimal disturbances. This motivated physicists to find a mathematical representation for the criterion of fluid stability via analysis of the Navier-Stokes equations. Their efforts, however, were not successful and finding the stability conditions for turbulence evaded prominent physicists from that era including Orr, Prandtl and von Karmann [10]. It was G.I. Taylor's insight that served as a conceptual breakthrough in understanding the mechanisms governing the stability of laminar flow. He proposed that rather than inspect the stability of fluid motion under general conditions, one should concentrate on a specific case, understand the conditions for stability in a specific case, and then generalize those findings to general fluid flow scenarios. He conducted experimental and theoretical investigations [11] (he was the first to introduce statistical correlations and Fourier transforms to turbulence literature) of shear flow between two concentric cylinders and found agreement between experimental findings and linear stability analysis. This experimental system would become known as the Taylor-Coutte setup and remains a commonly utilized setup to study fluid behavior [12]. Nevertheless, finding similar conditions for the stability of pipe flow remained an outstanding challenge.

The 1930's signified a remarkable achievement in relating local fluctuations to large-scale flow behavior. Johanne Nikuradze, a graduate student in Prandtl's group, measured [13] the friction exerted on a turbulent fluid by the walls of a rough pipe, while controlling varying roughness of the pipe walls. Covering 5 orders of magnitude

of Re, his measurements, never to be repeated, showed among other things that friction factor, was a function of normalized wall roughness (r/D, where r is the surface roughness of the walls and D is the pipe diameter) and Re. Friction factor, f, is given

$$f = \frac{\Delta P/L}{\rho U^2}, \tag{1.2}$$

where ΔP is the pressure drop, L is the length of the pipe, ρ is the fluid density and U is the mean flow speed. Even though his work was not directly concerned with the nature of transition to turbulence, his experiments became the first attempt to quantify the relationship between local structural inhomogeneities and macroscopic flow behavior.

The 1940's brought several breakthroughs to theoretical studies of turbulence. Landau[14] and Hopf [15] separately proposed similar mechanisms based on nonlinear instabilities to explain transition to turbulence: upon increase of Re, fluid flow experiences a sequence of an infinite number of transitions, during each of which an additional frequency (wavenumber) arises, eventually resulting into complicated flow behavior. Another breakthrough in understanding the spectral properties of turbulence, and particularly interference of a finite length-scale, came from the Russian statistician, Kolmogorov in 1941, when he stated that for large Re flow, the transfer of energy from a large length-scale to smaller ones occurs in a dissipation-less manner and is only dependent on the mean energy transfer rate [16]. The cascade breaks down at the so-called Kolmogorov length-scale, where dissipation sets in. Even though Kolmogorov's assumptions were based on homonogeneity and isotropy of fluid motion, in drastic contrast with pipe flow, Goldenfeld showed in 2006 that the pressure drop in a rough-wall pipe and Kolmogorov's scaling are related [17].

With the rise of chaos theory in the 1970's, various models were proposed to elucidate connections between chaotic dynamics and turbulence [18–20]. Ruelle and Takens proposed a modified version of the Landau-Hopf picture - instead of a large number (hypothetically infinite) of sequential instabilities, only a small number, such as two or three, is sufficient to transition laminar flow into a complex, turbulent regime. Their theory was confirmed in a seminal experimental work by Gollub and

Swinney [21] who used the Taylor-Coutte setup to show that only a few successive instabilities suffice to yield turbulent flow. Their findings successfully unified dynamical control theory and hydrodynamics in an attempt to understand turbulence. However, these findings did not end up being useful for understanding the mechanism of intermittency observed during the transitional regime in pipe flow.

1.2.2 Turbulence as a Nonequilibrium Statistical Physics

In order to understand the challenges associated with the transitional pipe flow, one needs to understand the subtle details of that particular experimental setup. There are two main classes of experimental techniques that study turbulence in a pipe. The first one employs continuous perturbation–the second, localized perturbations. The former technique is commonly used to study fully-developed turbulence, which also exhibits strong fluctuations and exotic spectral properties. Without going into too much detail, in the context of transitional turbulent flow, the experimental setups utilizing a localized disturbance are more common.

Novel spatiotemporal behavior observed during the transition to turbulence is partially due to the linear stability of laminar flow in a pipe for all Re [22]. For low Re flows in a pipe, a finite disturbance will generate a turbulent "puff" that will travel down the stream and eventually decay away, whereas for higher Re, the disturbance of fluid results in a "slug", a spatially disordered region that expands downstream. Puffs usually do not change in size, whereas "slugs" extend and gradually occupy larger domains. In pipe flow experiments, the goal is to observe the evolution of the disturbances. How far will the puff travel? How much will a turbulent "slug" grow? How does the interface between laminar and turbulent regimes evolve over time? These questions can only be answered after the flow reaches an asymptotic state, which is only possible if experiments are repeatable, greatly determined by how carefully the inlets and connections to the walls of the pipes are engineered, and how smooth the pipe walls are. It is worth mentioning that engineering such a system took more than 100 years after Reynold's original experiments - Avila and colleagues [9] utilized a localized-disturbance technique to generate turbulent puffs and observe

their dynamics in an extremely long pipe to measure the lifetime statistics of puffs.

The existence of puffs and slugs implies that the transitional regime in a pipe flow can be conceptualized as the coexistence of two distinct thermodynamic phases. Just as gaseous and liquid phases are made out of the same molecules and under certain conditions can coexist, for example in a kettle with boiling water in it, laminar and turbulent states can be thought of as two distinct phases coexisting. The interface between the phases experiences observable complex spatiotemporal behavior [23, 24]. This view was further strengthened by Pomeau [25], who proposed that the speed of the turbulent-laminar interface front controls the metastability of turbulence. For a large enough velocity, stable puffs are generated and the downstream interface moves with the same speed as the upstream interface, a further increase of velocity results into a metastable "slug", where the downstream velocity moves faster than the upstream one, and consequently a "slug" will expand spatially. Pomeau modeled the dynamics of turbulent-laminar interface as a mass in a double-well potential with differing well depths. A deep well corresponds to a stable state, whereas a shallower one corresponds to a metastable one. Pomeau found that the propagation of turbulent puffs, their decay and other large-scale spatial phenomena can be captured by the dynamics of the mass in a double-well potential. In the same paper, Pomeau proposed a powerful framework to think about flow as coupled oscillators on a lattice, each oscillator can be in a laminar or a turbulent state with a finite lifetime. Each oscillator in a turbulent state can decay back to a laminar state or contaminate a neighbor. This framework was a close analogy to the directed percolation, a well-known non-equilibrium process in statistical physics that is still considered the universality class to which turbulence is related.

The efforts to connect transitional turbulence with universality classes culminated in 2016, when Shih and et al. [26], using direct numerical simulations, showed that different "species" of flow modes (laminar, turbulent and zonal) undergo predator-prey dynamics. Where laminar flow is a resource, turbulent modes are prey and zonal flow modes serve as a predator. Zonal flow is a collective mode that arises due to anisotropy of Reynolds stress tensor and unlike the mean flow, it is not driven by the pressure drop along symmetry axis of the pipe. Zonal mode is purely azimuthal,

with no dependence on the axial coordinate of the pipe. The authors found that during a transitional regime, anisotropic turbulent fluctuations give rise to large-scale zonal flow, which on its end suppresses the turbulence. The resulting stochastic predator–prey dynamics is equivalent to directed percolation at the critical transition. Their model also successfully explains the superexponential scaling of turbulent puff lifetimes and splitting time, observed experimentally by Avilla in 2011 [9].

Current research directions in the transition to turbulence are mostly statistical in nature and one would expect in the near future even more connections to be established between turbulence and nonequilibrium statistical mechanics. However, despite all the progress, both on the theoretical and experimental fronts, the mechanism that underlies novel spatiotemporal patterns of transitional flow remains unknown.

My graduate research was dedicated to understanding a nonlinear phenomenon which closely resembles transitional turbulence. Namely, a dusty plasma crystal made out of microscopic spheres immersed in a charged environment, under certain external conditions, experiences intermittent switching between crystalline and gas-like phases without modifying any parameters. At a glance, dusty plasmas do not have much in common with conventional liquids, but their dynamics are highly inertial, they are susceptible to fluctutations, and they can collectively create different phases of matter. Our serendipitous experimental finding motivated us to formulate a framework for understanding intermittent switching in spatially extended complex systems. The great advantage of our system is that we can visualize individual components, providing an opportunity to study local dynamics and relate it to large-scale emergent behavior. We also utilize molecular dynamics simulations to explore the parameter space and determine what structural and dynamical conditions are necessary for the emergent behavior. Furthermore, the insight that a scattering event is a necessary pre-condition for the melting transition to occur led us to model the orthogonal mechanical energies as interacting species. In the nature of turbulent and zonal modes in a transitional pipe flow, vertical and horizontal mechanical energies undergo predator-prey dynamics, marked by intermittent spikes in the horizontal energy. Similar to Reynolds number, we are able to describe the dynamics, both in simulations and with an "ecological" model, using a single non-dimensional number. Furthermore, a more

controllable model system that exhibits the statistical features of turbulent flow aids in establishing more connections between non-linear phenomena in spatially extended systems and statistical mechanics.

Chapter 2

Experimental Studies

Material presented in this chapter was published in:

• Gogia, Guram, and Justin C. Burton. "Emergent Bistability and Switching in a Nonequilibrium Crystal." Physical Review Letters 119.17 (2017): 178004.

2.1 Dusty Plasmas

Plasma is commonly referred to as the fourth state of matter after solid, liquid, and gas. Heating a solid to its melting temperature creates a liquid, which can be brought to its boiling temperature to obtain a gas. Finally, heating a gas to its ionization temperature creates plasma. Plasma represents a mixture of electrons, positively charged ions, and neutral atoms. The discovery of plasma is credited to William Crookes, who first found experimental evidence of plasma in 1879 [27] and called it "radiant matter". After 50 years, the famous American scientist, Irving Langmuir coined the term "plasma" for this ionized gas [28].

Dusty plasma (DP), also known as complex plasma, represents a phase of matter in which particles of condensed matter are submerged in plasma. The size of these particles ranges from tens of nanometers to hundreds of micrometers. Dusty plasmas are extremely abundant in outer space. In the beginning of the 20th century, astronomers started noticing dust particles, which were hindering them from observing objects of interest. In the 1960's, with the rise of infrared technology, astronomers

no longer saw particles as an obstacle anymore, realizing that these particles played a crucial role in star and planet formation.

Two experimental findings in the 1980's dramatically increased interest in dusty plasma systems. The first one was the observation of radial "spokes" in the outer portion of Saturn's rings. The pictures, which were taken by Voyager 2, revealed an intriguing aspect of Saturn's ring spokes [29]. Upon closer inspection, it was revealed that the spokes scattered sunlight more effectively in the forward direction, implying that the material had to be dust. Two separate research groups independently proposed the possibility that spokes are made of dust particles. However, a later discovery that paved the road for laboratory studies of dusty plasmas took place when Gary Selwyn *et.al* at IBM found that silicon wafers were adulterated inside the plasma reactors while being etched [30]. To this day, in the semiconductor industry, dust particles are viewed as the main source of contamination, which decreases the chemical deposition rate and consequently reduces the quality of silicon films [31]. Another field of research where dust particles are seen as a contamination source is fusion reactors, where due to plasma-wall interactions, the dust particulates can grow and lead to various operational and safety issues [32].

What the semi-conductor industry considered a contamination, the physics community saw as an opportunity to create a novel model system. The usual experimental setup for studying dusty plasma includes a vacuum chamber that confines the plasma, which is usually sustained by radio frequency (rf) or direct current (dc) external electric inputs. An optical setup is usually used to illuminate the dust particles, which are introduced to the system by mechanically shaking the particle reservoirs Fig.2.1. Aside from a few exceptions [33], most laboratory studies utilize spherical microparticles.

In the last three decades, particle-based model systems, first colloidal suspensions [34], and then dusty plasmas, gained relevance to study various many-body phenomena on the particle length-scale. The systems are appealing to the scientific community as they are relatively easy to create and it is possible to capture the behavior of individual particles with straightforward imaging techniques. The realization of dusty plasma crystals in 1994 [35, 36] has attracted the plasma and condensed matter

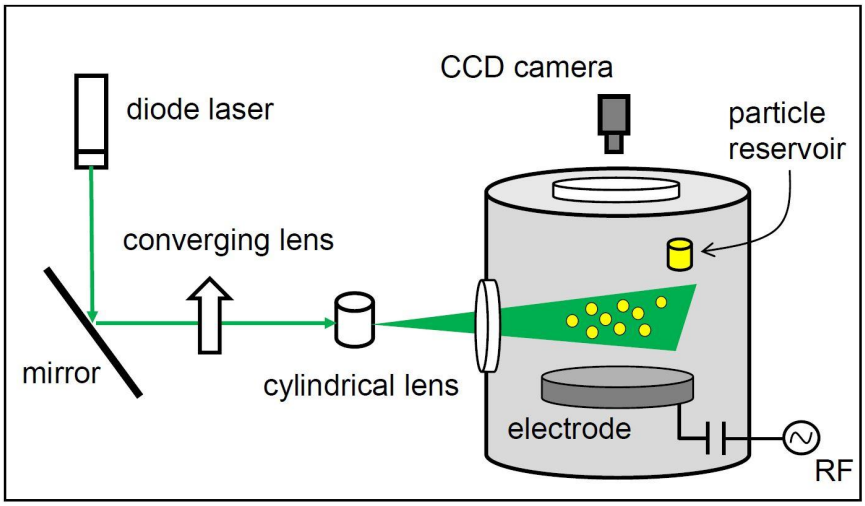

Figure 2.1: A diagram of the experimental setup. The 500mW green laser (LaserGlow) along with a mirror and converging and cylindrical lenses create a laser sheet that is used to illuminate the particles. The particles are introduced to the chamber by mechanically shaking the particle reservoirs, which are aluminum cylinders with a 0.1mm wide hole on the bottom. The particle positions are recorded using a PointGrey USB 3.0 camera equipped with a macro lens.

physics community and led to dusty plasmas becoming a complementary system to colloidal suspensions [37]. Both colloidal suspensions and dusty plasmas have been used to investigate phase transitions [38–40], phase separations [41, 42] and defect dynamics [43, 44] on the constituent particle-level. There is one important difference between colloidal suspensions and dusty plasmas, however. The particles in colloidal suspensions obey overdamped dynamics, whereas the particles in dusty plasma obey under-damped dynamics. Consequently, the inertia of the particles is not negligible, making the dusty plasma systems susceptible to environmental fluctuations, which usually results in a rich dynamical repertoire [45]. For example, dusty plasmas have been successfully used to study propagations of linear and non-linear waves [46, 47].

Another appealing aspect of using dusty plasmas as a model system is their inherent complexity. Dusty plasma is made out of distinct interacting "species" : ions, electrons and neutral atoms. The addition of dust particles increases the complexity further, which not only justifies the use of the term "complex plasmas," but also

provides a controllable model system to study real-world complex phenomena. Conceptually, mapping the behavior of real-life complex systems, such as ecologies, or power-transmission networks, onto the behavior of model systems is justified if the dynamics of the real and model systems share characteristic features. In the context of a philosophical framework, this is called a minimal model explanation [48], which allows the elimination of a large class of irrelevant variables and elucidates the essential ingredients that would reproduce the desired behavior. One remarkable example of a real-world phenomenon being reproduced in a model system is oscillations in light emission from dusty plasma successfully explained using a predator-prey framework [49]. Even though one would not expect the governing principles of the behavior of charged particles to have much in common with interacting species in nature, the underlying complex nature of plasma makes building such conceptual bridges possible.

2.1.1 Physics of Dusty Plasmas

Once plasma is ignited in the chamber, both electrons and positive ions start colliding with particles, the driving electrode, and other surfaces inside the chamber. The thermal velocity of the electrons in argon is 250 times larger than that of the ions, thus the collision rate of electrons on all surfaces is higher than that of ions. Consequently, the driving electrode gets charged negatively, attaining a negative DC bias. The resulting electric field points downwards, and as the charge on the particles is negative, there is an electrostatic repulsion that counterbalances the gravity, yielding a layer of levitating particles. The Debye sheath forms around the negatively charged particles. The charge on the particles usually ranges from 10^3 to 10^5 elementary charges. There are various models to estimate the charge on particles. The most commonly employed model, Orbital Motion Limited (OML) [51], along with other analytic models, approximates particles as a spherical capacitor. Then, particle charge is determined by the surface potential:

$$q_p = CV_p, \tag{2.1}$$

where q_p is the particle charge, C is the capactiance given by $C = 4\pi\epsilon a$, where a is the particle radius and V_p is the surface potential of the particle with respect to the

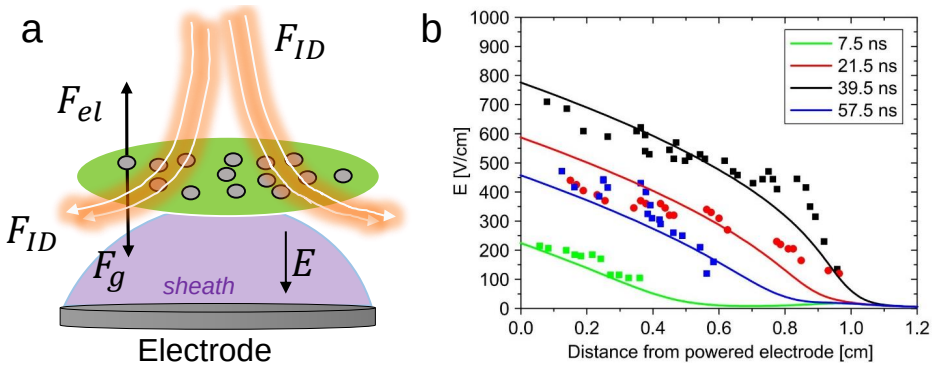

Figure 2.2: (a) A force diagram of particles levitating above the electrode. (b) Results of experimental measurement (points) and simulation (line) of electric field as a function of distance from the electrode in rf plasma. Reproduced from [50].

plasma potential of zero. Particles are surrounded by a cloud of positive ions, called Debye sheath, and the characteristic size of the sheath is called Debye or screening length, λ_D. The Debye screening length of a single particle is related to the screening lengths of ions and electrons -

$$\frac{1}{\lambda_D^2} = \frac{1}{\lambda_{De}^2} + \frac{1}{\lambda_{Di}^2}, \tag{2.2}$$

where λ_{De} and λ_{Di} are the screening lengths of the electrons and ions respectively [52]. Another important lengthscale in dusty plasma systems is the inter-particle distance, d. The relative sizes of the three main length scales, the particle radius, screening length and the inter-particle distance, determine the collective behavior of dusty plasma particles. Namely, if $a < \lambda_D < d$, one can treat plasma particles as isolated shielded grains and the collective behavior of the particles can be completely ignored. However, if $a < d < \lambda_D$, dusty plasma needs to be treated as a fluid, in which hydrodynamic interaction between particles plays a crucial role. Usually, in laboratory dusty plasmas, including our experimental setup, the latter scenario holds true.

Particles interact with each via shielded Yukawa potential

$$U_{ij} = \frac{kq_iq_j}{r_{ij}} \exp(-\frac{r_{ij}}{\lambda_D}), \tag{2.3}$$

where r_{ij} is the distance between particles i and j, q_i and q_j are the charges of the particles and k is the Coulomb constant. In equilibrium conditions, the collection of dust grains can be characterized using a nondimensional coupling parameter, Γ, which characterizes the ratio of electrostatic potential and thermal kinetic energies.

$$\Gamma = \frac{kQ^2}{dk_bT_d}\exp(-\frac{d}{\lambda_D}), \tag{2.4}$$

where d is the average interparticle distance and k_b is the Boltzmann constant and T_d is the effective dust temperature. For $\Gamma \lessapprox 1$, the system is weakly coupled and the collection of particles behaves like a fluid, whereas for $\Gamma \gtrapprox 170$ the particle self-organizes into crystalline structures. Finally, for intermediate values $1 \lessapprox \Gamma \lessapprox 170$, crystalline and fluid phases coexist.

Once introduced in the vacuum chamber, particles end up hovering above the powered electrode as a result of the balance between several different forces. The gravitational force, F_g is given by

$$F_g = \frac{4\pi}{3}\rho_d g a^3, \tag{2.5}$$

where ρ_d is the density of dusty particles and g is the gravitational acceleration.

The levitation height is set by the balance between electric repulsion, F_{el} and the combination of gravitational force, F_g and ion drag force F_{Di}. The simplified version of electrostatic repulsive force between a particle and the electrode assumes a linear gradient of the electric field and is given by

$$F_{el} = q(E_0 - \chi z), \tag{2.6}$$

where q is the particle charge, E_0 is the constant component and χ is the the gradient of the electric field. In reality, the electric field is a nonlinear function of the vertical distance from the electrode (Fig.2.2b), but for our experimental conditions it can be approximated with a linear relationship. Both gravitation and ion drag forces point downwards. The latter one originates from the momentum transfer from the scattering ions. For low ion densities, the ion drag force can be ignored and the levitation height can be accurately approximated by balancing gravitational and electric forces,

$q(E_0 - \chi z) = \frac{4\pi}{3}\rho a^3$ Fig.2.2a. The larger the mass of the particle, the lower its levitation height is going to be. However, if the ion density is not low, then the ion drag force will push particles further down towards the electrode, and in some cases, even generates voids in the center of the dusty plasma layers [53]. As a matter of fact, the ion drag force is responsible for various nonlinear interactions that emerge in dusty plasma systems. The stream of ions, which are directed towards the electrode, generate a wake right below the particles[54, 55]. The effect of the wake is usually modelled as a positive point charge at a distance d_f. Below the particle, however, in real-life settings, the structure and dynamics of the ion wake is a lot more complicated. If two particles are aligned vertically, then the ion wake from the upper particle will affect the lower particle, whereas the lower particle will not influence the upper one [56–58]. Non-reciprocal interactions can give rise to the "violation" of Newtons Third Law [59], particle-free voids in the sample [60], and ion wake-mediated coupling of in- and out-plane vibrational waves [61].

Finally, a neutral drag force arises due to neutral gas atoms colliding with dust particles and transferring momentum. If the particle size is much smaller than the mean free path and particle velocities are much smaller than the velocity of the surrounding gas molecules, then the neutral drag force is given by

$$F_n = -\gamma m v, \tag{2.7}$$

where γ is the damping coefficient and given by

$$\gamma = \delta \frac{8}{\pi} \frac{p}{a \rho v_t h} \tag{2.8}$$

The parameter δ varies depending on the collision mechanism between the gas atoms and the dust particles. It ranges from 1 to 1.42, corresponding to the lower limit of perfect scattering and diffuse reflection, respectively. For dusty plasma systems, δ has been found to be approximately 1.3 [62].

Other forces relevant for dusty plasma systems are the thermophoresis force [63], which emerges in the presence of a temperature gradient, and radiation pressure force, which is relevant when the particles are illuminated using powerful lasers [57]. For

our experiments these forces play a secondary role, thus we neglect them during our analysis.

2.2 Experimental Setup

A conventional experimental setup used for dusty plasma experiments is called the Gaseous Electronics Conference (GEC) cell [64, 65]. GEC represents a radio-frequency (rf) discharge confined in a vacuum vessel, similar to the setup shown in Fig. 2.1. The vacuum chamber is usually filled with an inert gas, argon for our experimental setup. As the pressure is lowered by pumping air out of the vessel using a vacuum pump, a capacitevely coupled radio-frequency power is applied to the bottom electrode that creates an alternating (13.56MHz) electric field and inert gas gets ionized. The power supplied to the electrode, and consequently the magnitude of the DC bias, can be adjusted by tuning the matching network. Another parameter that we control is the plasma pressure, which is regulated by the vacuum pump. In most dusty plasma experiments, including the ones presented in this work, the mean fraction of ionization is quite low, usually on the order of 10^{-4}. Even under such weak ionization conditions, the particles attain a net negative charge, ranging from 10^3 to 10^5 elementary charges.

2.2.1 Obtaining a Monolayer of Dusty Plasma Crystal

As mentioned earlier, the mass (size) of the particles determines the equilibrium levitation height. Considering that all the commercially available microparticles have some inherent polydispersity, there is no way to selectively introduce particles of certain sizes to the system. Once particles are introduced to the vacuum chamber, they will end up levitating at different heights from the electrode. Larger particles will end up levitating closer to the electrode, while the lighter ones will levitate further away from it. Our goal is to get rid of the large particles and obtain a monolayer of equally sized particles. In order to achieve this, we utilize a duty cycle function on the power supply: it allows one to periodically turn on and off the plasma with

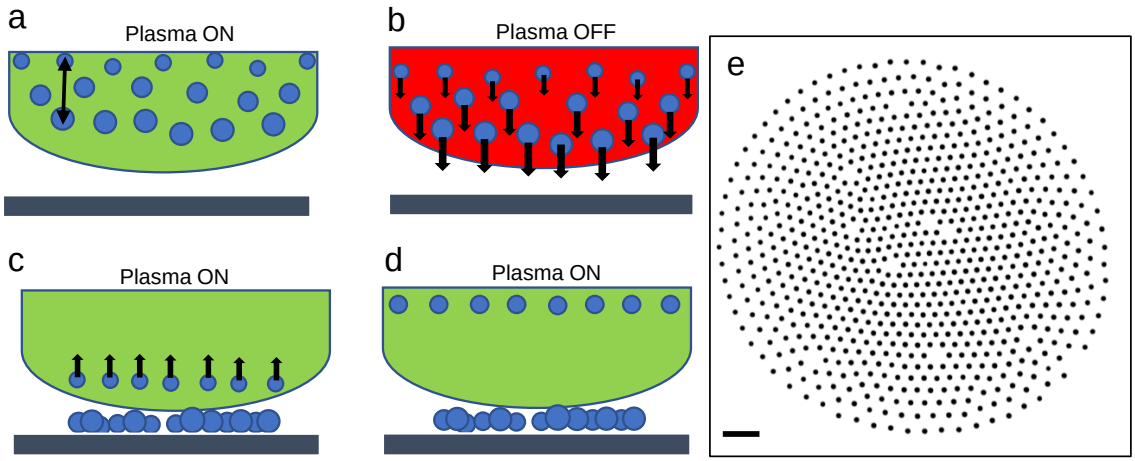

Figure 2.3: A diagram illustrating the operation of the duty cycle. (a) Once introduced to the plasma environment, polydisperse particles occupy varying equilibrium levitation heights. (b) Once plasma is off, all the particles start falling. Larger particles reach terminal velocity faster and are closer to the electrode than the lighter ones. (c) Plasma is turned back on once heavy particles fall on the electrode and stick irreversibly, and medium sized (desired) particles are still falling. (d) After the plasma is on, monodisperse medium-sized particles. (e) An inverted image of a layer of dusty plasma crystal made out of 691 particles of diameter 9.46 μm. The holes in the center of the sample are due to heavier particles that are not illuminated by the laser. The bar corresponds to 5mm.

some frequency f and duty cycle fraction α. In this way, the period of cycle is set by the frequency ($T = 1/f$), the time duration during which the plasma is going to be on is $T\alpha$ and the plasma is going to be off for $T \times (1 - \alpha)$. The trick is to adjust f and α so that the heavy particles fall and stick to the electrode irreversibly, while the lighter particles are still in free fall (Fig. 2.3c). Once the duty cycle is turned off, the lighter particles form a crystalline layer Fig. 2.3d-e. We have utilized different values of f and α, depending on the pressure of the plasma and dc but have found that using $f = 1Hz$ and $\alpha = 0.8$ is the most efficient way to clean the particles under the following experimental conditions: $V_{DC} = -20$V and $p = 2$Pa.

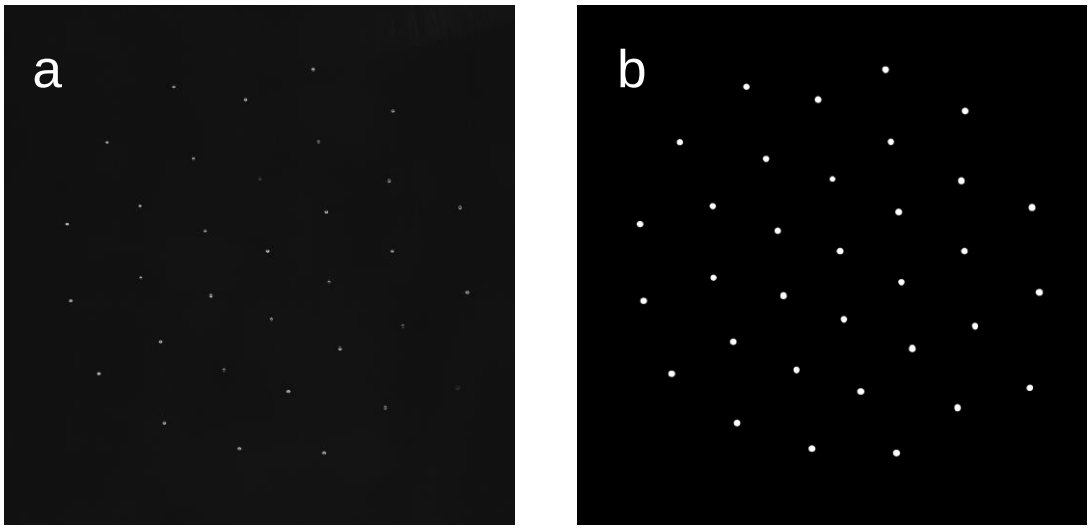

Figure 2.4: (a) Raw pmg image showing 33 particles. After using a sequence of ImageJ [66] commands to identify the edges of the particles, we applied Gaussian blur and subsequently adjusted the brightness and contrast on the image. The resulting image (b) significantly improves feature recognition and tracking.

2.3 Experimental Findings

2.3.1 Imaging Techniques and Image Analysis

Once a monolayer of dusty plasma crystal is obtained, it is illuminated using an optical setup that includes a laser and converging and cylindrical lenses. The diode laser with wavelength 534μm and power 500mW is oriented perpendicular to the plane of the electrode. The laser goes through converging and then cylindrical lenses to create a thin (200μm wide) laser sheet that once incident on the particles, illuminates them. The scattered light from the particles can be seen with a naked eye and is usually captured using a flycap usb camera and macrolens (Nikon). A typical picture of a dusty plasma crystalline monolayer can be seen on Fig. 2.3e. Images are recorded as tiff stacks and using ImageJ. We adjust the brightness and contrast to make the particles more visible. Afterwards, we use a python-based image analysis software package *Track-Py* [67] to identify each particle's position in each frame.

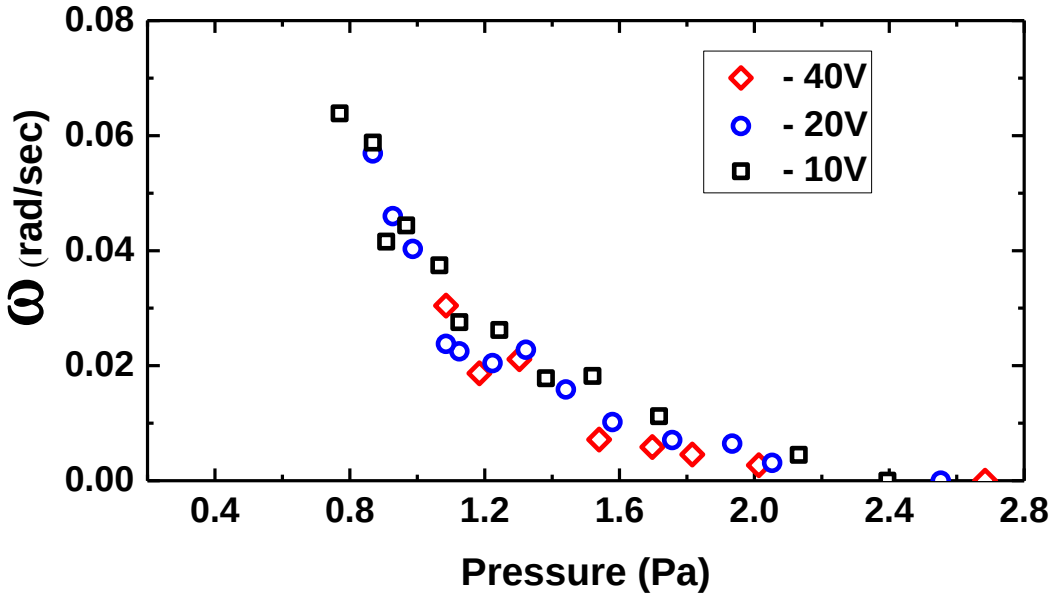

Figure 2.5: Angular velocity of rigid rotation of a crystalline system consisting of 881 MF particles with diameter 8μm as a function of plasma pressure. Different color points correspond to different bias voltages on the electrode.

Using *Track-py* we recreate the trajectories of each particle.

For reasons that will become obvious later on, we also modified the above mentioned optical setup to perform 3D scanning. We attached the mirror to the galvometer that would scan a volume of space and the dynamics of the particles inside.

2.4 Experimental Findings

As stated previously, the course of my graduate studies was shaped by the discovery of emergent bistable switching in dusty plasma crystals. The project that lead us to this discovery happened to be about a completely different subject. At that point, we were trying to make disordered layers of dusty plasma systems. We were hoping to achieve this goal by using particles of two different densities (ρ_1, ρ_2) and sizes (a_1, a_2) such that $\rho_1 a_1^2 = \rho_2 a_2^2$. This way electrostatic repulsion and gravitation attraction

would balance two different sized (consequently, different charged) particles at the same height. The goal of this line of research was the experimental demonstration of glassy dynamics in dusty plasma systems and to investigate vibrational modes, which happen to be unaccessable in other model systems, such as colloidal suspensions that are used to study glassy dynamics. The main question we were hoping to answer was if there was any difference between glassy dynamics in Newtonian and Brownian systems. We utilized polysterene and melamine formeldyhide particles with different pairs of sizes. We succeeded at obtaining a bidisperse sample, however, a slight change in pressure would result in dramatic separation of the two layers and a destabilization of the system. Remarkably, in a recent publication, Du and colleagues demonstrated [68] glassy dynamics in a bidisperse dusty plasma system consisting of 9.19 μm melamine formaldehyde (MF) and 11.36μm polystyrene (PS) microparticles in under-damped condition. Once we did not succeed in making a bidisperse sample, we decided to investigate the behavior of highly monodisperse samples.

2.4.1 Recrystallization and Rigid Rotation

Using a duty cycle function, we mastered obtaining a monolayer of dusty plasma crytal, consisting of 400 to 2000 highly monodisperse particles. Once such a system was obtained, we explored the phase behavior of the system using the two external parameters, which can be adjusted during the experiment : 1) power delivered to the electrode (which controls the accumulated bias voltage on the electrode and consequently ion density), and 2) the plasma pressure. Various studies have found that for large DC biases and plasma pressures, the collection of dust particles will form a crystalline layer, whereas for low values of the parameters, the system will be liquid-like [36, 69]. The mechanism behind the crystal melting is so-called mode-coupling theory [61, 70, 71], which predicts resonance coupling between the vertical and horizontal dust lattice (DL) waves. This occurs once the normalized frequency of the vertical confinement is reduced below a critical threshold. The vertical confinement frequency is proportional to both the ion density and the plasma pressure. The coupling between the modes has been hypothesized to be mediated by ion-wakes

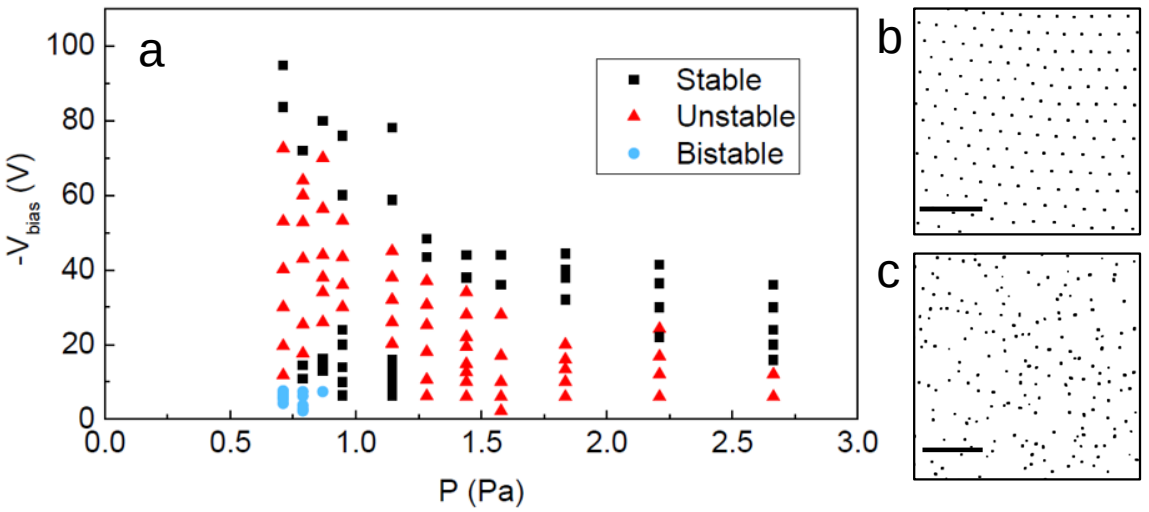

Figure 2.6: A phase diagram of a system consisting of 691 melamine-formaldehyde (MF) particles. For each fixed value of voltage, there is a threshold pressure below which the system melts. Further, a decrease of pressure and bias voltage results in full recrystallization of the system.

[72, 73]. Consequently, one would expect for each fixed value of bias voltage (pressure), there would be a threshold value of pressure (bias voltage) below which the system would melt irreversibly. The results of our investigation of the phase diagram of the system revealed similar trends. For each fixed value of plasma pressure, there was a unique bias voltage for which dusty plasma crystal would melt. Usually, the melting would commence in the center of the sample, where the particle density is the highest, and a further decrease in one of the parameters would result in the gradual and eventual complete melting of the system. Surprisingly, at least on first glance, the system would recrystallize for low values of pressure and voltage. We assume that the recrystallization occurs as a reduction of the plasma pressure results in a decrease in the ion drag force, allowing particles to move further away from the electrode to the region of lower horizontal confinement. Furthermore, the Debye screening length, λ_D, increases as the pressure is reduced and particles push each other away, resulting in recrystallization of the crystalline monolayer. Reduction of V_{DC} further weakens the ion drag force and particle charge.

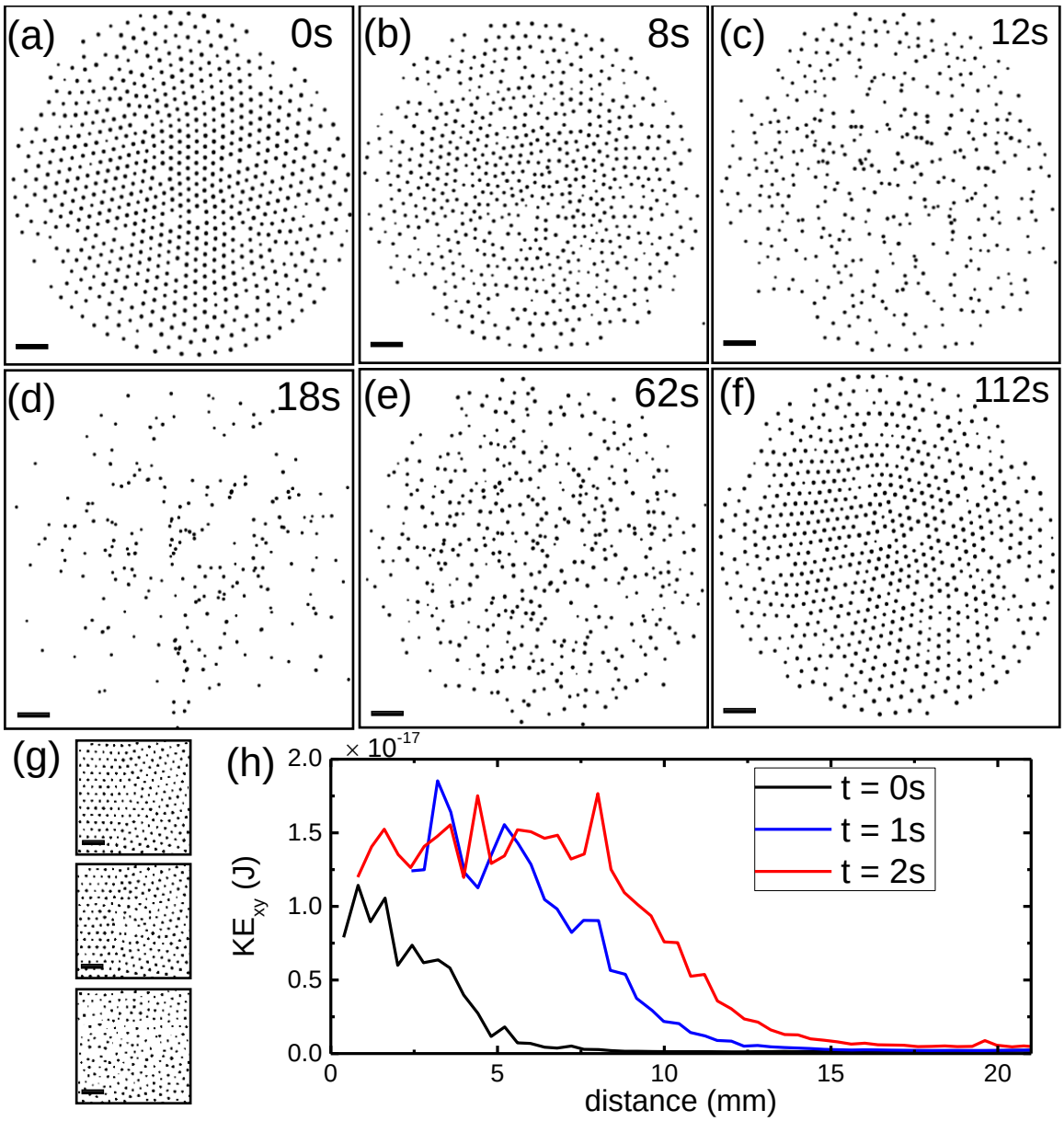

Figure 2.7: (a)-(f) Image sequence showing one cycle of melting and recrystallization of a particle monolayer made from 691 particles. Some particles move out of the plane of the laser sheet during the vertical oscillations and instability periods, so they are not visible. (g) Sequence of images showing the nucleation of melting taking place in the central part of the sample. The time between frames is $1s$. (h) Average horizontal kinetic energy per particle as a function of the distance from the nucleation event.

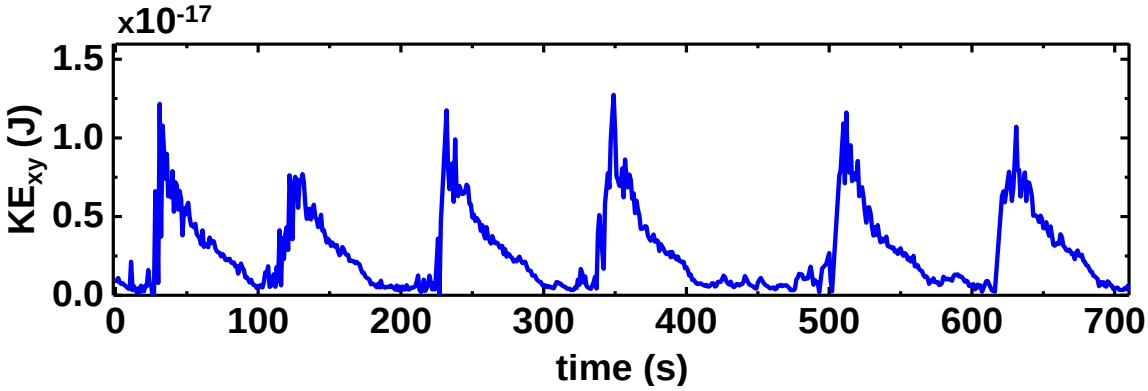

Figure 2.8: Six cycles of melting and recrystallization in a sample made out of 731 particles with diameters of 9.47μm.

Another surprising finding that escaped any explanation at first, was the observation of rigid rotation of the recrystallized systems. We observed that the angular velocity of the system was inversely proportional to the plasma pressure (Fig. 2.5. The direction of the rotation was always the same - clockwise, once viewed from above. Assuming that the rigid rotation was occurring due to $\vec{E_{rad}} \times \vec{B}$ drift, where $\vec{E_{rad}}$ is the electric field in the radial direction, and $\vec{B}$ is the magnetic field in the vertical direction. The drift makes the positively charged ions rotate and the ions drag the dust particles along. We calculated what should have been the strength of the magnetic field that would have generated a large enough force to rotate the particles of known size and density with a constant angular speed. Remarkably, the calculated value for the magnitude of the B-field was approximately the vertical component of the Earth's magnetic field in Atlanta, 43μT [74].

2.5 Emergence of Bistable Switching

The characterization of the phase diagram of the system led me to the aforementioned serendipitous discovery that shaped the course of my PhD studies. I came across a rather counter-intuitive phenomenon that for rather small values of the external parameters, the dusty plasma crystal would start oscillating in the vertical

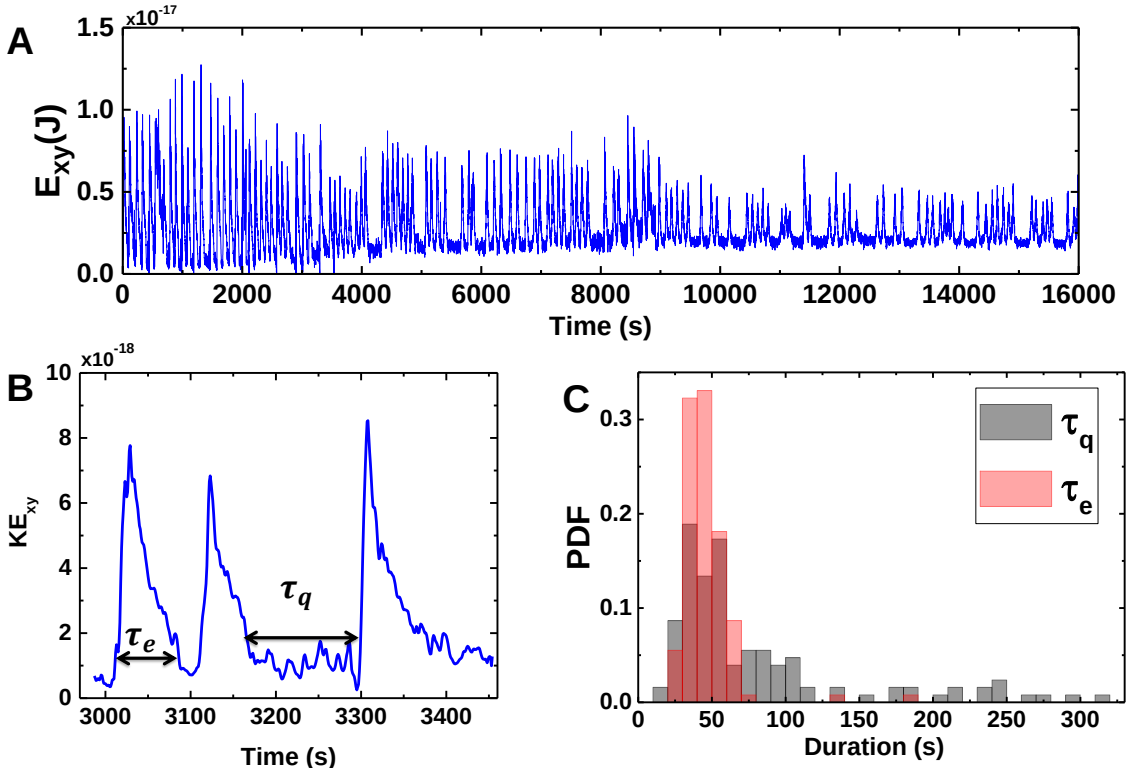

Figure 2.9: (A) Evolution of horizontal kinetic energy per particle for a system consisting of 723 particles with a mean diameter of 9.47μm for $\approx$ 5 hours. The peaks of KE_{xy} become less and less pronounced as the time goes on because the particles lose mass due to plasma interactions [75]. (B) Zoom-in on a $\approx$ 500s showing three occurences of the excited states. The duration of excited (τ_e) and quiescent (τ_q) states are defined. (C) The probability density functions of τ_e and τ_q from (A).

direction and periodically melt, remaining melted for tens of seconds and gradually recrystallizing. This phenomenon closely resembles intermittent turbulence in transitional pipe flow. In our experiments, the coherent vertical oscillation of the dusty plasma layer can be conceptualized as a laminar flow, whereas the melted state closely resembles a turbulent "puff". While the perturbations to the fluid flow in a pipe are due to external factors, such as rough walls, inlet or localized perturbations, the structural heterogeneities in our system are inherent - finite quenched disorder occurs inevitably due to distribution of particle sizes. As a matter of fact, slightly larger

sized particles, which have a larger charge on their surface and experience a stronger electrostatic force, pushes these large particles into the center of the sample. It is usually a defect due to one of the heavy particles (holes in the Fig.2.3e), from where the melting commences. Once melting nucleated at a defect, the melting front would move at the speed of sound, 1cm/s, radially outwards (Fig.2.7g-h).

Our initial experimental setup included a static laser sheet, meaning that we could not measure the vertical motion of the dust particles. Nevertheless, it was still possible to characterize the horizontal motion of particles quantitatively. Namely, we calculated the average horizontal kinetic energy per particle, by tracking the positions of individual particles and calculating the velocity using second-order central differences. The masses of the particles are calculated using the average particle diameter and manufacturer-provided value for the density. Fig 2.8 presents average horizontal kinetic energy over six cycles of melting and recrystallization for a system comprised of 751 particles with an average radius 4.73μm. There are a few features of the phenomenon that are worth highlighting. The transition to the gas-like state is rather abrupt since a copious amount of excess energy can be stored in the vertical oscillations. As the excited state relaxes, this excess energy dissipates more effectively since it is distributed among the horizontal degrees of freedom. In addition, the melting and recrystallization processes are not symmetric. As one can see, the melting, identified by non-zero kinetic energy in the crystal plane, propagates at a higher rate than the recrystallization occurs. Such temporal features are common in biological systems, where excitation processes are stochastic and relaxation is deterministic [76]. Moreover, the process is not actually periodic, but intermittent - the stability durations between two separate instabilities varies from one event to another.

In dynamical systems research, characterizing long-time behavior is always an interesting question. We have studied the statistics of the switching dynamics over a few hours. Namely, by measuring the average horizontal kinetic energy per particle and applying a threshold to it, we calculate the durations of the excited, "turbulent" (τ_e) and quiescent, "laminar" states (Fig.2.9B). Unfortunately, the duration of the experiments is limited by the fact that melamine formaldehyde particles start losing

their mass due to interactions with plasma [75], leading to an increase in the polydispersity of particles and eventual destabilization of the layer. However, before the plasma effects on the mass of the particles becomes pronounced, the system switches continuously between crystalline and gas-like states.

Chapter 3

Spontaneous Vertical Oscillations

Material presented in this chapter is under review process at Physical Review Research. The arxiv link for this work can be seen at

• Harper, J.M., Gogia, G., Wu, B., Laseter Z. and Burton, J.C., 2020. The origin of large amplitude oscillations of dust particles in a plasma sheath. arXiv:1908.03138.

3.1 Introduction

The energy source for the emergent intermittent dynamics in our system is the spontaneous vertical oscillation, which particles experience below some threshold of pressure. This phenomenon belongs to a larger class of nonequilibrium phenomena in dusty plasmas, which are enabled by the weak hydrodynamic dissipation of the surrounding neutral gas. Examples include instabilities [45], collective vibrational modes [61, 71] and fluctuation theorem for entropy production[77]. Indeed, the spontaneous vertical oscillation of particles suspended in an rf plasma sheath have been one of the better-studied phenomenona in the field of dusty plasma. Such spontaneous vertical oscillations have been observed and described by a multitude of authors over the last 20 years [78–85]. These oscillations seem to initiate once the gas pressure is reduced below a threshold value. The amplitude of motion, reported previously to be up to a few millimeters or less, increases with decreasing pressure.

A number of mechanisms have been proposed and explored to explain the origin

of the vertical oscillations [85]. Nunomura et al. [78] presented a delayed-charging mechanism that requires the equilibrium charge on a particle, Q_{eq}, to increase with height in the sheath (i.e. $\mathrm{d}Q_{\mathrm{eq}}/\mathrm{d}z > 0$), leading to an effective "negative damping". The threshold for this mechanism was given by Ivlev et al. [86], who also showed that stochastic charge fluctuations can parametrically couple to delayed charging to induce oscillations for small particles (≈ 1 μm in diameter). Samarian et al. [81] observed oscillations at higher pressures and suggested both spatial variation of charge [82] on the dust and boundary effects near the rf electrode. Finally, Resendes et al. [83] and Sorasio et al. [84] suggested a model based on fluctuations of the plasma sheath environment. In addition, an analysis of the motion of single particles showed a strong reduction in the effective damping rate, consistent with a delayed-charging mechanism [87]. Despite these laudable efforts, a lack of robust experimental data for the particle motion, coupled with the inherent complexity of low-density plasma sheaths, has limited our understanding of these nonequilibrium oscillations and their associated nonlinear dynamics. Vertical oscillations have also been identified as the driving mechanism behind the melting of dust plasma crystals through a "mode coupling" instability [61, 70, 71]. The instability is due to the presence of a "virtual" charge below each particle from each particle's associated ion wake field. However, this instability acts on a lattice of particles, and does not manifest as vertical oscillations of a single, isolated particle.

Interestingly, the vertical oscillations observed in Gogia et al. [1] have characteristics that, as far as we are aware, have not been observed previously. Undoubtedly, the most striking difference between that work and previous investigations involves the amplitude of oscillations. For instance, Nunomura et al. [78] and Takamura and others [80], who ascribe oscillations to a delayed-charging mechanism, report amplitudes on the order of hundreds of microns. In addition, Nunomura et al. [78] showed that the amplitude of oscillation in their experiments varied considerably over a few seconds. Similarly, Samarian et al. describe oscillations that, for a wide range of pressures and plasma powers, have amplitudes no larger than 1 or 2 mm [81]. Other authors have reported comparable oscillation amplitudes [83, 84]. Conversely, the observations described in Gogia et al. [1]) show that single, levitated micron-sized

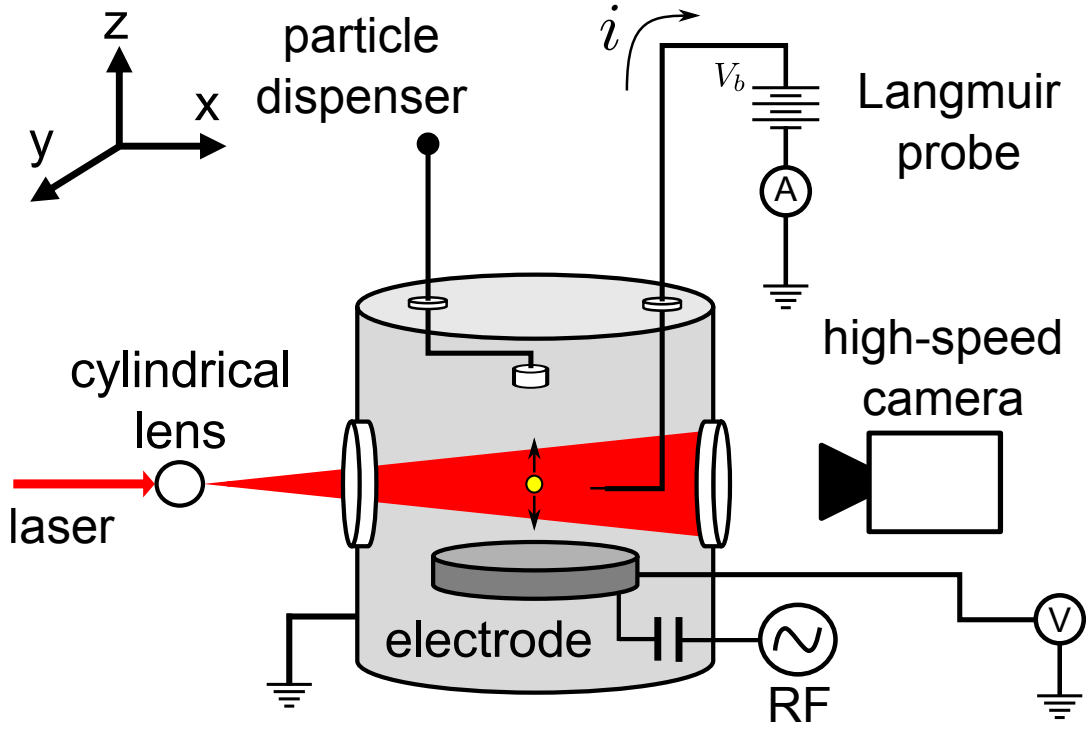

Figure 3.1: Experimental setup, slightly modified from [1], for imaging particle motion. The particle levitates in the rf sheath above the electrode and scatters the incoming laser light so it can be imaged with the high-speed camera. The vacuum system has ports so that the particle dispenser and Langmuir probe can be manipulated externally without losing a vacuum.

particles can oscillate with amplitudes larger than 3 mm with surprising regularity.

In this chapter, I present experimental results and associated numerical simulations to characterize the nature of such large-amplitude oscillations and compare the results to previously proposed mechanisms. At such large amplitudes (> 1 cm), comparable to the extent of the plasma sheath, the motion is highly anharmonic. The oscillations are initiated below a threshold pressure, typically 1 Pa, and depend on particle size and local plasma properties. We characterize the plasma environment using a Langmuir probe and find no appreciable fluctuations at low frequencies that may affect the particle motion. Our numerical simulations suggest that stochastic charge fluctuations are orders of magnitude too small to give rise to such large ampli-

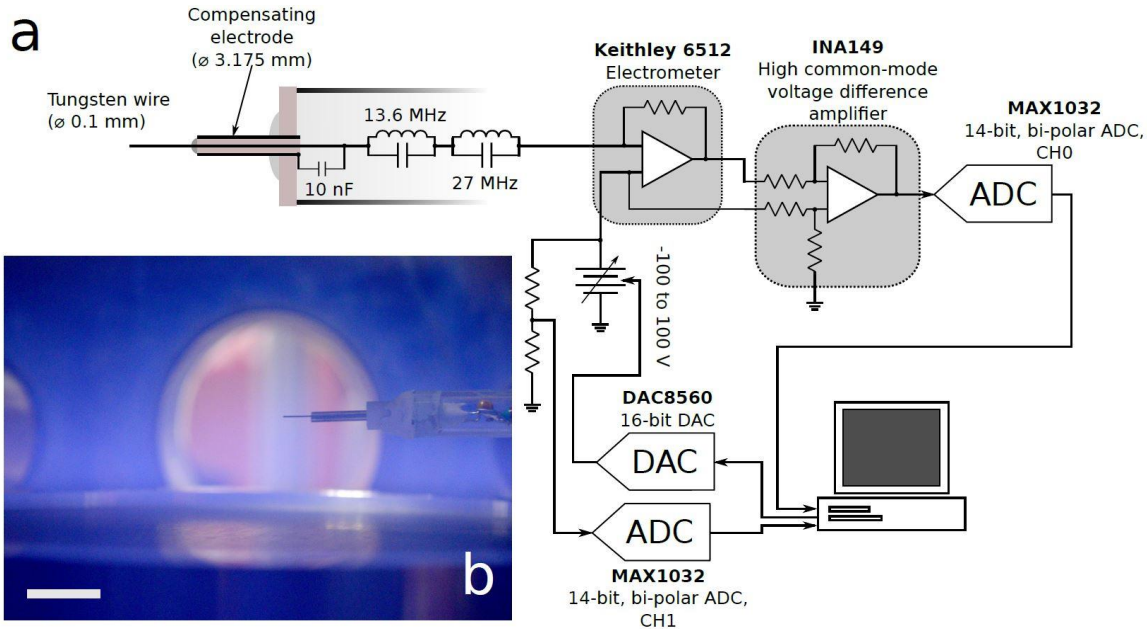

Figure 3.2: (a) Schematic of the compensated Langmuir probe used to characterize the plasma environment. See text for a detailed description. (b) Photograph of the Langmuir probe near the sheath boundary. The scale bar is 10 mm.

tudes of motion. We analyze hundreds of cycles of the particles' motion in order to extract the electrostatic force and spatial dependence of the equilibrium charge. We find that the model of delayed charging presented by Ivlev et al. [86] can accurately reproduce the motion. Our results also provide a quantitative estimate of the particle charging rate, ν, which is notoriously difficult to measure by other experimental methods.

3.2 Methods

3.2.1 Experimental setup

The experiments were carried out in a conventional GEC RF reference cell [1, 35, 59] (see Fig. 3.2 for a simplified schematic rendering). The system consists of a stainless-steal chamber which encloses a weakly-ionized argon plasma and the par-

ticles. The plasma was generated by a rf power-supply (operating at 13.56 MHz), capacitively-coupled to an aluminum disk (diameter = 15 cm) electrode near the bottom of the chamber. A particle reservoir was suspended over the electrode by a movable arm. The arm passes through the chamber wall, allowing the user to gently shake the reservoir and dispense a small quantity of particles into the plasma. A ring electrode 6 mm in height running along the edge of the disk electrode provides horizontal, electrostatic confinement to the grains. We denote the negative bias developed on the electrode as ϕ_{dc}.

We used both melamine-formaldehyde (MF) with nominal diameters of 8, 9.46, and 12.8 μm, as well as silica particles with nominal diameters of 6.27 μm. All particles had a coefficient of variance of 1.0%-1.5% according to the manufacturer (microParticles GmbH). However, we characterized the particle sizes using optical microscopy. A representative histogram for 9.46 μm MF particles is rendered in Fig. 4.3. Note that the distribution has a second peak at larger particle sizes that was not reported by the manufacturer.

As mentioned above, both the particles and the electrode acquire net negative surface charges. The particles levitate above the disk electrode at the position where the vertical electrostatic force balances the gravitational force. This position typically corresponded to a few millimeters below the edge of the sheath (at the transition to the pre-sheath). The thickness of the sheath varied inversely with pressure, and was typically 1-2 cm, as measured by the analysis of the particle motion (see Sec. 3.4.2). Although the drag force from the accelerated ions in the plasma sheath can contribute to this vertical force balance, our estimates of this force in our experimental conditions (see Sec. 3.4.1) suggests that ion drag forces are significantly smaller than either gravity or the electrostatic force.

The self-induced vertical oscillations are commonly studied in a system consisting of a large number of particles. In order to avoid any collective effects, in the present work, we focused on characterizing the dynamics of a *single levitated particle*. A system comprising an individual suspended particle (see Fig. 3.1) was produced by reducing the rf power supply's duty cycle (in essence, pulsing the plasma), causing some of the suspended particles to fall out during the "off" portion of the period.

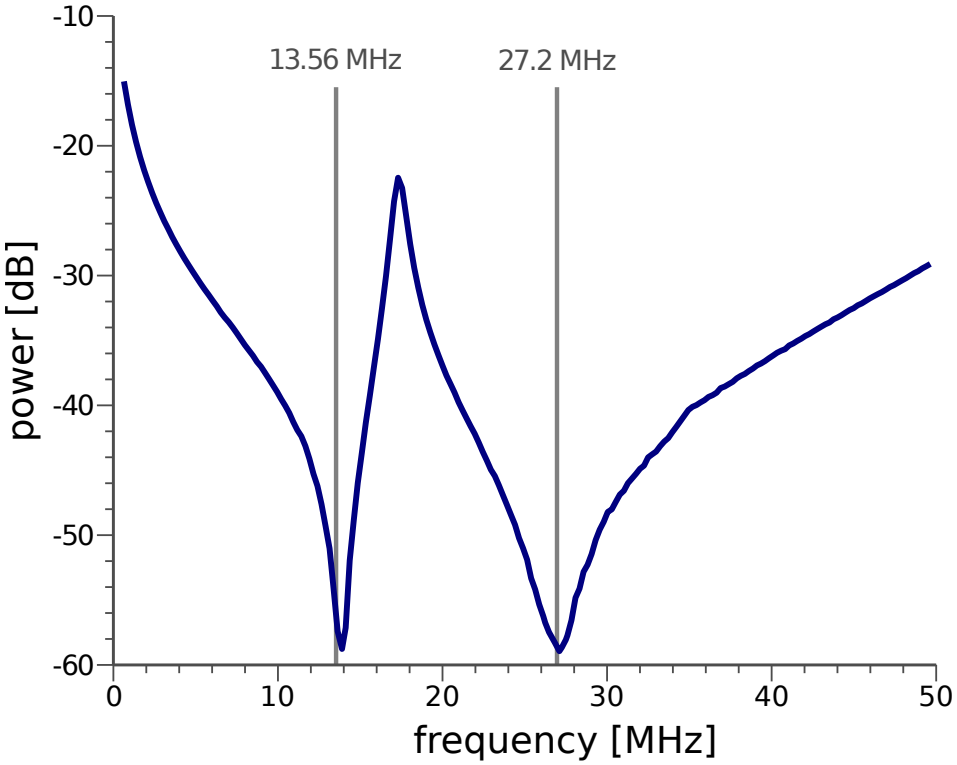

Figure 3.3: Frequency response of the Langmuir probe, as measured with a network analyzer, showing high impedance at 13.56 MHz and 27.2 MHz.

The duty cycle was returned to 100% once all but one particle were removed. We verified the presence of a single isolated particle by scanning a laser sheet through the chamber. Two variables were then adjusted to produce vertical oscillations: the gas pressure and the rf power delivered to the gas. We use ϕ_{dc} (as measured by a high-impedance electrometer) as a proxy for the plasma power. Previous studies [1] reported the occurrence of vertical oscillations in this experimental setup at pressures < 1 Pa and bias voltages in the range between -6 and -40 V. Here, we characterize our observed vertical oscillations under similar conditions.

We employed two principal instruments to characterize the particle's dynamics and the plasma environment: a high-speed camera (Phantom v7.11, Vision Research) to record the dynamics of the particle and 2) a custom-built, compensated Langmuir

probe to assess the plasma environment. To visualize the levitated particle, we illuminated it with a 100 mW vertical laser sheet (632 nm) created by passing the beam through a cylindrical lens. The camera was configured to record at 1000 frames per second.

3.2.2 Langmuir Probe

To characterize the plasma in which the suspended particle oscillate, we employed a custom Langmuir probe described schematically in Fig. 3.1. We note that all probe measurements were conducted with the particles *absent* from the system to ensure we were characterizing only plasma parameters. In its most basic form, a Langmuir probe consists of a thin wire with radius r_{P} inserted into the plasma and then biased to some potential ϕ_{b} relative to a reference node (here, the grounded chamber wall). The potential difference between the biased probe and plasma produces a sheath around the probe, resulting in a current flow through the probe which carries information regarding the plasma environment. Our probe design makes use of "low pressure theory," which implicitly assumes that r_{P} is much smaller than the Debye length λ_{D} and $\lambda_{\mathrm{D}} << \lambda_{\mathrm{mf}}$, where λ_{mf} is the ion mean free path [88]. For the plasma system described above, $\lambda_{\mathrm{D}} \approx$ 1-2 mm, and $\lambda_{\mathrm{mf}} \sim 13 - 30$ m in the bulk plasma (see Sec. 3.3.2).

The theory of Langmuir probes has been addressed in great detail in other works [88–91], however it is worthwhile to briefly summarize some key principles. When the probe has sufficient negative bias in relation to the plasma, a sheath around the probe effectively repels electrons and the current to the probe is the result of ions that random-walk past the sheath boundary. As the probe potential is made more positive, the ratio of electrons to ions collected by the probe increases, generating an electron retardation current. At some probe potential ϕ_{f} the number of ions arriving at the probe equals the number of electrons and the current through the probe goes to zero. This *floating potential* is characteristic of the equilibrium charge gained by objects immersed in the plasma, such as particles. Above the ion saturation current, the electron current through the probe grows exponentially because of the exponential

form of the Maxwell-Boltzmann electron velocity distribution in the plasma:

$$I_{\mathrm{e}}(\phi_{\mathrm{b}}) = I_{\mathrm{es}} \exp \frac{e[\phi_{\mathrm{b}} - \phi_{\mathrm{p}}]}{k_{\mathrm{B}} T_{\mathrm{e}}}. \tag{3.1}$$

In Eq. 3.1, e is the elementary charge, T_e is the electron temperature, and k_{B} is Boltzmann's constant. However, above the space potential ϕ_{p} the current no longer increases at an exponential rate. Here, current increase is solely due to an expanding collection region around the probe. At probe voltages larger than ϕ_{p}, the electron saturation current I_{es} is reached and is given by:

$$I_{\mathrm{es}} = e n_{\mathrm{e}} A \left(\frac{k_{\mathrm{B}} T_{\mathrm{e}}}{2\pi m_{\mathrm{e}}} \right)^{1/2} \tag{3.2}$$

where A is the exposed area of the probe, n_{e} is the electron number density, and m_{e} is the electron mass.

Physically, the probe is a cylindrical tungsten wire ($r_{\mathrm{P}} = 50$ μm) housed within a borosilicate glass tube (outer diameter 6.35 mm). Only a length of 5 mm of the wire is exposed horizontally to the plasma (see Fig. 3.2). All vacuum seals were made with TorrSeal epoxy. Because the plasma is generated by an rf source, the plasma parameters vary in conjunction with the source. Thus, we compensated our probe based on the design of Chen [92]. In essence, compensation involves forcing the probe to follow the plasma's AC component so that the voltage drop across the probe sheath ($\phi_{\mathrm{b}} - \phi_{\mathrm{p}}$) remains constant. Thus, we increased the probe's impedance to ground at 13.56 MHz and the first harmonic (27.2 MHz) using two resonant tank circuits in series. Additionally, an auxiliary electrode, capacitively-coupled to the probe tip, was required to ensure that the rf sheath impedance is lower than the impedance to ground. The auxiliary electrode has a much larger area than the probe tip and was placed coaxially with the probe tip. The frequency response of the compensated probe is rendered in Fig. 3.3, showing anti-resonances at 13.56 and 27.2 MHz. Our design, leveraging precision electronics, yields a probe capable of characterizing a plasma with picoampere and sub micro-Volt resolution.

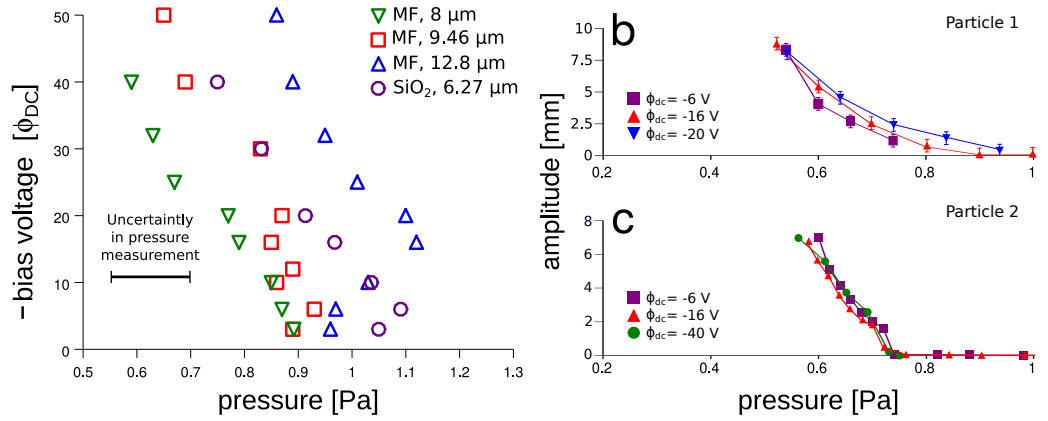

Figure 3.4: (a) The pressure/bias voltage combinations under which particles of different sizes and material compositions begin to oscillate. The uncertainty in the voltage measurement is much smaller than a data point symbol, whereas the uncertainty in pressure measurement is approximately 0.15 Pa (note horizontal error bar). (b) The amplitude of oscillation as a function of pressure and bias voltage for an MF particle with a nominal diameter of 9.46 μm. This dataset was acquired with help of a mechanical actuator resulting an uncertainty in the amplitude of 1 mm (note error bars). (c) The same measurement as in (b) but with a different MF particle of the same nominal diameter. For this dataset, the particle's amplitude was measured using a high-speed camera. Thus, the error is much smaller than in (b), on the order of a 40 microns. Within the uncertainty of the pressure transducer, there is good agreement between (b) and (c).

3.3 Results

3.3.1 Description of single-particle oscillations

At elevated gas pressures and plasma powers, a particle suspended in the plasma remains stationary at the point where the electrostatic force balances that of gravity. As mentioned previously, once the pressure is reduced below some threshold, the particle undergoes spontaneous vertical oscillations. However, we found that the precise value of the pressure threshold for a given particle depends on the bias voltage on the electrode. The combinations of plasma powers and gas pressures at which oscillations commence for different particle compositions and sizes are shown in Fig. 3.4a. Notice that as $|\phi_{\mathrm{dc}}|$ (and plasma power) is reduced, the onset of the vertical oscillations oc-

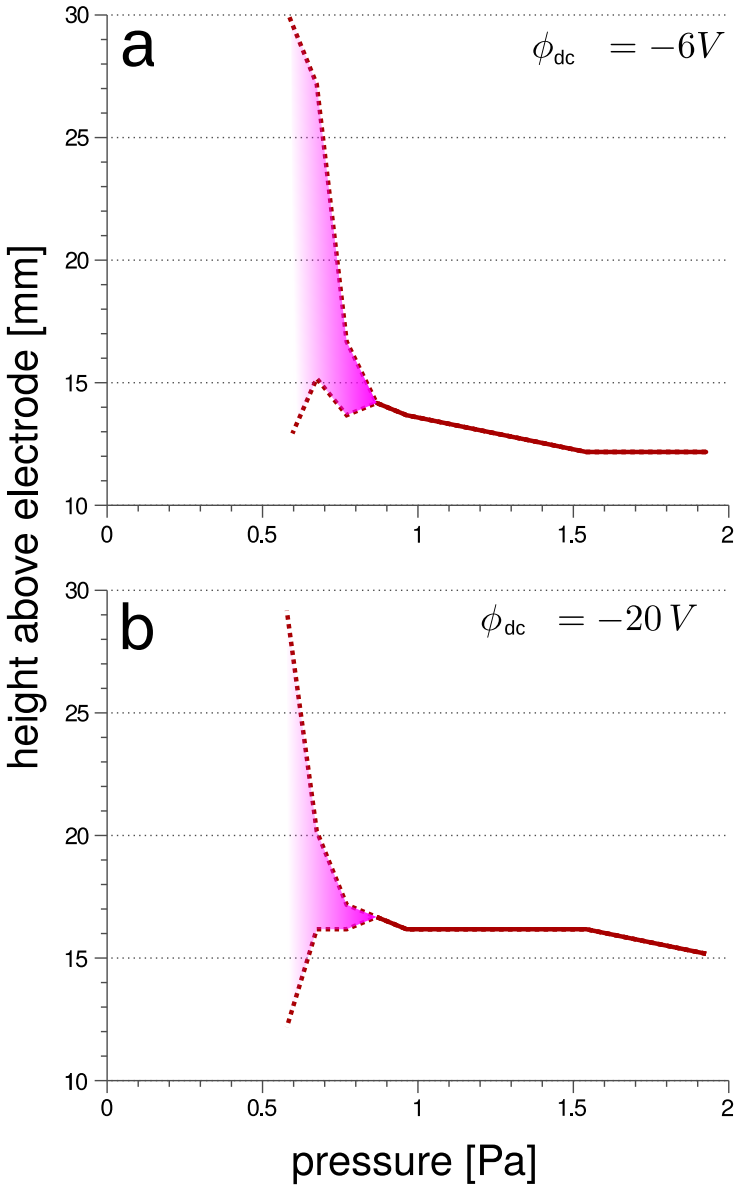

Figure 3.5: Position of an MF particle (9.46 μm diameter) as a function of pressure for two different bias voltages ϕ_{dc}: (a) -6 and (b) -20 V. In the two panels, the shaded areas denote the pressures at which particles oscillate. The upper and lower dotted lines show the lower and upper limits of the oscillation.

curs at higher gas pressures. The range of pressures at which the particles oscillate is narrower than the range of bias voltages, implying that the oscillations are more strongly dependent on P than on $\phi_{\rm dc}$.

To illustrate this point in greater detail, we measured the oscillation amplitude for two different 9.46 μm MF particles as a function of both P and $\phi_{\rm dc}$ (Fig. 3.4b-c). Although data was extremely repeatable for a given particle, there was significant variation between particles obtained from the same sample, presumable due to potential size variations (Fig. 4.3). For a given bias voltage, the transition between the stationary and oscillatory regimes occupies a very narrow pressure range. Indeed, by lowering the plasma pressure by only a few tenths of a Pascal, the particle oscillation amplitude increases from 0 μm to 10,000 μm (corresponding to a length scale equivalent to 1000 times the particle diameter).

While reports of spontaneous vertical oscillations of particles in plasmas are copious in the literature [78, 81–84, 86], the oscillations we observe in our experiments differ in two fundamental ways. Firstly, the amplitudes of the oscillations are more than 10 times larger than those reported in previous studies. At very low pressures and plasma powers, particles in our system undergo vertical excursions of several millimeters (sometimes, even exceeding 1 cm), whereas previous experiments produced oscillations not much greater than several 100s of microns. Also, the particle oscillation is particularly asymmetric at large amplitudes. Figure 3.5 shows the maximum and minimum positions of a MF particle as a function of pressure for two different bias voltages. As the pressure is lowered, the Debye screening length and the equilibrium position of the particle both increase. The strong asymmetry of the motion about the equilibrium position reflects the highly nonlinear variation in the electric field in the sheath. As we will show in Sec. 3.4.2, the particle actually exits the sheath and spends a significant portion of its cycle in free fall.

Secondly, the single-particle oscillation displays a regularity in both amplitude and frequency not seen in previous works. A time series of the vertical position of a single MF particle (9.46 μm) is shown in Fig. 3.6a. The regularity in the amplitude is striking and it persists for minutes. As will be discussed, this regularity strongly suggests that stochastic variations in the charge or plasma environment are not responsible for

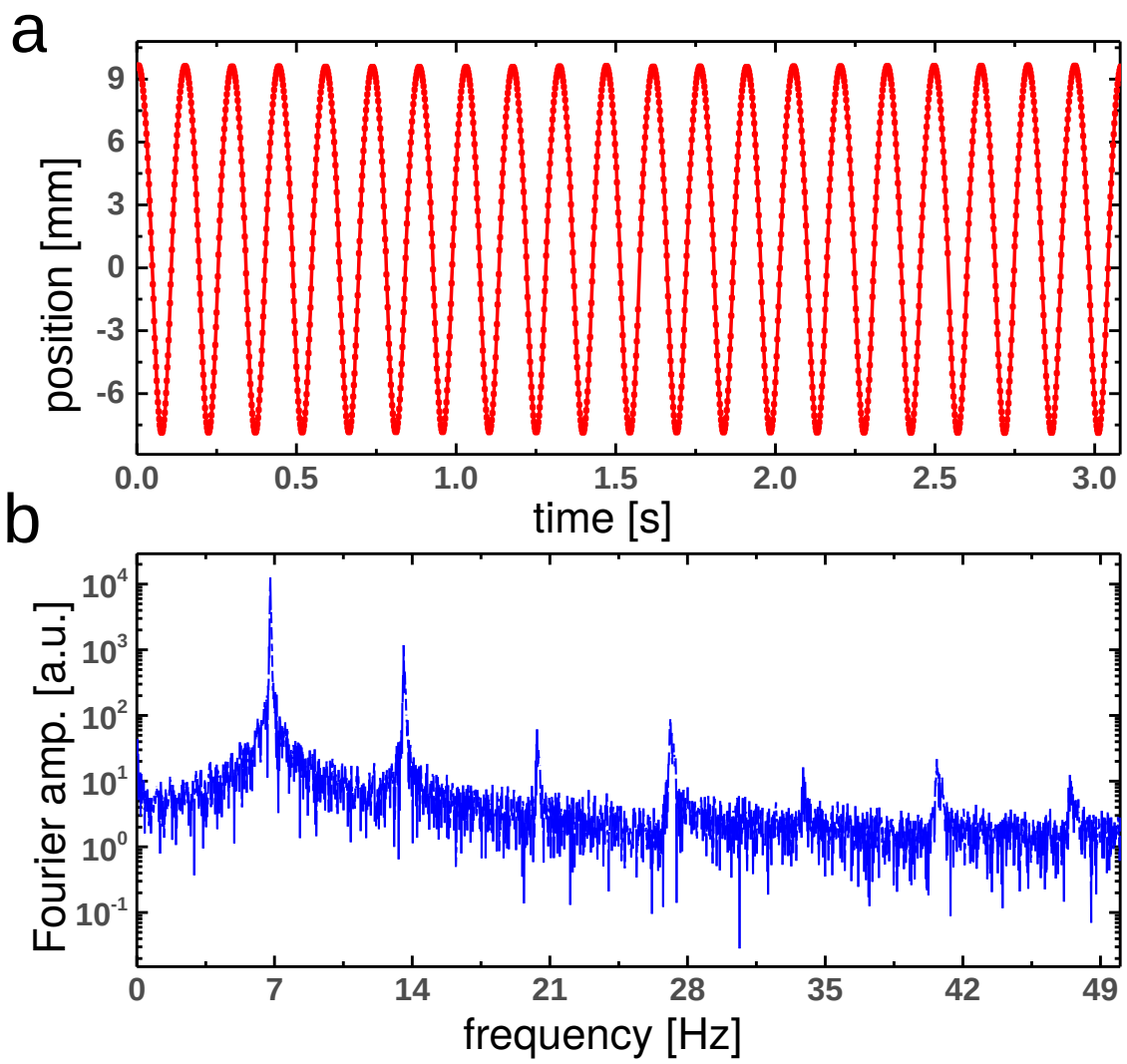

Figure 3.6: (a) Vertical position vs. time for a single MF particle (diameter = 9.46 μm). The constant-amplitude oscillation persists for minutes. (b) Fourier power spectrum of the particle oscillation. Both even and odd harmonics are visible.

driving the particle motion. Additional information can be gained from analyzing the spectral content of the particle's trajectory. A power spectrum of the particle motion is shown in Fig. 3.6b. Note that, while most of the energy is concentrated in the ~ 7 Hz fundamental, the oscillations display activity across odd and even harmonics. In other words, the motion of the particle is not strictly sinusoidal, but rather exhibits

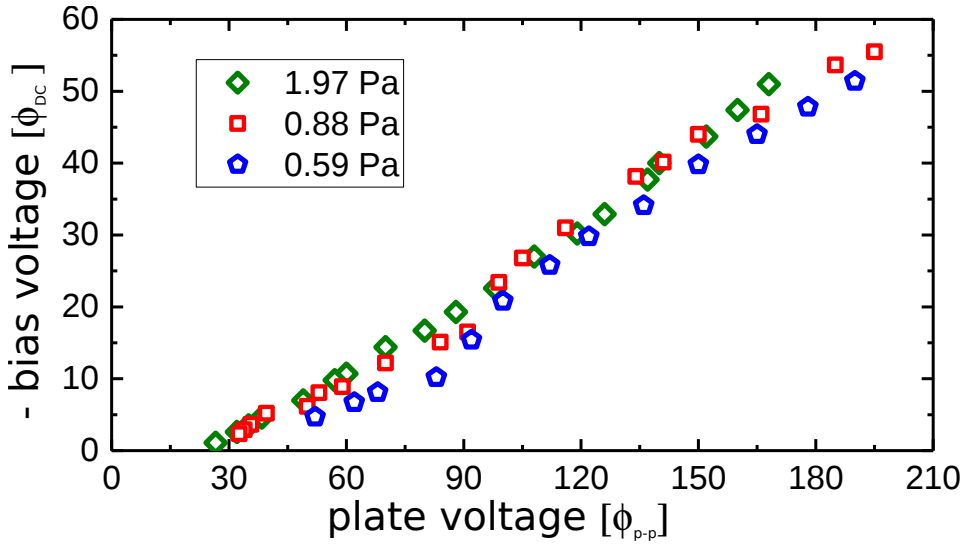

Figure 3.7: The dc bias voltage on the electrode $\phi_{\rm dc}$ as a function of the peak-to-peak ac voltage applied to the electrode at 13.56 MHz. Data is shown for three different values of the pressure. At lower pressures, the data deviates more significantly from linear behavior.

considerable anharmonicity.

3.3.2 Plasma characteristics

Before analyzing the motion of suspended particles, we discuss the plasma environment in which they levitate. As aformentioned, the plasma was generated through a powered disc electrode (see Fig. 3.1). While we use the bias voltage ϕ_{dc} as a proxy for the plasma intensity, we refer the reader to Fig. 3.7 which shows $\phi_{\rm dc}$ as a function of the peak-to-peak ac voltage applied to the electrode for three representative pressures. Note the generally linear behaviors, and relatively weak dependence of pressure. Unless otherwise noted, all reported voltages are reported relative to system ground.

We used a Langmuir probe to characterize basic plasma properties such as the floating potential $\phi_{\rm f}$, the plasma potential $\phi_{\rm p}$, and ion number densities. The current-voltage characteristics for our Langmuir probe are shown in Fig. 3.8a for a pressure of 1.02 Pa and $\phi_{\rm dc}$ = -6, -20, and -40 V. The voltage on the probe $\phi_{\rm b}$ was swept between

-100 and 50 V relative to system ground (for clarity, only the response between -10 to 50 V is shown in Fig. 3.8). The dashed vertical lines indicate the points where the current in the Langmuir probe was 0 A, representative of the floating potential ϕ_f for each of the three electrode voltages. For ϕ_{dc} = -6 V, $\phi_f \approx$ 15.5 V; for ϕ_{dc} = -20 V $\phi_f \approx$ 16.5 V; and, for ϕ_{dc} = -40 V $\phi_f \approx$ 16.5 V.

As mentioned above, when the voltage applied to the Langmuir probe is raised above a threshold ϕ_p, the current no longer increases exponentially and increases slowly as the collection region around the probe expands. This *plasma potential* can be found by differentiating the I-V characteristics in Fig. 3.8a and locating a change in slope (Fig. 3.8b). For ϕ_{dc} = -6 V, $\phi_p \approx$ 22 V; for ϕ_{dc} = -20 V, $\phi_p \approx$ 23 V, and, for ϕ_{dc} = -40 V, $\phi_p \approx$ 24 V. Due to differentiation, the error in the estimate of the plasma potential is +/- 1-2V. The floating potential is defined at the point where $I_{ion} = I_e$, where I_e is given by Eq. 3.1. For the current study, we estimate I_{ion} from the Bohm current [90]:

$$I_{ion} \approx \frac{n_i e A}{2}(k_B T_e/m_i)^{1/2}, \tag{3.3}$$

where m_i is the ion mass, and n_i is the ion number density. Equating Eq. 3.1 and 3.3 and assuming quasi-neutrality ($n_e \approx n_i$) leads to:

$$\phi_f = \phi_p - \frac{k_B T_e}{2e} \ln\left(\frac{2m_i}{\pi m_e}\right). \tag{3.4}$$

For argon, the above equation can be simplified to: $\phi_f - \phi_p \approx -5 k_B T_e/e$ (which includes a geometrical correction factor for a cylindrical probe tip [90]). Thus, for our experimental conditions, T_e is in the range of 1.3 - 1.5 eV.

The ion number density n_i can also be extracted from the I-V characteristics using the floating potential method described in Chen et al. [2]. This method consists in extrapolating the ion saturation current to the floating potential, as shown in Fig. 3.9. The ion density at ϕ_{dc} = -6 V is 2.24 $\times 10^{13}$ m^{-3}; at ϕ_{dc} = -20 V, 4.28 $\times 10^{13}$ m^{-3}; and at ϕ_{dc} = -40 V, 5.57 $\times 10^{13}$ m^{-3}. Thus, the electron Debye length in the plasma system can be calculated as follows [93]:

$$\lambda_D = \left(\frac{\epsilon_0 k_B T_e}{e^2 n_e}\right)^{0.5}. \tag{3.5}$$

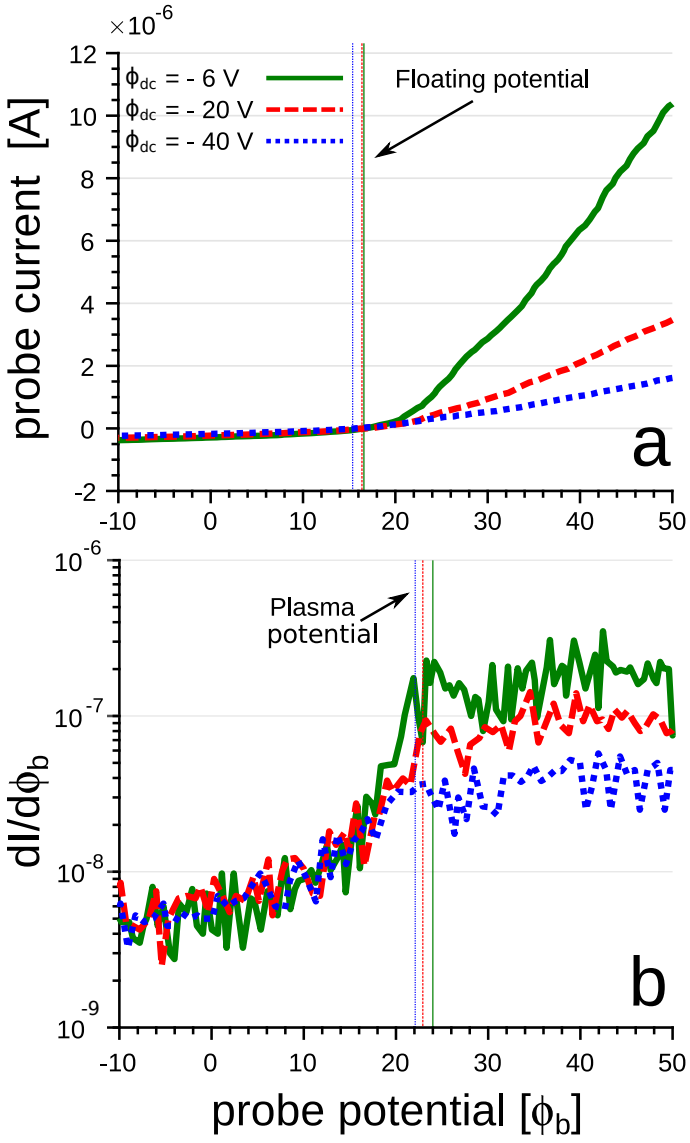

Figure 3.8: Langmuir probe measurements for the collection current (a) and its derivative (b) as a function of probe potential for three different values of $\phi_{\rm dc}$ at $P = 1.0$ Pa (a pressure corresponding to the threshold at which oscillations begin). The height of the probe above the rf electrode was 40 mm (in the bulk plasma). The point at which the current crosses zero indicates the floating potential $\phi_{\rm f}$, and the change in slope is representative of the plasma potential $\phi_{\rm p}$.

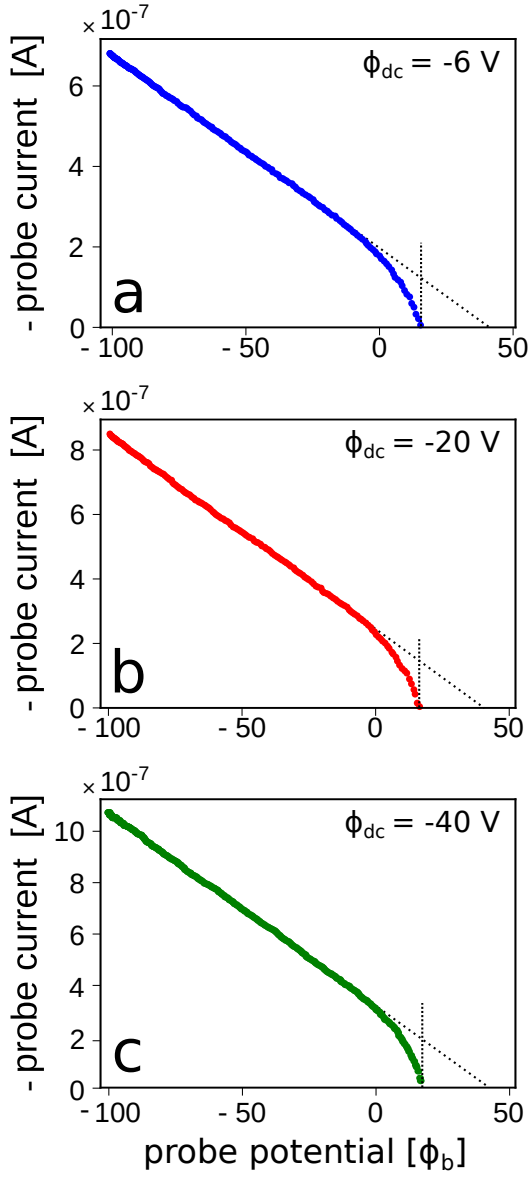

Figure 3.9: Zoom-in of the ion current portions of the plasma I-V characteristics rendered in figure 3.8. Note that these curves have been plotted with sign reversal. Using the floating potential method described by Chen and company [2], we can estimate the ion density n through an extrapolation to the floating potential of the saturation ion current (see fitted, black curves in figure above). We perform this analysis for bias potentials of (a) -6 V, (b) -20 V, and (c) -40 V. The ion density at ϕ_{dc} = -6 V is 2.24 $\times 10^{13}$ m^{-3}; at ϕ_{dc} = -20 V, 4.28 $\times 10^{13}$ m^{-3}; and at ϕ_{dc} = -40 V, 5.57 $\times 10^{13}$ m^{-3}

.

Here, ϵ_0 is the permittivity of free space. At $\phi_{\rm dc}$ = -6 V, $\lambda_{\rm D}$ = 1.78 mm; at $\phi_{\rm dc}$ = -20 V, $\lambda_{\rm D}$ = 1.39 mm; and at $\phi_{\rm dc}$ = -40 V, $\lambda_{\rm D}$ = 1.21 mm. Lastly, the ion mean free path $\lambda_{\rm mf}$ for argon ions can be computed using:

$$\lambda_{\rm mf} = \left(\pi d_{\rm c}^2 n_{\rm i}\right)^{-1}, \tag{3.6}$$

where, $d_{\rm c} \approx e^2/(4\pi\epsilon_0 m_{\rm i} v_{\rm i}^2)$ is the argon ion's interaction length enhanced by Coulomb forces. The mean thermal speed $v_{\rm i}$ for the ions is given by $\sqrt{8k_{\rm B}T_{\rm i}/(m_{\rm i}\pi)}$. Note that for our experimental conditions the ion temperature is close to the neutral gas temperature, $\sim$ 300 K. For our experimental conditions, λ_{mf} ranges between $\sim$ 30 m (at ϕ_{dc} = -6 V) to $\sim$ 13 m (at ϕ_{dc} = -40 V); Thus, as discussed previously, $\lambda_{\rm D} << \lambda_{\rm mf}$ and the use of "low pressure theory" is justified for our Langmuir probe experiments.

Beyond extracting fundamental plasma parameters, we employed our Langmuir probe to determine whether variations in the plasma existed in our experimental setup under the conditions where particle oscillations are observable. For a fixed $\phi_{\rm b}$, the probe can resolve very small changes in the plasma environment. For instance, Fig. 3.10a shows that millivolt changes in ϕ_{dc} can be readily detected by the probe. As discussed later on in Sec. 3.4.3, variations in the plasma would have to be much larger to produce oscilliations with a modest 1 mm amplitude. The homogeneity of our plasma at low frequencies is quantitatively described by the Fourier transform of the Langmuir probe current in Fig. 3.10b. Between 0.1 and 1000 Hz, there are no discernible spectral components that would give rise to particle oscillations. In addition to searching for variations in the probe current, we obtained spectrograms of the the bias voltage ϕ_{dc} to determine whether fluctuations on the electrode were present at the conditions under which particles oscillate. A broadband spectrogram

Thus, it is unlikely that temporal inhomogeneities in the plasma are responsible for the spontaneous vertical oscillations observed in our experiments.

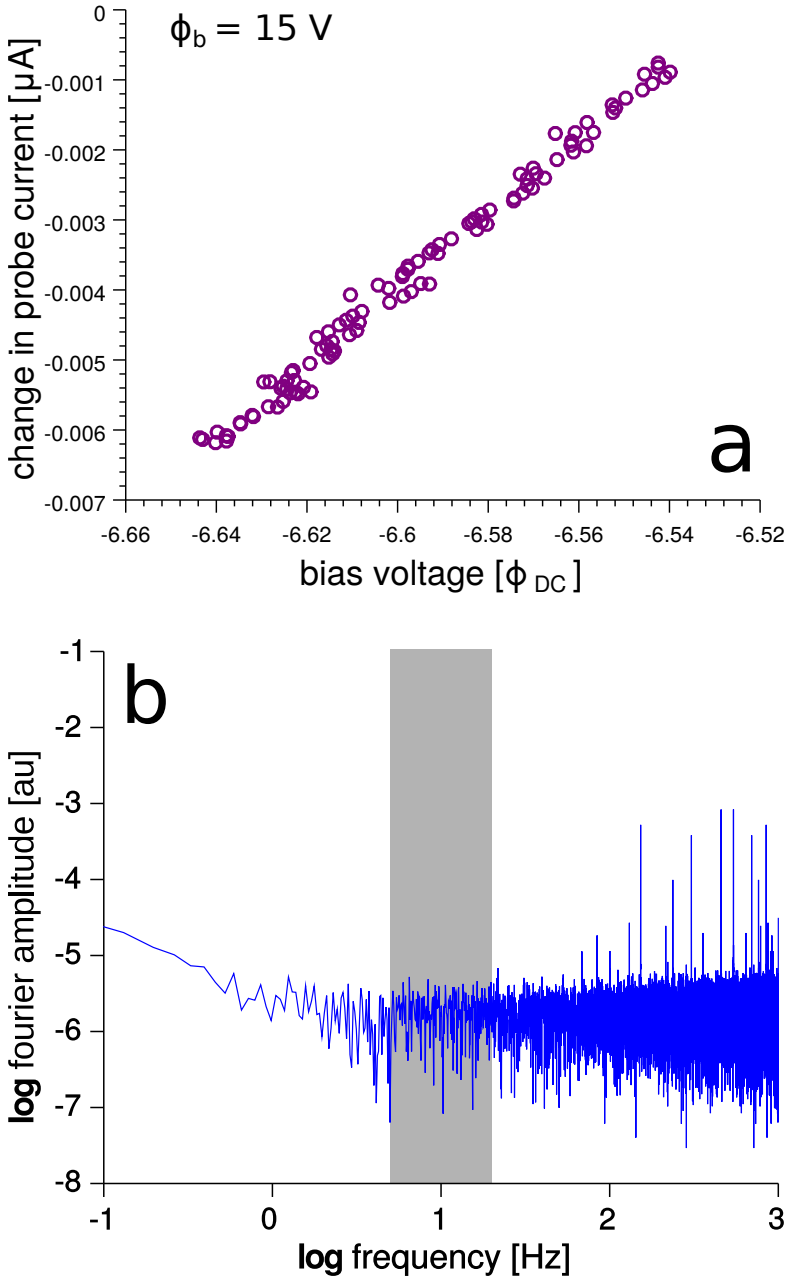

Figure 3.10: (a) Variation in probe current as a function of a small, controlled change in bias voltage, demonstrating the sensitivity of both the ammeter and voltmeter sensitivities (order pA and μV, respectively). (b) Fourier transform of voltage fluctuations from the Langmuir probe at 15 mm above the electrode. The probe was biased to zero Volts relative to system ground, and the pressure was 0.6 Pa. The gray region depicts the typical frequencies of particle oscillations.

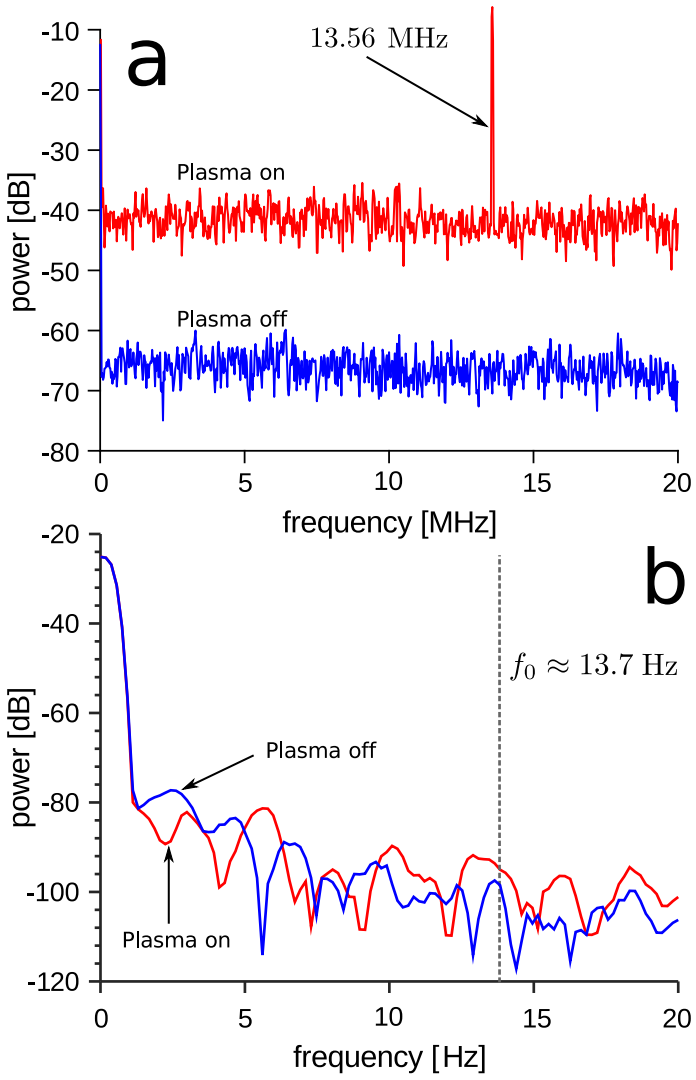

Figure 3.11: (a) Broadband spectrogram of the bias voltage ϕ_{dc} on the electrode with the plasma on (red; note the power spike at 13.56 MHz) and off (blue). The pressure was $P = 0.6$ Pa. Note that the "off" has been shifted downward for clarity. (b) Narrow band spectrogram the bias voltage ϕ_{dc} on the electrode with the plasma on (red) and off (blue) at frequencies near characteristic frequencies of particle oscillation (Sec. 3.4.2)

3.4 Discussion

3.4.1 Forces on a dust particle

In order to understand the origin of the spontaneous oscillations, it is necessary to enumerate the forces acting on a particle in the vertical direction [94, 95]. First, gravity acts on the particle with force $F_g = -m_p g$, where m_p is the mass of the particle and g is the acceleration due to gravity. For the 9.46 μm MF particles used in our experiment with density $\rho_p = 1510$ kg/m^3, $F_g \approx -6.6 \times 10^{-12}$ N. The electrostatic force acting against gravity is given by

$$F_e = -Q_{eq} E. \tag{3.7}$$

Here E is the electric field in the sheath, which points in the positive z direction, and depends on position z. Q_{eq} refers to the average charge the particle will obtain at a given position z in the sheath given sufficient time. This will later become important when the particle moves rapidly through the sheath (Sec. 3.4.4).

The particle will also feel a drag force as it moves through the background of the neutral gas:

$$F_d = -\gamma m_p v_p, \tag{3.8}$$

where v_p is the velocity of the particle in the z-direction. The damping rate γ is given by the Epstein law [94]:

$$\gamma = \delta \frac{2P}{a_p \rho_p} \sqrt{\frac{2m_n}{\pi k T_n}}, \tag{3.9}$$

where m_n and T_n are the mass and temperature of the neutral gas species, respectively. In our experiments with argon, $m_n = 6.64 \times 10^{-26}$ kg and $T_n = 298$ K. The coefficient δ ranges from 1.0-1.44 depending on the nature of scattering of neutral atoms, namely specular vs. diffuse reflection. We will assume that $\delta = 1.25$ for simplicity. For MF particles moving at $P = 1.0$ Pa, $\gamma = 1.12$ s^{-1}.

We also consider the ion drag force, F_i, from the rapidly moving ions that are accelerated towards the electrode [94, 96–98]. The ion drag force may be relevant for our experiments since it contains a non-monotonic dependence on the relative dust-ion velocity, and potentially, spontaneous oscillations of dust particles through "negative

damping" in the regime where the force *decreases* with increasing ion velocity [81, 99]. The ion drag force has two components, a collection force, $F_{\rm dir}$, due to direct collisions, and a Coulomb force, $F_{\rm Coul}$, from ions scattered from the Debye shield around the particle [97, 100–104]. In the simple Barne's model of a collisionless plasma [100, 103], these forces are

$$F_{\rm dir} = -\pi a_{\rm p}^2 m_{\rm i} n_{\rm i} v_{\rm i} v_s \left(1 - \frac{2eQ_{\rm eq}}{4\pi\epsilon_0 a_{\rm p} m_i v_s^2}\right), \tag{3.10}$$

$$F_{\rm Coul} = -2\pi b_{\pi/2}^2 m_{\rm i} n_{\rm i} v_{\rm i} v_s \ln\left(\frac{\lambda_{\rm D}^2 + b_{\pi/2}^2}{b_{\rm c}^2 + b_{\pi/2}^2}\right), \tag{3.11}$$

where $v_{\rm s}^2 = v_{\rm i}^2 + v_{\rm th,i}^2$, $v_{\rm i}$ is the ion drift speed, $v_{\rm th,i}$ is the ion thermal speed, $b_{\pi/2} = Q_{\rm eq}e/4\pi\epsilon_0 m_{\rm i} v_{\rm s}^2$ is the impact parameter for perpendicular scattering, $a_{\rm p}$ is the radius of the particle, and $b_{\rm c} = a_{\rm p}(1 - 2b_{\pi/2}/a_{\rm p})^{1/2}$ is the minimum collision parameter. Often the electron Debye length (Eq. 3.5) is used for $\lambda_{\rm D}$ as a rough approximation.

A more sophisticated model [100, 101, 104, 105] builds on this approach by considering scattering outside the Debye sphere and shifted Maxwellian ion velocity distributions. The result is a decrease in the ion drag force by a factor of ≈ 2. However, assuming the Barnes et al. [103] model above (Eqs. 3.10 and 3.11), we estimate the total ion drag force to be approximately one order of magnitude smaller than the gravitational and electrostatic force. For example, as an upper bound on this force in our argon environment, we assume that $Q_{\rm eq} \approx -35,000e$ (see Sec. 3.4.2), $v_{\rm i} \approx 2000$ m/s (Bohm velocity), $v_{\rm th,i} \approx 400$ m/s, $n_{\rm i} \approx 5 \times 10^{13}$ m^{-3}, and the logarithm in Eq. 3.11 is ≈ 4, the total ion drag force is 9% of the gravitational force. In many experiments, the ion density is smaller and the ion velocity is larger than the Bohm velocity in the sheath. Additionally, if we consider the regime where the ion drag force decreases with the ion velocity (where "negative damping" is possible [95]), the size of this effect is 3-4 orders of magnitude too small to explain the oscillations we observe. This can be seen by replacing $v_{\rm i}$ with $v_{\rm i} - v_{\rm p}$, where $v_{\rm p}$ is the particle velocity, and linearizing around $v_{\rm p} = 0$. The result is a force $\sim m_{\rm p}\gamma_{\rm eff} v_{\rm p}$, where $\gamma_{\rm eff}$ is an effective negative damping coefficient of order 10^{-4}, which is much smaller than the real damping coefficient $\gamma \approx 1$ s^{-1}.

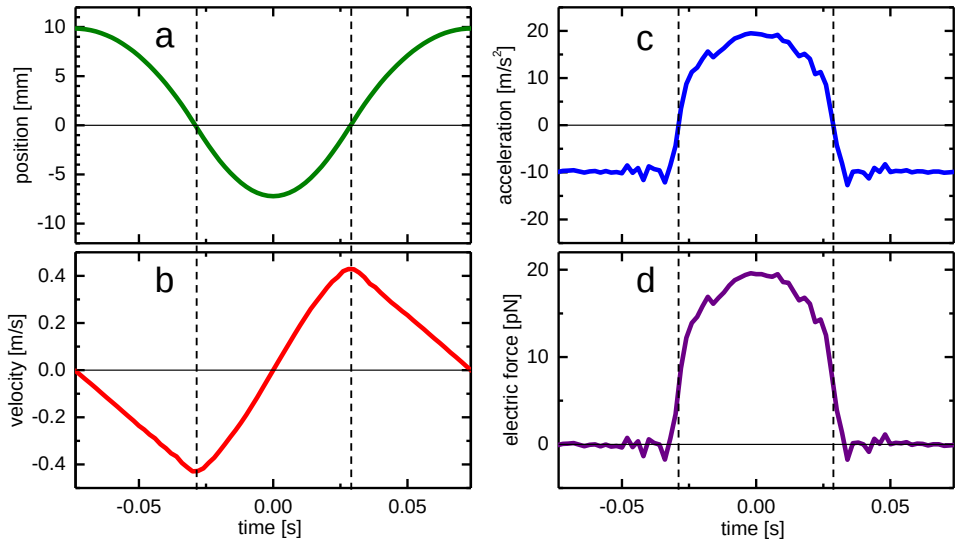

Figure 3.12: (a) Vertical position vs. time for a 9.46 μm diamter MF particle at P = 0.61 Pa. Data has been averaged over 400 oscillation cycles. The equilibrium position of the particle was 14 mm above the electrode surface, and ϕ_w = -28 V (ϕ_{dc} = -6 V). The velocity (b) and acceleration (c) are computed from derivatives of the data. (d) Electrostatic force computed from the data, assuming Eq. 3.12. The dashed lines represent zero net acceleration, where gravity and electrostatic forces are balanced.

3.4.2 Estimate of particle charge

Although Langmuir probe measurements have been used to estimate the floating potential deep in the plasma sheath [106], these measurements may not be reliable enough to estimate the particle charge in our experiments. Thus, we chose to extract the charge from dynamical measurements of the particles' motion under large-amplitude oscillations. Figure 3.12a shows one cylce of the z-position vs. time for a single particle oscillating at P = 0.61 Pa. The data has been averaged over 400 cycles of the steady oscillation in order to reduce noise in calculating derivatives. The velocity and acceleration associated with the position are shown in Fig. 3.12b-c. The position has been adjusted so that zero corresponds to the maximum velocity where the net restoring force is zero.

First, we note that for such large-amplitude oscillations, the particle spends a significant amount of time above the sheath, where the net acceleration is due to

gravity, $\approx$ -9.8 m/s^2. Due to the damping effects of the neutral gas (Eq. 3.9), the particle must receive a net "kick" within the sheath in order to maintain a nearly constant amplitude of oscillation over minutes. If gravity, hydrodynamic damping, and electrostatic forces are the only forces acting on the particle, then the electrostatic force must not be purely conservative, i.e. the charge is not solely a function of position. The time dependence of Q will be discussed in more detail in Sec. 3.4.4.

In order to estimate the particle charge, first we extract the net electrostatic force assuming the equation of motion for the z-position is:

$$m_\mathrm{p}\ddot{z} = -m_\mathrm{p}\gamma\dot{z} - m_\mathrm{p}g + E(z)Q(z,t), \tag{3.12}$$

where $E(z)$ is the spatially-varying electric field in the vertical direction and $Q(z,t)$ is the charge on the particle, which varies with both z and t. Using the velocity and acceleration shown in Fig. 3.12b-c, we compute $E(z)Q(z,t)$ as a function of time. The result is shown in Fig. 3.12d. To a good approximation, the force is symmetric about $t = 0$, so to a good approximation, we can assume that $Q = Q(z)$.

The total electric force is plotted vs. position in Fig. 3.13a. At the equilibrium position, as shown by the vertical dashed line, we can compute the angular frequency of small oscillations, ω_0:

$$\omega_0^2 m_\mathrm{p} = -\left.\frac{d\left(E(z)Q_\mathrm{eq}(z)\right)}{dz}\right|_{z=0}, \tag{3.13}$$

where $\omega_0 = 2\pi f_0$. For the data shown in Fig. 3.13a, $f_0 \approx 13.7$ Hz. The actual frequency of the anharmonic particle motion is significantly smaller than this because of the amount of time the particle spends in free fall above the edge of the sheath. The edge of the sheath is determined by the points where total force goes to zero, which is approximately 1.6 $\pm$ 0.1 mm above the equilibrium position ($z = 0$ mm).

In order to proceed further, we need a model for the electric field, $E(z)$. Self-consistent fluid models for the electrons and ions in the sheath are more accurate for determining the electric field [107–110], but rely on more parameters which are difficult to measure experimentally. Thus, we used perhaps the simplest analytical model for the sheath, which is the Child-Langmuir law [111]:

$$E(z) = \frac{4\phi_\mathrm{w}(1 - z/z_\mathrm{s})^{1/3}}{3z_\mathrm{s}(1 - z_\mathrm{w}/z_\mathrm{s})^{4/3}}, \tag{3.14}$$

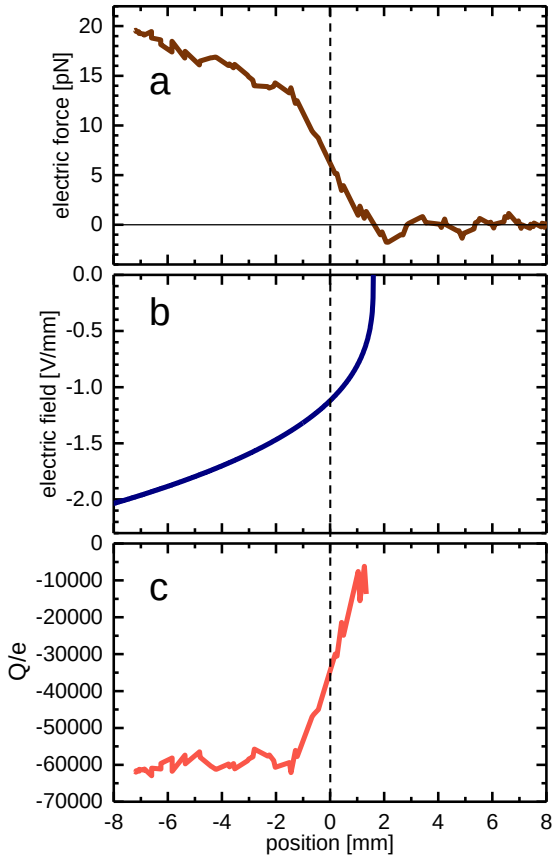

Figure 3.13: (a) Electrostatic force vs. position for an 9.46 μm MF particle at P = 0.61 Pa and ϕ_w = -28 V. The equilibrium position corresponds to $z = 0$. The edge of the sheath occurs at $z \approx 1.6 \pm 0.1$ mm. The oscillations in the data near sheath's edge are due to differentiation of the numerical position data. (b) Electric field computed from Eq. 3.14 with ϕ_w = -28 V, z_s = 1.6 mm, and z_w = -14 mm. (c) Equilibrium charge, normalized by the elementary charge e. This was computed by dividing the data in (a) by the electric field in (b).

where $\phi_w = \phi_{dc} - \phi_p$ is the potential on the conducting wall relative to the plasma potential, z_w is the position of the wall, and z_s is the position of the boundary between the sheath and the pre-sheath. This model is valid for low-pressure, collisionless plasmas where 1) the electrons are significantly depleted in the sheath, and when 2) the kinetic energy gained by the ions in the sheath is much larger than their kinetic energy at the sheath's edge. Given the low pressures and plasma conditions in our experiments ($P < 1$ Pa, $T_e \sim 1$ eV), the plasma can be considered collisionless [112].

Additionally, since the total potential difference across the electrode sheath is rather large, $e\left|\phi_{\mathrm{w}}\right| / k_{\mathrm{B}} T_{\mathrm{e}} \approx 30$, the other two conditions are reasonably satisfied.

For the data shown in Fig. 3.12, ϕ_{w} = -28 V, z_{w} = -14 mm, and $z_{\mathrm{s}} \approx$ 1.6 mm. With these parameters, the electric field is shown in Fig. 3.13a. By dividing the electrostatic force by the electric field, we arrive at an estimate of the particle charge. Figure 3.13b shows the Q/e as a function of position. The charge is relatively constant in the middle of the sheath, near 60,000 electrons, and decreases to $\approx$ 10,000 electrons at the sheath's edge. Although we expect the equilibrium number of electrons to decrease further into the sheath (below z = 8 mm) since the electrons will be significantly depleted, the relatively flat region of constant charge agrees with previous measurements of dust charge in plasma sheaths [110]. The positive slope of the charge near the equilibrium position, $dQ/dz > 0$, is an important feature that will be discussed in Sec. 3.4.4.

At the particle's equilibrium position ($z = 0$). The charge is approximately 35,000 electrons. This agrees extremely well with orbital-motion-limited (OML) theory predictions for $\approx$ 10 μm particles in similar plasma conditions [109, 110]. In Douglass et al. [109], OML theory is applied in the sheath using a shifted Maxwellian distribution of ion velocities and a fluid model for both the electron and ion densities in the sheath. These models usually produce a smoother, extended transition from the sheath to the pre-sheath and bulk plasma. Here we have used the Child-Langmuir law in order to estimate the particle charge, which has a very sharp transition (Fig. 3.13b). The validity of this model should be poor at the sheath's edge where the electron's are not yet depleted. However, given that the force drops sharply to zero (Fig. 3.13a) so that the particle is essentially in free fall (Fig. 3.12c), we surmise that the Child-Langmuir law is reasonable for the plasma environment in our experiments.

3.4.3 Stochastic fluctuations

A number of authors have proposed stochastic fluctuations, either of the plasma environment or of the charge on the particle itself, as a mechanism to generate oscillations [85, 86]. In either case, such fluctuations could turn the particle into a

randomly-forced harmonic oscillator. However, this is inconsistent with our observations since stochastic forcing invariably gives rise to large variations in the amplitude of oscillation. We used stochastic numerical simulations to investigate the effect of plasma environment and particle charge fluctuations on the vertical oscillations. First, we characterized the effect of sheath boundary fluctuations on the vertical oscillations. To illustrate this, we assume the particle motion obeys the following equation:

$$m_{\mathrm{p}}\ddot{z} = -m_{\mathrm{p}}\gamma\dot{z} - m_{\mathrm{p}}g + E(z,t)Q, \tag{3.15}$$

where $E(z,t)$ is an electric field given by the Child-Langmuir law (Eq.3.14). The particle experiences stochastic forcing over time and the relative size of these fluctuations depends on the sheath boundary location, $z_s(t)$ which is a normally-distributed, uncorrelated random variable with mean $\langle z_{\mathrm{s}}\rangle$ and variance δz_{s}^2. Q is the constant charge on the particle and is equal to $\approx -36,000e$ in the simulation.

Stochastic fluctuations of the sheath boundary resulted in spontaneous oscillations of a singl e particle (Fig. 3.14a). Notably, the amplitude varies over time, as expected for a stochastically driven oscillator, drawing a striking difference from our experimental observations (Fig. 3.6a). Fig. 3.14b shows the rms (root mean squared) amplitude of the oscillations as a function of the normalized sheath boundary fluctuations, $\delta z_{\mathrm{s}}/\langle z_{\mathrm{s}}\rangle$. Importantly, an oscillation with a conservative amplitude of 1 mm requires stochastic sheath variations of nearly 60%, meaning that the sheath boundary would fluctuate by $\approx$ 1 mm. Although this is plausible, these fluctuations would be visible withing the plasma environment, and we did not observed any visible changes below the threshold pressure needed to induce oscillations. .

Furthermore, we investigated the effect of charge fluctuations on the vertical oscillations, assuming the sheath position is fixed. We utilized Eq. 3.15 with one modification: the charge is not constant but rather experiences temporal fluctuations. The fluctuations occur around mean $\langle Q\rangle$ with variance of δQ^2. Fig. 3.15a shows temporal evolution of the particle for $\delta Q/\langle Q\rangle \approx 0.1$. As Fig. 3.15b illustrates, even for very large relative charge fluctuations of order 100%, the rms amplitude of oscillations is an order of magnitude smaller than the experimentally observed values. For either mechanism, the required fluctuations are too large and the amplitude too variable to

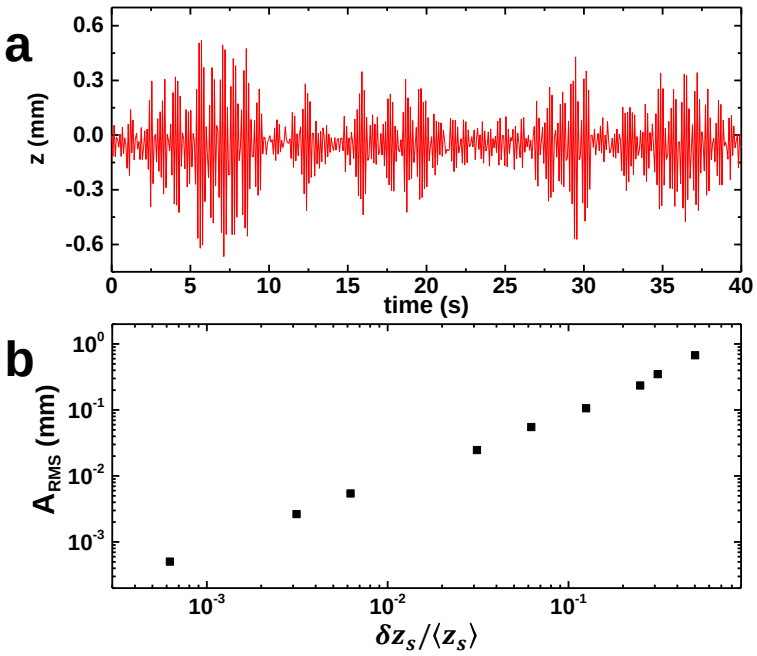

Figure 3.14: (a) The trajectory of a single particle driven by stochastic variations of the sheath boundary (z_s in Eq. 3.19). Parameters for the Child-Langumuir law (Eq. 3.19) were ϕ_w = -28 V, z_w = -14 mm, and z_s = 1.6 mm. The damping constant γ was set to 0.68 s^{-1} and $m_p = 7.85 \times 10^{-13}$ kg. (b) Root mean squared (rms) amplitude of vertical oscillations as a function of the normalized sheath boundary fluctuations.

be consistent with our experiments.

3.4.4 Delayed charging

The experimental data points to a potential mechanism for the large amplitude oscillations without stochastic processes. As first introduced by Nunomura et al. [78], a positive gradient in the equilibrium charge profile can couple to the finite charging time of the particle and produce a net positive work during a single oscillation cycle. However, the amplitude of the oscillations reported in Nunomura et al. [78] were less than 1 mm. A linear stability analysis later showed that the condition for the inception of the instability is for the effective damping constant to be negative [86]:

$$\gamma_{\text{eff}} = \gamma - \frac{1}{2}\left(\frac{EQ'_{\text{eq}}}{(Q_{\text{eq}}E)'}\right)\frac{\omega_0^2}{\nu}, \tag{3.16}$$

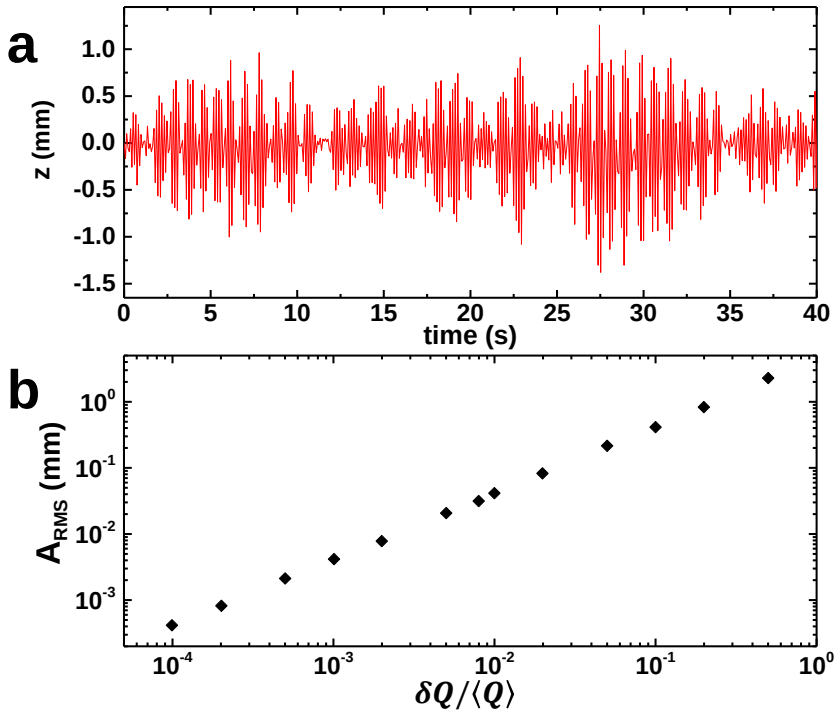

Figure 3.15: (a) The trajectory of a single particle driven by stochastic fluctuations of the particle charge. Parameters for the Child-Langumuir law (Eq. 3.19) were ϕ_{w} = -28 V, z_{w} = -14 mm, and z_{s} = 1.6 mm. The damping constant γ was set to 0.68 s^{-1} and $m_p = 7.85 \times 10^{-13}$ kg. (b) Root mean squared (rms) amplitude of vertical oscillations as a function of the charge fluctuations.

where the primes denote differentiation with respect to z and all quantities are evaluated at the equilibrium position. Here, the fundamental angular frequency is $\omega_0 = 2\pi f_0$, and ν is the charging frequency determined by the collection of ions and electrons on the particle. To linear order, when γ_{eff} is negative, the oscillations will increase exponentially without bound. Obviously the particle oscillations reach some maximum amplitude due to changes in the equilibrium charge profile (i.e. $Q_{\mathrm{eq}}(z)$). As shown in Fig. 3.12d, the particles exit the sheath entirely for much of their oscillation cycle, so that the electric force is zero. Here we combine a simple model for the potential in the sheath and the equilibrium charge with the charging dynamics model from Ivlev et al. [86] to directly compare with the experimental measurements of large amplitude oscillations.

We model the vertical motion of a single, charged particle in a 1D spatially-varying electric field with a time-dependent charge [86, 113]. As in Eq. 3.12, the equation of motion for the particle's vertical position is:

$$m_{\mathrm{p}}\ddot{z} = -m_{\mathrm{p}}\gamma\dot{z} - m_{\mathrm{p}}g + E(z)Q(z,t), \tag{3.17}$$

where $E(z)$ is the spatially-varying electric field in the vertical direction and $Q(z,t)$ is the time-varying charge on the particle, which intrinsically depends on the particle position. The vertical position of the particle is $z(t)$, where $z = 0$ is the equilibrium position determined by electrostatic and gravitational forces.

The charge on the particle follows a simple exponential decay towards its equilibrium value:

$$\dot{Q} = -\nu(Q - Q_{\mathrm{eq}}(z)), \tag{3.18}$$

In the limit $\nu/\omega_0 \to \infty$, the particle always remains at the position-dependent equilibrium charge, $Q_{\mathrm{eq}}(z)$, and a closed path of motion can only result in zero net work done on the particle. However, even if $\nu/\omega_0 \approx 100$, this is still sufficient to cause large-amplitude oscillations, provided that $Q'_{\mathrm{eq}}(0) > 0$ and sufficiently large.

In order to quantitatively interpret the experimental data for a single particle oscillation, we require a spatial model for the electric field in the sheath, $E(z)$, and the equilibrium charge on the particle, $Q_{eq}(z)$. As before (Eq. 3.14), we assume the simplest model for $E(z)$ by using the Child-Langmuir law:

$$E(z) = \frac{4\phi_{\mathrm{w}}(1 - z/z_{\mathrm{s}})^{1/3}}{3z_{\mathrm{s}}(1 - z_{\mathrm{w}}/z_{\mathrm{s}})^{4/3}}, \tag{3.19}$$

where $\phi_{\mathrm{w}} = \phi_{\mathrm{dc}} - \phi_{\mathrm{p}}$ is the potential on the conducting wall relative to the plasma potential, z_{w} is the position of the wall, and z_{s} is the position of the boundary between the sheath and the pre-sheath. Based on our measurements of the particle charge from Fig. 3.13b, we choose a simple cubic function for the equilibrium charge for $-z_0 < z < z_0$:

$$Q_{\mathrm{eq}}(z) = \quad Q_0 + Q_1 z - \frac{Q_1 z^3}{3z_{\mathrm{s}}^2} \tag{3.20}$$

This form ensures a positive slope for the charge at $z = 0$ and zero slope at $z = \pm z_0$. We assume that the equilibrium charge is constant above and below these

values, i.e. $Q_{\rm eq}(z) = Q_{\rm eq}(z_0)$ for $z > z_0$ and $Q_{\rm eq}(z) = Q_{\rm eq}(-z_0)$ for $z < -z_0$. The values of Q_0 and Q_1 are constrained by the two equilibrium conditions

$$\begin{aligned} \omega_0^2 m_{\rm p} &= -\frac{d\left(E(z)Q_{\rm eq}(z)\right)}{dz}\bigg|_{z=0}, \\ m_{\rm p} g &= E(0)Q_{\rm eq}(0). \end{aligned} \tag{3.21}$$

Using these conditions, and solving for Q_0 and Q_1 results in

$$\begin{aligned} Q_0 &= \frac{3m_{\rm p}g(z_{\rm s}-z_{\rm w})^{4/3}}{4\phi_{\rm w} z_{\rm s}^{1/3}}, \\ Q_1 &= -\frac{m_{\rm p}(z_{\rm s}-z_{\rm w})^{4/3}(3z_{\rm s}\omega_0^2 - g)}{4\phi_{\rm w} z_{\rm s}^{4/3}}. \end{aligned} \tag{3.22}$$

The parameters $\phi_{\rm w}$, $z_{\rm w}$, $z_{\rm s}$, and ω_0 are all tightly constrained by experimental measurement (i.e. Figs. 3.12 and 3.13). Thus, in order to fit the data, only ν is a truly adjustable parameter.

Figure 3.16 shows results from the nonlinear regression using time series generated by the model with a particle with diameter 9.46 μm, $\phi_{\rm w} = -28$ V ($\phi_{\rm dc} = -6$ V), $\gamma = 0.68$ s^{-1}, $f_0 = \omega_0/2\pi = 13.7$ Hz, $z_{\rm w} = -14$ mm, and $z_{\rm s} = 1.6$ mm. The spatial variation of the equilibrium charge agrees well with our estimates of the particle charge from the analysis of the particle motion shown in Fig. 3.13c. This provides confidence in the model, and allows for a quantitative estimate of the particle charge, the charging time, and the spatial variation of the equilibrium charge.

Moreover, the model provides an excellent fit to large-amplitude oscillation data, as shown in Fig. 3.16b. We fit the data by solving Eqs. 3.12 and 3.18 with initial conditions $z(0) = 7$ mm, $\dot{z}(0) = 0$ mm/s, and $Q(0) = $ -30,000e using built-in routines in *Mathematica*, then fit the solution with a few cycles of the experimental data once the solution has reached a steady-state value (usually after $t \approx 30$ s). The arbitrary phase offset between the solution and the experiment is automatically adjusted to maximize the quality of the fit. We obtain similar fits for all of our oscillation data.

We again note here that the plasma sheath ends at $z = z_{\rm s} \approx 1.6$ mm (Fig. 3.16a). However, the maximum vertical position is larger that 10 mm. This means that for much of the cycle of motion, the particle is essentially in free fall, with the addition

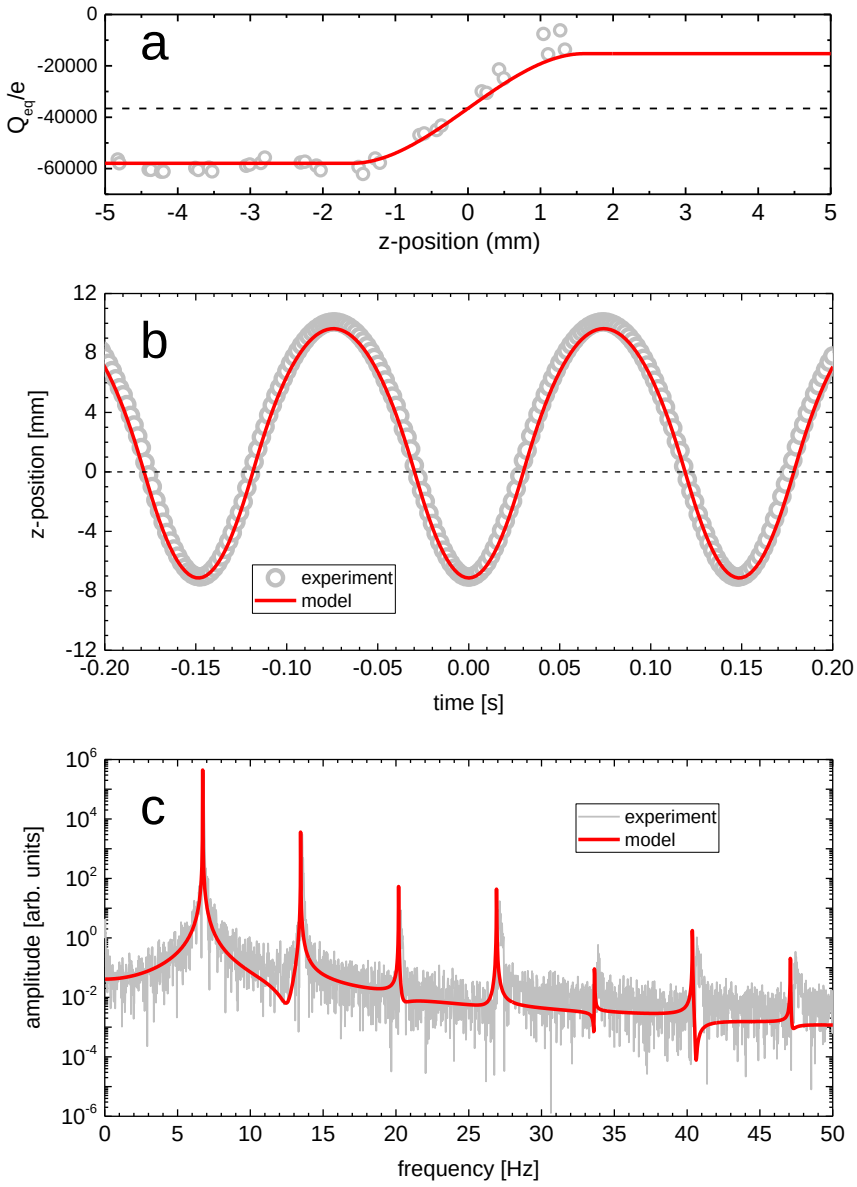

Figure 3.16: (a) Equilibrium charge (number of electrons) as a function of z for the delayed charging model. The equilibrium position of the particle is $z = 0$, and the edge of the sheath is approximately $z = 1.6$ mm. The gray data points are the measurements from Fig. 3.13c. (b) Vertical position of a single MF particle (9.46 μm diameter) as a function of time (gray points). The pressure in the chamber was $P = 0.6$ Pa, and the bias was $\phi_{dc} = -6$ V. The red line is the best fit using the delayed charging model. (c) Fourier transforms of the experimental data (similar to Fig. 3.6b, gray) and the model output (red).

of drag from the neutral gas. As the particle descends further into the sheath, both the magnitude of the electric field and the charge increase, so the total upward force increases significantly, leading to a sort of "bouncing" effect. This explains the strong asymmetry of the motion, and the presence of multiple harmonics in Fig. 3.16b. The model is able to quantitatively capture the entire shape of the Fourier spectrum with no adjustable parameters.

Our nonlinear regression procedure uses the sum of the squares of the residuals (χ^2) as a quality of the fit. We can produce estimates of the errors in ν and $Q'_{\text{eq}}(0)$ by holding one parameter fixed, and minimizing with respect to the other. The 95% confidence interval for the best fit in Fig. 3.16 is $\nu = 1324 \pm 70$ s^{-1}. Thus the characteristic charging time for the particle is $\nu^{-1} \approx 755$ μs, which quite large, but not unrealistic given the environmental conditions (low pressure, low ion and electron density, and relatively low T_e), and is in agreement with estimates of the charging time that accounts for these conditions [114]. This slow charging time, coupled with the gradient in the equilibrium charge, is essentially why the particle oscillation amplitude can become so large in our experiments.

Figure 3.16a shows that the equilibrium charge gradient is $Q'_{\text{eq}}(0)/e \approx 20{,}000$ electrons per millimeter. This is approximately 5 times larger than reported measurements [110]. This discrepancy may by due to the underlying assumptions of our model. In Fig. 3.13c, the charge measurements are based on motion analysis of the particle, and a model for the electric field in the sheath. This is the largest unknown in our measurements. Without experimental characterization of the sheath potential, which is quite challenging, measurements of the particle charge can not be decoupled from the model of $E(z)$. In addition, the measurements of ν from the delayed charging model depend on $E(z)$. Nevertheless, delayed charging is able to provide the "kick" in the sheath necessary to maintain oscillations with a surprisingly regular amplitude, although constraining $Q_{\text{eq}}(z)$ and ν require an accurate model of $E(z)$.

3.5 Conclusion

The spontaneous oscillations of micron-sized particles in a plasma sheath has been a topic of active research for more than 20 years. However, multiple, disparate mechanisms have been invoked to explain their origin. Although it may be that not all oscillations share the same initiation mechanism, many observations have shown that the oscillations begin below a threshold pressure where the effective damping becomes exceedingly small. Using a combination of high-speed video, Langmuir probe measurements, and numerical modeling, we investigated the largest-amplitude oscillations reported to date. The peak-to-peak amplitude can reach more than 2 cm, is strongly anharmonic, and has a remarkably consistent amplitude over minutes timescale. The Langmuir probe measurements suggested that the plasma environment is quite stable at frequencies below 1000 Hz, and the consistency of the oscillations pointed toward a non-stochastic origin for the input of energy into the particle motion. Although our model of delayed charging was able to reproduce the motion of the particle with exquisite accuracy, the model's necessary gradient in the equilibrium charge on the particle is approximately 8 times larger than experimentally measured values.

We suspect that any mechanism that leads to an effective "negative damping" can give the particle a kick in the sheath and will produce oscillations consistent with our observations. Delayed charging is the most likely candidate, but more direct measurements of the charging time would confirm this. We note that not all oscillations may be the same. For instance, Samarian et al. [81] observed oscillations in multi-particle layers for pressures as high as 5 Pa. Taking together the collective set of observations and corresponding models over the last 20 years, we emphasize that a good model for the ion and electron densities and velocity distributions in the sheath is extremely important, considering their influence on the local potential and charging dynamics. The gradient in the equilibrium charge is quite sensitive to the choice of model and is crucial for the delayed charging mechanism. The collective influence of multiple particles undergoing spontaneous oscillations remains an open question since the local plasma environment is affected by the density of particles.

Chapter 4

Molecular Dynamics Simulation

Part of the material presented in this chapter was published in:
• Gogia, Guram, and Justin C. Burton. "Emergent Bistability and Switching in a Nonequilibrium Crystal." Physical Review Letters 119.17 (2017): 178004.
Another part is under review process at Physical Review Research. The arxiv preprint can be found: • Gogia, Guram, Wentao Yu, and Justin C. Burton. "Intermittent" Turbulence" in a Many-body System." arXiv:1901.10567 (2019).

4.1 Introduction

As mentioned previously, the state of plasma is characterized by a plethora of forces that are potentially influencing experimentally observed intermittent switching. In order to understand the essential elements necessary for the emergent behavior, one needs to eliminate a large class of irrelevant variables. Such frameworks are called minimal models [48, 115], which are usually regarded as caricatures of real systems, but capture the salient features of a given phenomenon. For example, the minimal model known as Gas Lattice Automaton (GLA), which is based on a hexagonal lattice, can accurately simulate large-scale patterns observed in fluid flows [116]. For our system, we identified two main components - driving, as manifested by the spontaneous vertical oscillations, and quenched disorder that contributes to the emergence of intermittent switching. The intuition behind the first component lies

in the necessity of energy for the self-evident "phase transition" between crystalline and gas-like states. Quenched disorder is essential as the melting usually commences from one of the defects. Unfortunately, modifying the number of particles and their size distributions is close to an impossible task in these experiments. Thus, in order to investigate the dependence of intermittent switching behavior on the interplay between dynamic and structural features of the system, with the intention of eventually characterizing a minimal model, we utilized molecular dynamics simulations to characterize the system behavior under various conditions.

4.2 Electrostatic Simulation

We start with modeling the experiment by treating the dust particles as charged spheres that interact via shielded Yukawa potential, which is given by

$$U_{int} = k\frac{q_i q_j}{r_{ij}} \exp^{-\frac{r_{ij}}{\lambda_D}}, \tag{4.1}$$

where k is the Coulomb constant, q_i and q_j are charges of i-th and j-th particles and r_{ij} is the distance between the charges. λ_D is the Debye screening length and is set to $1mm$. The charge on the particles set by the plasma potential, V:

$$q = 4\pi\epsilon V a, \tag{4.2}$$

where ϵ is the vacuum permittivity and equals to $8.85{*}10^{-12}$ F/m and a is the particle radius. The particles are confined by harmonic potentials in vertical and horizontal directions. The strength of confinement is set by the gradient in the electric field, denoted by χ_V for the vertical direction and χ_H for the horizontal direction. The confining potential in the vertical direction is given by

$$U_V = -\frac{1}{2}\chi_V q z^2, \tag{4.3}$$

where q is the particle charge and z is the deviation from the equilibrium levitation height of the particle. Similarly, the horizontal confinement is defined as the following: $U_H = -\frac{1}{2}\chi_H q r^2$, where r is the radial distance from the geometric center of the sample $r^2 = x^2 + y^2$.

Quenched disorder is introduced to the system by setting the particles sizes according to normal distribution, which is characterized by the coefficient of variation, c_V, a ratio of the standard deviation and the mean of particle sizes. Particles are initially placed at random locations in the xy-plane and subsequently quenched to the nearest local potential energy minimum in three dimensions using the FIRE algorithm [117]. The anisotropic confinement ($\chi_V \gg \chi_H$) leads to a natural separation of normal mode frequencies (more about this later) associated with in-plane and out-of-plane motion, yielding a monolayer of the crystalline layer. The Fortran code for the electrostatic simulation is presented in Appendix A1.

Intermittent behavior is recreated by the addition of two non-conservative forces in the system: 1) hydrodynamic damping force, which in experiments arises due to momentum transfer to the neutral atoms and 2) the stochastic force in the vertical direction to induce spontaneous oscillations. The damping force is proportional to the velocity, v, of the particles and is given by

$$\vec{F}_d = -\gamma m \vec{v}, \tag{4.4}$$

where γ is the Epstein damping coefficient and m is the mass of a particle. The stochastic Langevin force, commonly referred to as white noise, is given by

$$\overrightarrow{F_n} = \eta(\beta, t) m \sqrt{\Delta t_0 / \Delta t} \hat{\mathbf{z}}, \tag{4.5}$$

where $\eta(\beta, t)$ is a random number chosen at each time step from a Gaussian distribution with standard deviation β, Δt is the time step in the simulation, and $\Delta t_0 = 0.001$ s. Even though in the experiments the vertical oscillations do not arise due to stochastic effects, neither is energy supply in the pipe flows noisy, we still used stochastic driving in order to avoid losing the overall generality. The particle positions and velocities were advanced in time using a velocity-Verlet integration. Given the large parameter space, we used $\gamma = 0.2 s^{-1}$, $\beta = 0.5 m/s^2$, $V_p = -6V$, and $c_V = 1.25\%$ as default parameters unless otherwise noted. The Fortran code for the molecular dynamics simulation can be seen in Appendix A1.

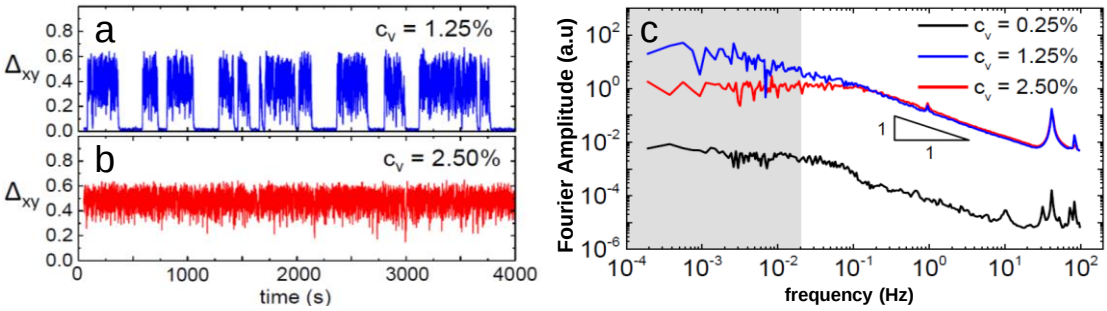

Figure 4.1: Temporal evolution of Δ_{xy} for (a) $c_V = 1.25\%$ and (b) $c_V = 2.50\%$. (c) Fourier transform of Δ_{xy} from (a),(b) and one for $c_V = 0.25\%$.

4.2.1 Characterizing Intermittent Switching

Even though qualitatively it is easy to differentiate between melted and crystalline states, we needed a quantitative measure to characterize the extent of switching in the system. The quantity we chose was fractional kinetic energy in the horizontal plane,

$$\Delta_{XY} = \frac{KE_{XY}}{KE_{XY} + KE_Z}, \tag{4.6}$$

where KE_{XY} and KE_Z are kinetic energies per particle in the horizontal and vertical directions, respectively. The reason behind our choice was that Δ_{XY} is always between 0 and 1 Fig. 4.1a-b, enabling comparison of system dynamics under different conditions. Exploration of the parameter space led us to a surprising finding. For a fixed stochastic driving amplitude, the system exhibits switching behavior for a very narrow range of quenched disorder. Namely, the system switches between crystalline and gas-like states for $0.75\% < c_V < 1.5\%$ ((Fig. 4.1a), whereas for $c_V < 0.75\%$, it remains crystalline and finally, for $c_V > 1.5\%$ the system exists in a perpetually melted state (Fig. 4.1b). This closely resembles the transitional turbulent flow in a pipe, where the intermittent behavior sensitively depends on the wall roughness of the pipes. Effectively, the quenched disorder, which serves the role of the wall roughness, enabling the nucleation of the "turbulent" state.

With the intention of quantifying the system-wide switching behavior using a single parameter, we first calculated the Fourier transforms of Δ_{XY}. As we are interested

in *long time-scale behavior*, we integrate the area under the curves of Fourier transforms for *low frequencies* (smaller than 0.02Hz). We denote the integrated area as switching intensity, I (Fig. 4.1c) and is defined as the following:

$$I = \int_{-\infty}^{2\pi/50} F(\omega) d\omega, \tag{4.7}$$

where $F(\omega)$ is the amplitude of Fourier transform for frequency ω. The integration limits correspond to switching timescales of 50 s and larger. As a matter of fact, we came up with this quantity and we are not aware of a similar quantity being studied in the turbulence literature. However, it might be useful to quantify spatio-temporal intermittent dynamics using statistics of Fourier modes. We characterized the switching intensity for a range of values of β and c_V. Figure 4.2a presents a heatmap of switching intensity for a polydisperse system for a range of c_V and β. As one can see on the switching intensity heatmap, the switching is maximal for intermediate values of structural disorder and environmental noise. One can also notice the traces of some functional form for the region, where the switching is maximized. This will be discussed in greater detail in Section 4.5.

In order to study the role of disorder in greater detail, in addition to polydisperse systems, we investigated the dynamics of bidisperse ones as well. We create bidisperse systems by replacing N_α (out of 500) particles of radius r with ones of radius $\alpha \times r$. The dynamics of the bidisperse systems were subjects of interest to us, as they are commonly utilized in computational and experimental studies of colloidal glasses[118, 119], where size discrepancy between two species of particles prevents system-wide crystallization. Another reason for studying the bidisperse systems was microscopy measurements of particle sizes, revealing existence of a second "hump" in the distribution of particle sizes, as illustrated in Fig. 4.3.

The heatmap of switching intensity as a function of α and N_α for bidisperse systems under constant driving ($\beta = 0.52m/s^2$) is presented in Fig. 4.2. There are also visible bands of regions where the switching intensity is maximized. The location of these bands depends on the intensity of driving, but there are still some universal features. Nameely, for very small α, the system is effectively monodisperese, thus it would be impossible to trigger a "turbulent" state

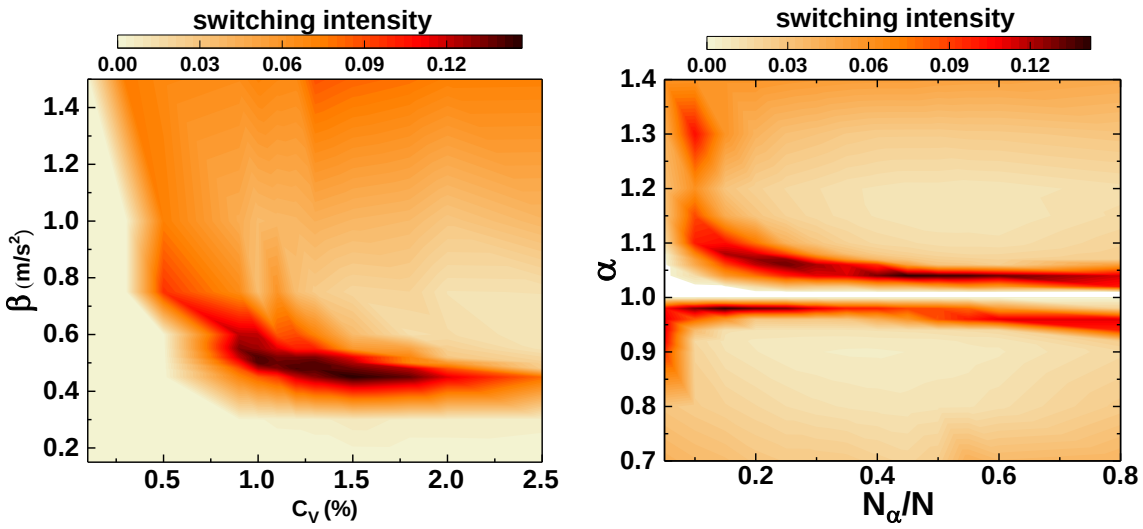

Figure 4.2: Heatmaps of switching intensity for a polydisperse system (left) as function of β and c_V and a bidisperse system (right) for $\beta = 0.52m/s^2$ as function of α and N_α.

4.2.2 Melting due to Scattering and Early Warning Signals

Prior to the transition to a gas-like state, most of the mechanical energy in the condensed phase exists at high frequency, coherent, vertical oscillations ($\Delta_{xy} \ll 1$). The transition occurs through a nucleation event and a subsequent energy cascade that redistributes the mechanical energy into low frequency, horizontal oscillations. This process closely resembles the generation of turbulent puffs in transitional flow, where either localized disturbance or rough walls induce turbulent puffs. We simplified the geometry of the system in order to better characterize the nucleation event. Fig. 4.4 presents the evolution of the fractional horizontal kinetic energy for a chain of 6 particles. We found that the nucleation event comes in the form of a nonlinear scattering of two particles (Fig. 4.4Inset III) when their separation is too small. The melting front propagates through the crystalline layer, which quickly melts into a gas-like phase. The particles behave as under-damped harmonic oscillators driven by noise. As such, they each respond sharply at their fundamental frequency, which varies with particle size. Neighboring particles can eventually oscillate out-of-phase,

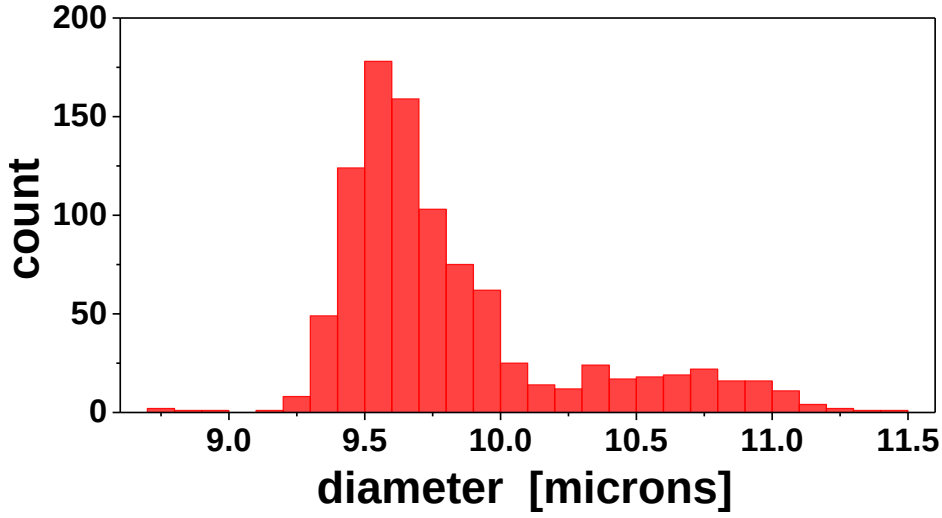

Figure 4.3: Typical particle size distribution for melamine-formaldehyde particles with nominal diameters of 9.46 μm (as reported by the manufacturer). The results were obtained by bright-field optical microscopy. The mean of the distribution is 9.83 μm and the median is 9.67 μm. The discrepancy between our measured values and the manufacturer-provided values is due to diffraction-limited imaging of the particles' edge, making the particles appear 2-3% larger than they actually are.

increasing the chances of a scattering event (Fig. 4.4 Inset II-III). If all the particles are driven sinusoidally, they oscillate at the same driving frequency with no relative phase, suppressing the scattering of neighboring particles. Additionally, if the particles are individually driven with spatially uncorrelated noise, the system transitions to a gas-like state quickly since energy can no longer be pumped into the center-of-mass motion of the entire system.

For our system, the scattering event represents a tipping point leading to a "regime shift" from the crystalline to "turbulent" state. In various complex dynamical systems, such as climate, vegetation and financial systems, tipping points are usually foreshadowed by a critical slow-down, as measured by an increase of variance and/or auto-correlation of state variables [120, 121]. Recent studies have shown that for spatially extended systems, the early warning signals for a critical transition can be extracted from the emerging spatial, rather than temporal, patterns [122–124]. We were able to determine one spatial parameter for our system that would characterize

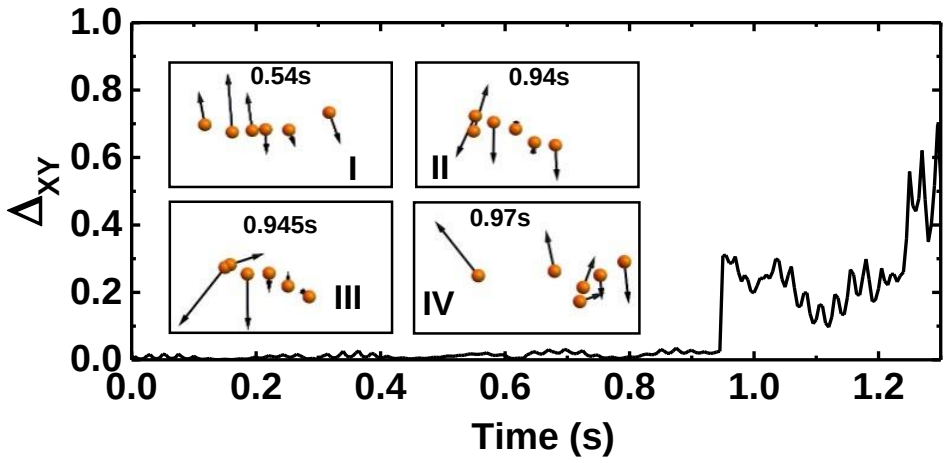

Figure 4.4: Evolution of fractional horizontal kinetic energy Δ_{xy} for a one-dimensional system of six particles. Inset: a scattering event (III) leads to a sharp increase in Δ_{xy} due to energy redistribution to the horizontal direction. The coefficient of variation of the particle sizes is 2%.

the approach to the critical transition - minimal horizontal distance, δ_{min}, between *any* two particles in the layer. Two particles may collide and scatter due to mutual electrostatic repulsion when their separation is small. Fig. 4.5a-b shows the evolution of Δ_{xy} and δ_{min} for a bidisperse system. Δ_{xy} increases dramatically when $\delta_{min} \to 0$, verifying that the scattering event is necessary for the transition to the gas-like state. Moreover, δ_{min} experiences a gradual, rather than abrupt, decrease *prior* to the transition. Thus, δ_{min} holds some predictive power of the impending regime shift.

The melting transition can also be characterized by the more conventional Lindemann criterion[125], which suggests that the mean squared displacement (MSD) of particle motion must exceed some critical fraction, κ_c, of the lattice constant, usually ranging from $\kappa_c \approx 0.15$-0.3 [126]. For two-dimensional crystals, $\kappa_c \approx 0.17$. We calculated the normalized, horizontal MSD averaged over 1 s of motion: $\langle d \rangle = \sqrt{\langle \Delta x^2 + \Delta y^2 \rangle} / \langle r_{ij} \rangle$. Fig. 4.5c shows $\langle d \rangle$ for two cycles of switching and finds that the critical threshold that system needs to cross in order to melt and enter a "turbulent" state is indeed ≈ 0.17.

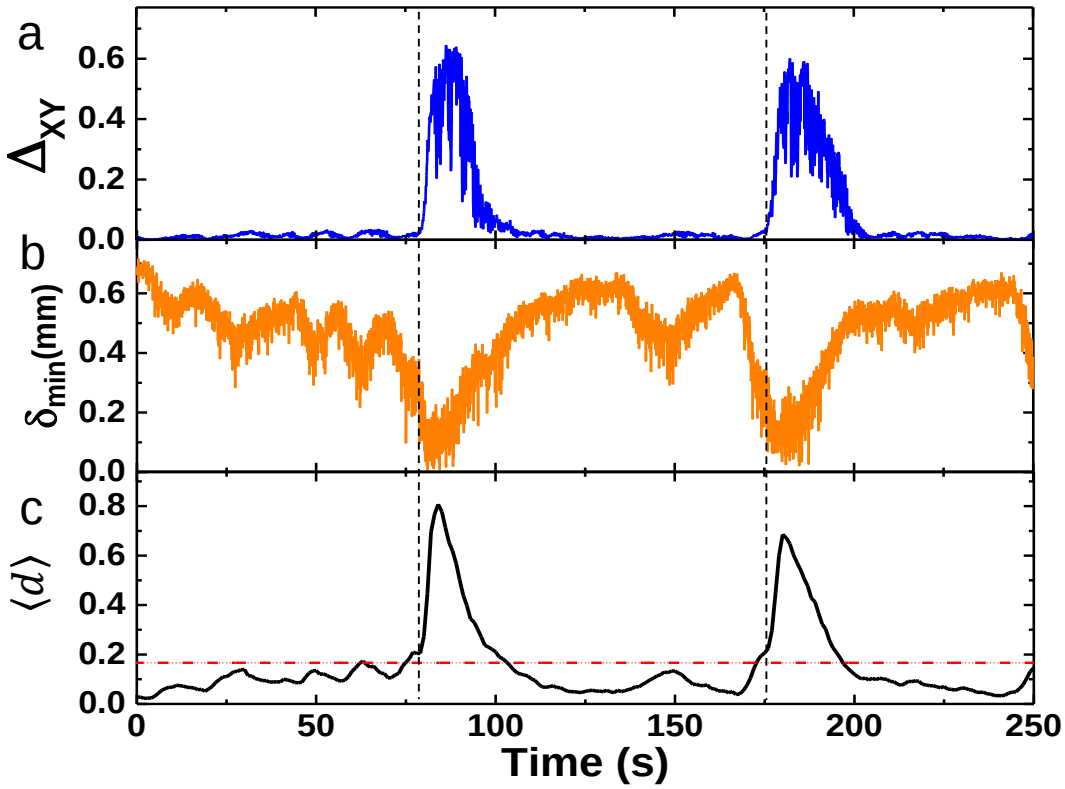

Figure 4.5: (a)Temporal evolution of Δ_{xy}, (b) minimum horizontal distance between any two particles (δmin) and (c) horizontal mean-squared displacement (MSD) divided by the average inter-particle spacing for a bidisperse system of N = 500 particles with $N_\alpha = 80$ and $\alpha = 1.08$. The dotted red line in (c) corresponds to the critical threshold (0.17), above which the system melts, in analogy to the Lindemann criterion.

4.3 Simplified Molecular Dynamics Simulation

Once we found a working model with essential elements, we considered to further simplify it. First, we got rid of the colloidal particle features: instead of simulating spheres of finite radius, we modeled them as point masses that are confined by spring-like harmonic potentials in horizontal and vertical directions. This allowed us to simplify the form of interaction potential. $U(r) = U_0 \lambda e^{-r/\lambda}/r$, where U_0 is the characteristic energy scale, r is the particle separation, and λ is the screening length.

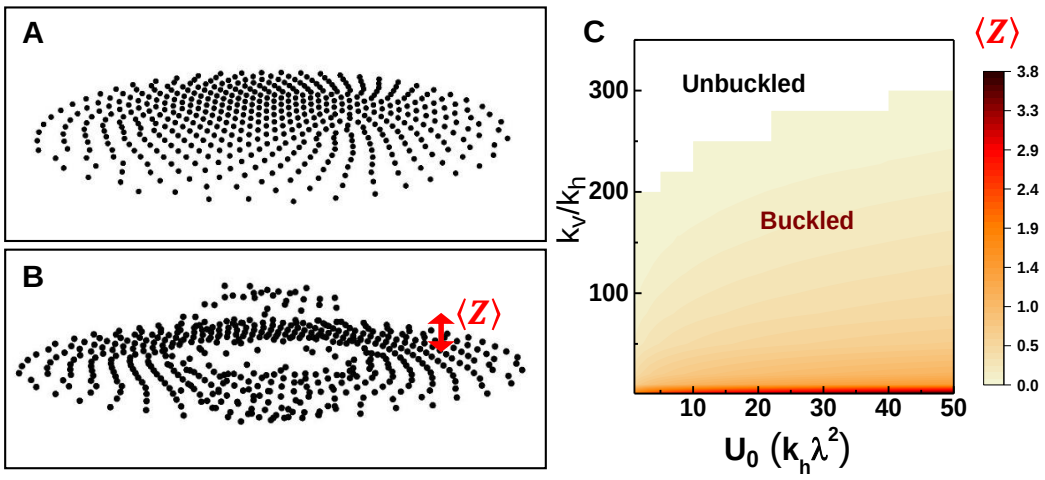

Figure 4.6: (A) A monodisperse system comprised of 500 particles in an unbuckled configuration under $k_v = 800$ and $U_0 = 19$. Reducing vertical confinement, $k_v = 150$, results into a (B) buckled phase. (C) Buckling was quantified by measuring average vertical distance of deviation from the particle plane $\langle Z \rangle$ for a monodisperse system for a range of U_0 and k_v/k_h.

The general form of the interaction potential stayed the same. The particles are spatially confined vertically and horizontally through harmonic potentials, $k_v z^2/2$ and $k_h(x^2 + y^2)/2$, where k_v and k_h are the respective spring constants.

The confinement needs to be stronger in the vertical direction in order to obtain a uniform crystalline layer (Fig. 4.6a). Otherwise, if k_v/k_h is not large enough, the layer will buckle (Fig. 4.6b). We actually quantified the extent of buckling by measuring the average vertical deviation from the layer plane while varying U_0 and k_v/k_h. If a system is buckled, it is impossible to coherently pump energy into the vertical direction, preventing any consequent redistribution of energy. This situation is analogous to pipe flow where the wall roughness is on the same order of magnitude as the diameter of the pipe. Such a scenario does not allow a coherent supply of energy to the fluid in the pipe.

We also include the same two non-conservative forces as before: neutral drag force, $\vec{\mathbf{F}}_d = -\gamma m \vec{\mathbf{v}}$, where γ is the dissipation rate, and a simplified form of a spatially-uniform Langevin force in the z-direction to stimulate vertical oscillations,

$\vec{\mathbf{F}}_s = \hat{\mathbf{z}} w(t)\sqrt{m\phi/\Delta t}$, where $w(t)$ is a Wiener process with zero mean and unit standard deviation, ϕ is the power delivered by the noise, and Δt is the simulation time step. The particle positions and velocities were advanced in time using velocity-Verlet integration.

We introduce the quenched disorder by distributing the masses of the particles with a Gaussian distribution with mean m and coefficient of variation c_v. With all-of-the-above parameters, we identify a characteristic mass (m), length (λ), and time ($\sqrt{k_h/m}$) scale in the system. In what follows, all variables have been scaled by these units. The intermittent dynamics are realized through punctuated cascades of energy from the vertical to the horizontal degrees of freedom. We also use the fractional horizontal kinetic energy, $\Delta_{xy} = KE_{xy}/(KE_z + KE_{xy})$, to characterize the switching behavior as shown in Fig. 4.1c. The Fortran code for the simplified simulation is presented in Appendix A2.

4.4 Localized Vibrational Modes

The observed intermittent dynamics in our system arise from the system's inherent nonequilibrium and nonlinear nature. Nevertheless, an analysis of the harmonic vibrational modes in the system are a powerful tool to determine how quenched disorder facilitates switching between "laminar" and "turbulent" states. We used dynamical matrix formalism to calculate the normal modes of the system [127–129]. The weighted Hessian matrix, K, was computed about this equilibrium position using $K_{ij} = \frac{\partial^2 V_{ij}}{\partial r_i \partial r_j}$, where V_{ij} is the total potential energy of i-th and j-th particles. Using harmonic approximation around the equilibrium position vector $\vec{x_0}$, Newton's 2nd law yields

$$M\ddot{\vec{x}} + K\vec{x} = 0 \tag{4.8}$$

For N particles in 3 dimensions, M and K are $3N \times 3N$ matrices and x is the $3N \times 1$ vector. The dynamical matrix, $D = K/M$ has 3N eigenvalues which correspond to squares of mode frequencies and the normalized eigenvectors represent the polarizations of the particle displacements. Fig 4.7 presents density of states for

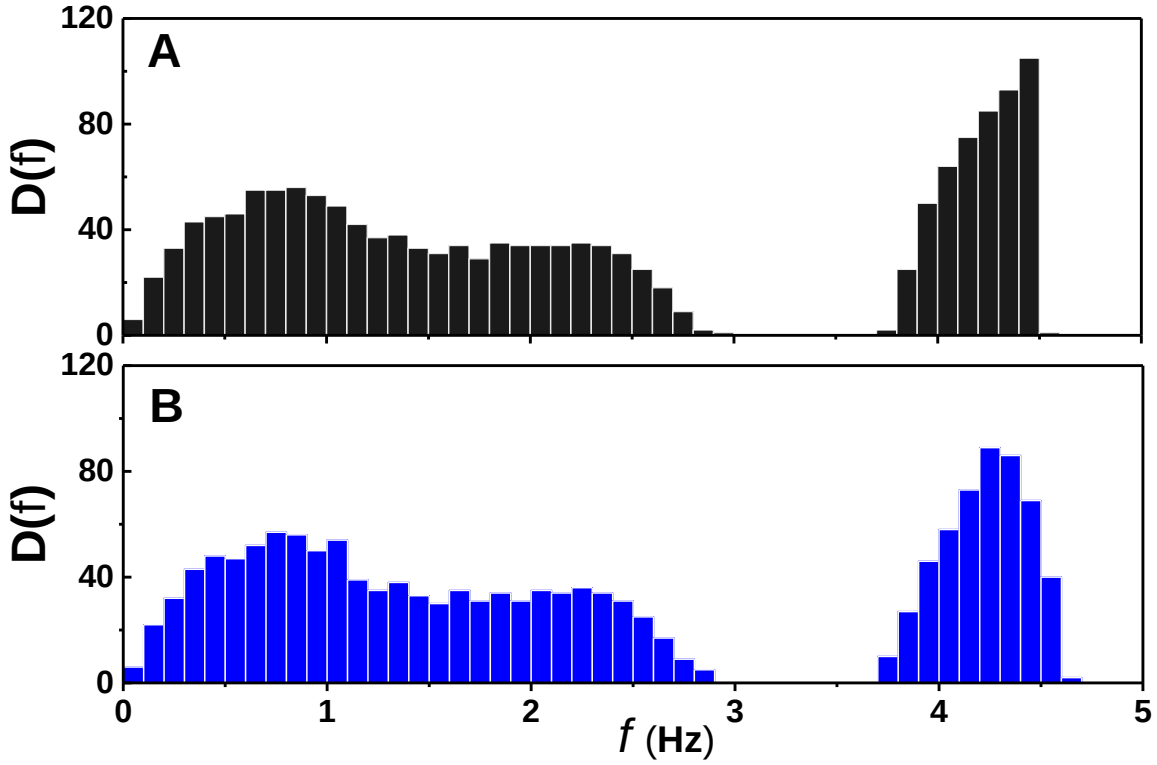

Figure 4.7: The density of states for a completely monodisperse ($c_V = 0\%$) (a) and polydisperse ($c_V = 4\%$) samples.

completely monodisperse ($c_V = 0\%$) and polydisperse ($c_V = 4\%$) samples. In both cases, there are two separate frequency bands corresponding to vertical and horizontal modes. The gap between the two bands is key to maintaining a crystalline order since it suppresses the transfer of energy from vertical to horizontal degrees of freedom. Horizontal frequency bands are almost identical for polydisperse and monodisperse samples, whereas vertical modes in a polydisperse system are more spread out. However, the density of states does not hold any information about the spatial features of the modes. In order to characterize the spatial extent of each mode, we calculated the participation ratio, p_r, for each eigenvector. p_r characterizes the

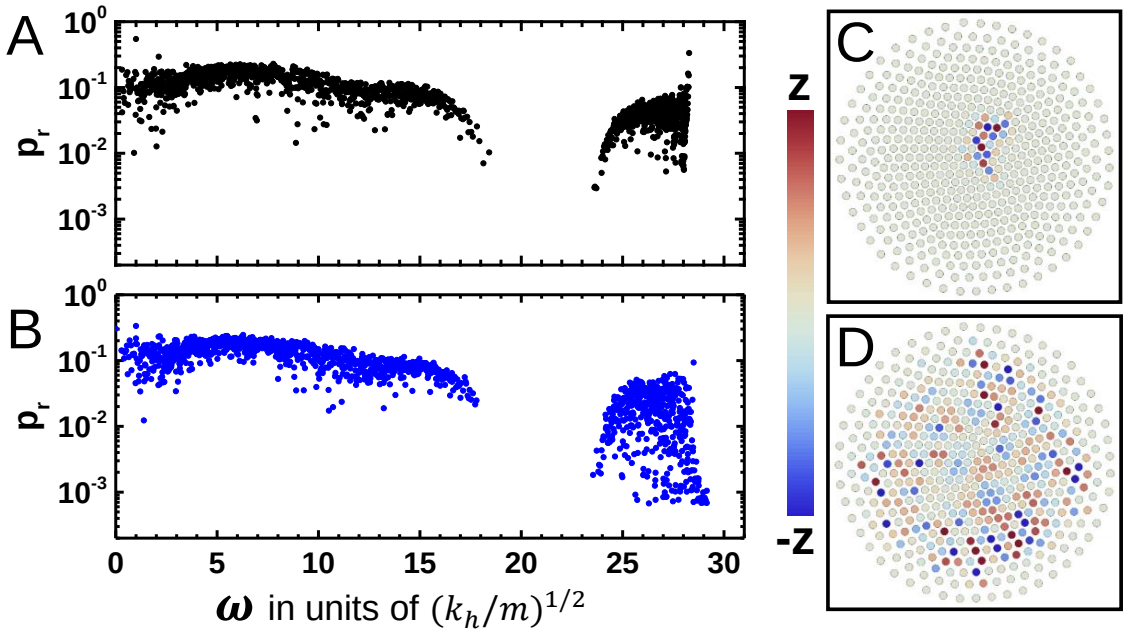

Figure 4.8: Participation ratio (p_r) vs. mode frequency for a monodisperse (A) and a polydisperse (B) system. The dashed red line corresponds to the lowest value of p_r in the monodisperse sample. Vertical polarization for two modes (low-p_r (C) and high-p_r (D)) in a polydisperse system with $c_v = 4\%$.

fraction of particles participating in a given vibrational mode:

$$p_r = \frac{(\sum_i |\hat{\mathbf{e}}_{m,i}|^2)^2}{N \sum_i |\hat{\mathbf{e}}_{m,i}|^4}, \tag{4.9}$$

where $\hat{\mathbf{e}}_{m,i}$ is the polarization vector of the i-th particle in the m-th unit eigenvector. The modes with p_r close to unity represent the coherent motion of a large fraction of particles, whereas the modes with $p_r \ll 1$ correspond to the motion of only a few particles. Fig. 4.8a-b shows p_r versus mode frequency for three different systems comprised of 500 particles: monodisperse (A) and polydisperse (B). High frequency modes near $f \approx 25$ correspond to vertical motion, and the low frequency modes with $f < 20$ correspond to horizontal motion. Polydisperse quenched disorder leads to localized modes with $p_r \ll 1$ in the vertical frequency band, whereas the horizontal frequency band remains nearly the same. Upon excitation with spatially-

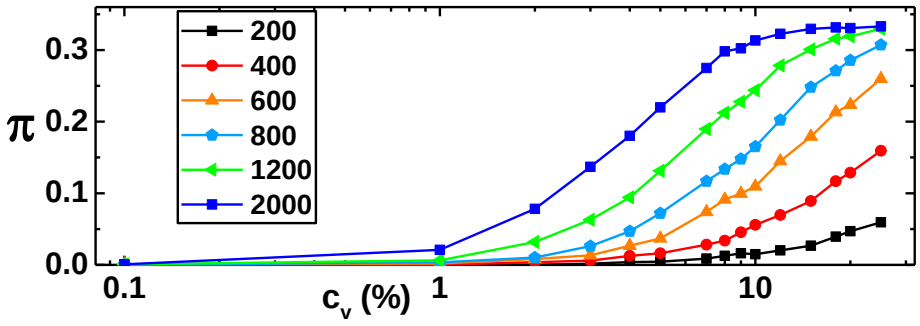

Figure 4.9: Fraction of vertical modes with low-p_r as a function of c_v for different values of k_v/k_h, as indicated by the legend.

uniform (wavevector $k = 0$), stochastic noise, these low-p_r modes are excited since they contain low-k Fourier components. Additionally, since there are fewer particles participating in these modes, their amplitude of motion is larger, and thus more susceptible to nonlinearities and coupling to other modes in the system. In this way they serve as the progenitors of the energy cascade from vertical to horizontal motion.

Furthermore, we quantified the fraction of vibrational modes with p_r below the lowest value for a monodisperse sample ($c_v = 0$), as shown by the dashed red lines in Fig. 5.2A-B. This fraction increased monotonically with the amount of disorder, but also increased with the ratio of vertical to horizontal confinement, k_v/k_h. This is illustrated in Fig. 4.9. For strong confinement, the energy gap between the frequency bands is large and a small amount of disorder can quickly lead to mode localization. For very weak confinement, the frequency gap is small or nonexistent and structural disorder induced by the circular confinement of a hexagonal crystal is a more determinant factor in mode localization. For all the data shown in Fig. 4.9, intermittent switching occurs when the fraction of modes is approximately 0.07–0.2. In this manner, the linear, equilibrium properties of the system can inform the system's response to nonequilibrium, noisy conditions [130].

4.5 Nondimensional Analysis

In order to better characterize dynamical behavior in this system, we identified 5 relevant dimensionless numbers through Buckingham's Pi theorem: c_v, k_v/k_h, $U_0/k_h\lambda^2$, $k_v/m\gamma^2$, and $\phi/k_v\lambda^2\gamma$. The first number, c_v, characterizes the degree of disorder in the system. The next two, k_v/k_h and $U_0/k_h\lambda^2$, determine the degree of quasi-2D confinement. If either number is too small, then the system's equilibrium configuration will be "buckled" into the z direction (Fig.4.6). The 4^{th} number, $k_v/m\gamma^2 \gg 1$, determines the quality factor of under-damped vertical oscillations. The last number, $\phi/k_v\lambda^2\gamma$, is the only number associated with external forcing. A value of order unity can be intuited as the amount of noise necessary for a stochastic, damped harmonic oscillator to reach an average amplitude λ, $k_v\lambda^2/2 = \phi/4\gamma$ (Fig.4.11a) . This amplitude threshold, λ, is necessary since particles must be displaced an amount on the order of the equilibrium separation in order to induce structural rearrangements, similar to the Lindemann criteria in classical melting [125]. For a thermal, Brownian oscillator, $2\gamma k_{\text{B}}T$ would assume the role of ϕ in our simulations. This is clearly illustrated in Fig. 4.11a, where the root-mean-square (rms) amplitude of the oscillation amplitude scales as $\sqrt{\phi}$. This bares a striking resemblance to rms amplitude of Brownian motion scaling as $\sqrt{k_{\text{B}}T}$ [131].

We can form a single dimensionless number that describes the system-wide, intermittent dynamics by considering the role of disorder on the vertical oscillations. Since each particle has a slightly different mass, their vertical frequencies would vary by $\Delta\omega$:

$$\omega_v + \Delta\omega_v = \sqrt{k_v/(m + \Delta m)} \sim \omega_v(1 - c_v/2), \tag{4.10}$$

where $c_v = \Delta m/m$. For this frequency difference to be significant, $\Delta\omega_v$ must be larger than γ, which determines the broadness of particles' response in frequency space. If γ is too large, the oscillators will be strongly coupled, preventing out-of-phase oscillation of neighboring particles and the consequent melting of the crystal. This single-particle picture also applies to the harmonic vibrational modes illustrated in Fig. 5.2A-B. Modes with significant spatial overlap will also be strongly coupled if γ is too large. Consequently, by multiplying the stochastic forcing, $\phi/k_v\lambda^2\gamma$, by the

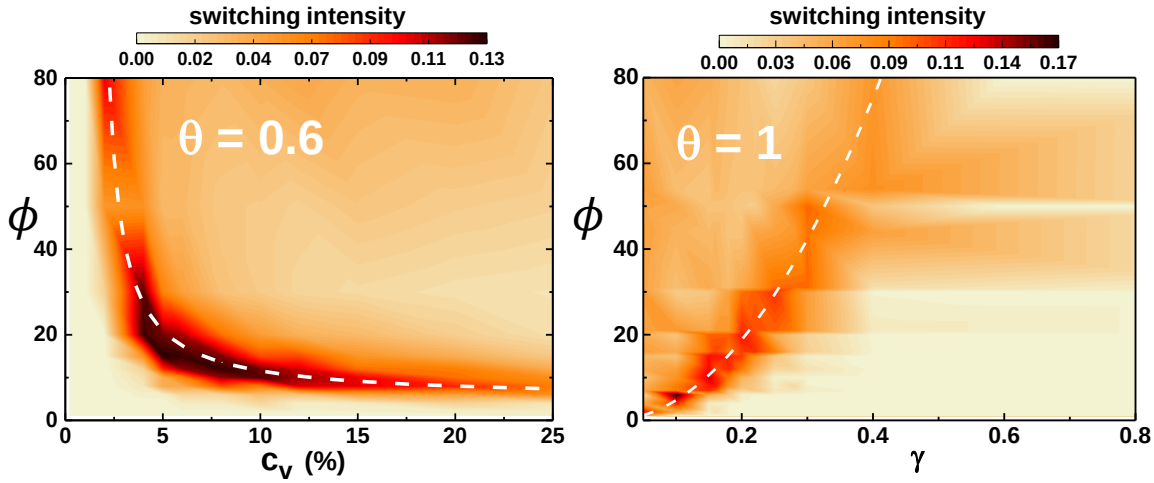

Figure 4.10: (Left) Heatmap of switching intensity of Δ_{xy} for a range of ϕ and c_v with $\gamma = 0.2$. (Right) Heatmap of switching intensity of Δ_{xy} for a range of ϕ and γ with $c_v = 6\%$.

disorder in frequency space, $c_v\omega_v/\gamma$, we obtain

$$\theta = \frac{c_v\phi}{\sqrt{k_v m}\lambda^2\gamma^2}. \tag{4.11}$$

This dimensionless number characterizes the strength of energy input to dissipation, modulated by disorder. θ has a similar physical form as Re (ratio of inertial and dissipative terms) and it effectively incorporates the contribution from the structural heterogeneities. For the fluid flow in a pipe, wall roughness was included into Re only recently in Ref. [17]. It has been conceptualized as a parameter inducing critical dynamics [132, 133]. Remarkably, for $\theta \approx 1$, the extent of intermittent dynamics of the system is maximized (as measured by the switching intensity, I). Fig. 4.10 displays two separate heatmaps of switching intensity. Both for constant values of $\gamma = 0.2$ (Fig. 4.10a) and $c_v = 6\%$ (Fig. 4.10b), the intermittent switching is maximized along contours of constant $\theta \approx 1$, as shown by the white dashed lines. For larger values of θ, the system would be in a "turbulent" state, whereas for lower values of θ, the system will remain laminar. Another feature worth highlighting is that for very low c_v (ϕ), no matter how large ϕ (c_v) is, the system will remain stable, drawing close

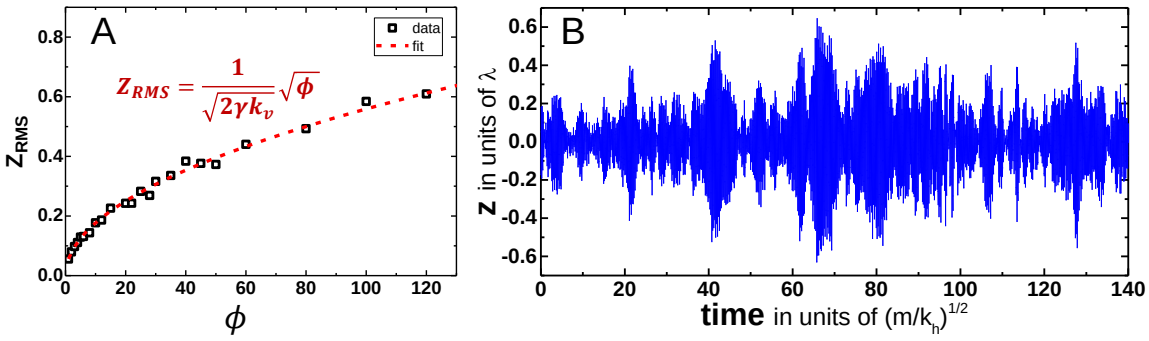

Figure 4.11: (A) Root Mean Square (RMS) of the oscillation amplitude in z of a single particle as a function of ϕ, $\gamma = 0.2$ and $k_v = 800$. The dashed red line is the analytic prediction for a damped, stochastically-driven harmonic oscillator. (B) z-position of a single particle in a sample of 500 particles that is forced at $\phi = 18$. The system melts at time = 70 due to the large preceding oscillation amplitude.

similarities with linear stability of the fluid flow in a pipe, where for the turbulence to develop both driving and wall roughness need to be large enough.

4.6 Summary

The numerical simulations allowed us to elucidate the major components of the system and their coupling mechanism that gives rise to emergent intermittent dynamics. Similar to conventional turbulence, in our system, the intermittent switching arises due to the coupling of external driving and structural heterogeneities. However, there are subtle differences between our model and conventional pipe flow. If the structural inhomogeneities for the fluid flow in a pipe is due to external factors, such as roughness of the pipe walls, in our system defects emerge due to internal features, such as distribution of particles sizes (masses). Furthermore, if the external driving in the pipe flow is due to *constant* pressure drop, in our system input of energy is noisy. More specifically, we utilized so-called "white noise" to induce the vertical oscillations in the system. There were several reasons for utilizing noisy driving in our numerical simulations. Firstly, we were not aware of the exact nature

of forcing in the experiments, and we took into account that the vast majority of complex systems are subject to environmental fluctuations and with the intention of not losing the generality, we used Gaussian noise to force the system. Secondly, there has been substantial evidence that describing the turbulent flow via "renormalized viscosity" and a fluctuating "renormalized forcing" framework yields experimentally viable results [134].

It is worth mentioning a few words about the noise-induced dynamics in complex systems. Noise is commonly regarded as an unavoidable inconvenience due to an ever-changing environment and a nuisance that interferes with otherwise deterministic processes. However, noise has been found to play a crucial role in various dynamical systems. For example, noise can facilitate switching between two or more distinct states in non-equilibrium systems. Dynamics that benefit from, rather than become hindered by noise are usually discussed through the framework of stochastic resonance[135]. Originally developed to explain cycles of planetary climate[136], stochastic resonance has been experimentally observed in various physical [137–139] and neurophysiological systems [140, 141]. Furthermore, noise has been found to induce spatio-temporal regularity in non-linear systems, where environmental fluctuations can result into regular spatial structure. Noise, both environmental and demographic, has been found to alter the behavior of ecological systems, where stochastic effects, such as demographic noise, can induce oscillations [142, 143] and even enable coexistence between distinct species [144, 145]. The evidence for noise not being just a defacement to deterministic processes is rather overwhelming, and presumably a paradigmatic shift towards treating noise as a creator of various nonlinear phenomena and an "informer" of underlying dynamics in complex systems is imminent [146].

For our numerical simulations, not necessarily the experiments, the noisy driving is essential. If the particles were driven periodically, their response would have a peak at the frequency of periodic external driving, preventing a growth of phase between oscillations of the particles. Once the particles are driven with white noise, the maximum of their response inversely depends on their masses. Consequently, particles forming a polydisperse system oscillate at differing frequencies, making scattering in the vertical direction and consequent melting of the system inevitable.

Furthermore, we found that the equilibrium properties, namely the polarization of the vibrational normal modes in the vertical direction, can predict the non-equilibrium response of the system. The localized vertical modes get easily excited by noisy external driving and they transfer energy to orthogonal modes, resulting into melting of the crystal and transition to "turbulent" states. Characterizing similar relationships between structural properties and the ensuing dynamics is a challenging task in fluid flows. This demonstrates a great advantage of our system as a physical model to study spatio-temporal intermittent dynamics on a constituent-scale.

Chapter 5

Minimal Model for Energy Evolution

5.1 "Ecological" Interactions in Complex Systems

An ecosystem of two or more competing species is an archetypal model for studying emergent oscillations in complex systems. The simplest case, comprised of two species - predator and prey, is called the Lotka-Volterra model [147, 148]. Qualitatively, the system behaves in the following manner: prey numbers increase, resulting in predators eating more prey, consequently increasing the number of predators. Under increased predation, the number of prey decreases, resulting in a subsequent decrease in predators as well. Under reduced predation, the number of prey increases and the cycle goes on. In deterministic predator-prey models, the characteristic phase between prey and predator is $\pi/2$, which is sustained until the equilibrium point is reached in the phase space. Other timescales have been found to emerge in predator-prey systems under stochastic conditions, where random birth and death rates, so-called demographic stochasticity, can result in intermittent fluctuations of the species' numbers.

The predator and prey for our system would be horizontal and vertical energies, respectively. The vertical energy increases gradually to a certain point and then gets "consumed" by horizontal energy. In more accurate terms, the energy gets

redistributed isotropically due to a scattering event. Transfer of energy from vertical to horizontal degrees of freedom represents an underlying mechanism of the emergent intermittent switching. The energy is pumped in the vertical direction due to the spontaneous oscillations and then energy gets redistributed to the horizontal degrees of freedom due to scattering events. We use the model of Rutherford scattering to estimate the rate of energy exchange between particles during the scattering events.

5.2 Derivation of Coupling between Vertical and Horizontal Energies

In this system, particles are strongly confined in the vertical direction, and weakly confined in the horizontal directions, leading to a quasi-2D geometry. Energy is only delivered to the vertical direction due to white noise and is redistributed to the horizontal degrees of freedom due to nonlinear interactions between particles. These nonlinearities occur when neighboring particles oscillate out-of-phase at high amplitude and their horizontal separation is small enough for them to scatter classically. We used the model of Rutherford scattering to estimate the rate of energy exchange between vertical and horizontal degrees of freedom during collisions.

Suppose two particles interact with a pairwise, repulsive, isotropic potential, $U(r)$. We consider elastic scattering with impact parameter b and initial kinetic energy E_0 (Fig. 5.1). The linear momentum, angular momentum, and total mechanical energy are conserved. Let $v_r(t) = \frac{dr}{dt}$ and $v_\theta(t) = r\frac{d\theta}{dt}$ denote the radial and tangential velocity in the center-of-mass frame, respectively, and m is the mass of each identical particle. Conservation of angular momentum and energy yields:

$$v_\theta(t) = \frac{J}{mr(t)} \tag{5.1}$$

$$v_r(t) = \sqrt{\frac{2}{m}\left(E_0 - U(r(t)) - \frac{mv_\theta(t)^2}{2}\right)}, \tag{5.2}$$

where $J = b\sqrt{2mE_0}$ is the angular momentum, and we have only considered the

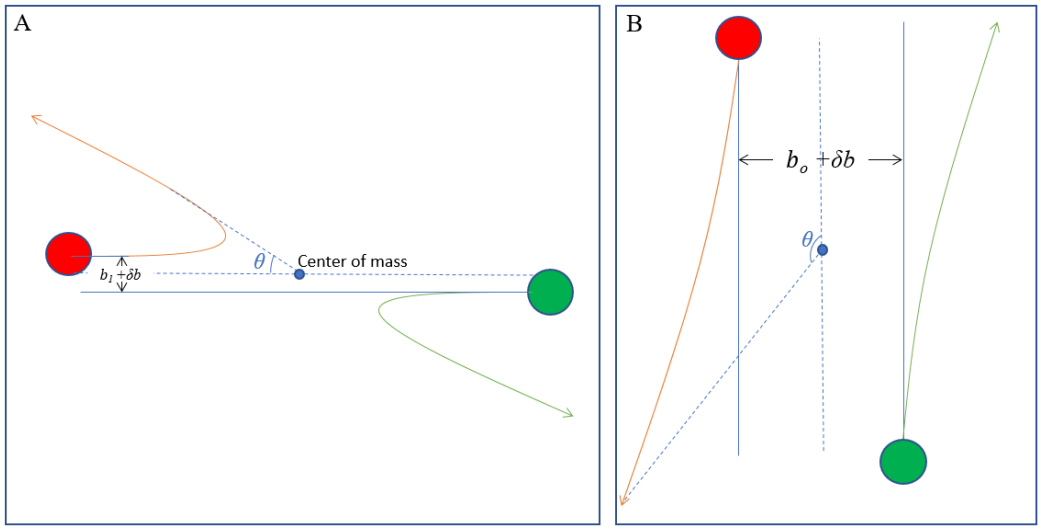

Figure 5.1: The sketch of scattering process taking place in the center-of-mass frame. Two limiting cases correspond to when all the energy is in (a) the horizontal direction and (b) the vertical direction.

outgoing part of the scattering where $v_r > 0$. Dividing equation 5.1 by 5.2 yields

$$\frac{v_\theta(t)}{v_r(t)} = \frac{J}{r(t)\sqrt{2m(E_0 - U(r(t)) - \frac{mv_\theta(t)^2}{2})}}. \tag{5.3}$$

The left side of the equation also equals $\frac{1}{r}\frac{d\theta}{dt}\frac{dt}{dr}$. Cancelling out dt and substituting for v_θ and J results in:

$$\frac{d\theta}{dr} = \frac{b}{r\sqrt{r^2 - b^2 - r^2\frac{U(r)}{E_0}}}. \tag{5.4}$$

The particles come from infinitely far away prior to interacting. The closest distance to the center of mass that the particles can reach is r_{min}, which is the positive solution for

$$r^2 - b^2 - r^2\frac{U(r)}{E_0} = 0. \tag{5.5}$$

Assuming the incoming angle is $\theta(t = -\infty) = \pi$, then we add a negative sign since J is negative, and at the closest approach (r_{min}), $\theta = \pi/2 + \theta_f/2$, where $\theta_f = \theta(t = \infty)$. Thus

$$\theta_f = \pi - 2\int_{r_{min}}^{\infty} \frac{b}{r\sqrt{r^2 - b^2 - r^2\frac{U(r)}{E_0}}} dr. \tag{5.6}$$

If we assume a Coulomb potential of the form $U = aE_0/r$, where a is a characteristic interaction radius, then we may evaluate the integral, noting that the denominator is zero when $r = r_{min}$ (although the integral does not diverge):

$$\theta_f = \pi - 2\arctan\left(\frac{2b}{a}\right). \tag{5.7}$$

Ultimately we want the amount of kinetic energy transferred to perpendicular direction, which is:

$$E_0 \sin^2\theta_f = 16E_0\frac{a^2b^2}{(a^2+4b^2)^2}. \tag{5.8}$$

Here we have assumed a long-ranged Coulomb potential. However, our simulations use a finite-ranged, screened potential. In the case of hard spheres of radius R, the scattering formula is nearly the same as in Eq. 5.8, except that a is replaced with $4R$.

The potential energies associated with the external confinement of particles are independent, i.e. they depend only on r or z. As a result, mechanical energy can be divided into vertical and horizontal energy. In each direction, kinetic and potential energy is assumed to be equipartitioned. Since the particles strongly confined in z, collisions are mostly determined by kinetics within the xy-plane. The frequency of collision between particles, f_c, is:

$$f_c = v_h a\rho, \tag{5.9}$$

where ρ is the surface density of the particles, a is the typical spacing, and v_h is the average horizontal velocity. As the energy is mainly in the horizontal direction, the vertical energy E_v can be expressed as

$$E_v = k_v\delta b^2 = mv_v^2, \tag{5.10}$$

where k_v is the strength of vertical confinement, v_v is the average vertical velocity, m is the particle mass, and δb is average vertical displacement from equilibrium position. Since particles can have different masses, on average there is a gap between the vertical equilibrium position of each particle, denoted as b_1, which is dependent on c_v. $b_1 + \delta b$ gives the impact parameter of one collision (see Fig. 5.1A). After each

collision, a portion of kinetic energy ΔE is transferred from the horizontal to the vertical direction:

$$\Delta E_v(\delta b) = \frac{E_h \sin^2 \theta_f}{2} \approx \frac{8a^2 E_h (b_1 + \delta b)^2}{\left(a^2 + 4(b_1 + \delta b)^2\right)^2}. \tag{5.11}$$

We are only interested in the amount of energy transferred due to the excess vertical displacements, δb. Therefore, the net energy transferred is:

$$|\Delta E_v(\delta b) - \Delta E_v(0)| \approx \frac{16a^2 b_1 E_h \left(a^2 - 4b_1^2\right)}{\left(a^2 + 4b_1^2\right)^3} \delta b. \tag{5.12}$$

The total rate of energy transfer from the horizontal to vertical direction, $p_{h\to v}$, is proportional to the above quantity multiplied by the collision frequency (Eq. 5.9). Since $v_h \propto E_h^{1/2}$ and $\delta b \propto E_v^{1/2}$ (Eq. 5.10), the power of energy transfer is

$$p_{h\to v} \propto E_h^{\frac{3}{2}} E_v^{\frac{1}{2}}. \tag{5.13}$$

5.2.1 Case 2: Energy is mostly in vertical degrees of freedom

This case is more important for the recurrent energy cascades since the energy is constantly driven into the vertical direction, leading to vertical oscillations, with subsequent scattering events that transfer energy to the horizontal direction. Figure 5.1B illustrates this case. The derivation here is identical to Case 1, except the role of vertical and horizontal energies are reversed. However, the collision rate is still dependent on the horizontal energy since the particles are strongly confined in z.

Thus, we have:

$$p_{v\to h} \propto v_h v_v^2 \delta b \propto E_h E_v \tag{5.14}$$

since $\delta b \propto E_h^{1/2}$. Thus, the fundamental asymmetry in the two cases comes from the fact that the collision rate only depends on the average horizontal velocities.

5.2.2 Application to minimal model

For simplicity, we combine these two terms and assume that both types of scattering events can occur simultaneously. This model gives the result that the net power

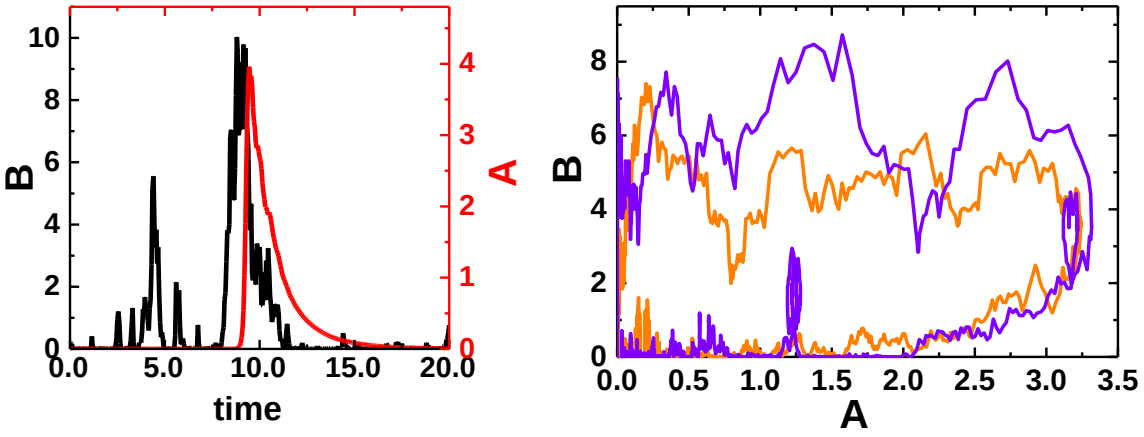

Figure 5.2: (Left) Temporal evolution of A and B over 20 units in time with $c = 1.5$, $\Phi = 10$, and $\gamma = 0.5$. (Right) Phase portrait of two separate cascades in energy for the same parameters.

of energy transferred from vertical to horizontal is:

$$p_{v\to h,net} \approx c_1(E_v E_h)(1 - c_2\sqrt{\frac{E_h}{E_v}}), \tag{5.15}$$

where c_1, c_2 are constants independent of energy. In our minimal model, we assume $c_1 = c$ and $c_2 = 1$ for simplicity. Consequently, if $E_v = E_h$, no net energy is transferred between the degrees of freedom.

As mentioned, both in experiment and simulation, Case 2 is the most common, and Case 1 is only important in the gas-like state. In fact, the quantity b_1 is very small or zero in most cases, i.e. if there is no vertical energy, the particles rest in the same plane. Nevertheless, we have kept terms linear in δb for simplicity and symmetry. Although this is only a rudimentary model, assuming Coulomb interaction, it captures the appropriate scaling of E_v and E_h, and is based on physical processes and kinetics in the experiment and particle simulation.

5.3 Modelling "Ecological" Interactions Between Mechanical Energies

The next step is to determine the "death" rates of the species. We have assumed that kinetic and potential energies are equipartitioned in each direction, so that $A = 2\langle KE_{xy}\rangle$ and $B = 2\langle KE_z\rangle$. The amount of power one particle dissipates to the environment would be equal to the product of the damping force and its velocity. Thus

$$\frac{dKE}{dt} = \sum \vec{\mathbf{F}}_d \cdot \vec{\mathbf{v}} = -\sum \gamma m(v_x^2 + v_y^2 + v_z^2) = -\gamma(KE), \tag{5.16}$$

where KE is the total kinetic energy of the system, $\vec{\mathbf{F}}_d$ is the damping force and $\vec{\mathbf{v}}$ is the particle velocity and the sum runs over each particle.

Next, we characterize the "birth" rates. It is a common practice in the predator-prey literature to study systems where only one, usually the prey population, experiences so-called demographic stochasticity (noise). This is further justified for our system, as it is the vertical mechanical energy that experiences constant input.

Therefore, in our many-body system, we derive a two-species framework by considering the total horizontal mechanical energy (A) as a predator, and the total vertical mechanical energy (B) as a prey to be consumed:

$$\frac{dA}{dt} = -\gamma A + cAB\left(1 - \sqrt{A/B}\right), \tag{5.17}$$

$$\frac{dB}{dt} = -\gamma B - cAB\left(1 - \sqrt{A/B}\right) + w(t)\sqrt{B\Phi/\Delta t}. \tag{5.18}$$

The second term, as derived above from classical scattering theory, characterizes "predation" between mechanical energies and obeys energy conservation. The constant c controls the coupling between vertical and horizontal energies, and parameterizes the polydispersity in the many-body system. Finally, the third term in Eq. 5.18 represents the instantaneous power delivered in the vertical direction, $\vec{\mathbf{F}}_s \cdot v_z\hat{\mathbf{z}}$, where $v_z \sim \sqrt{B/m}$ and Φ is the average power. Similar noise terms are commonly used to model demographic stochasticity in ecological systems, often resulting in population oscillations [149].

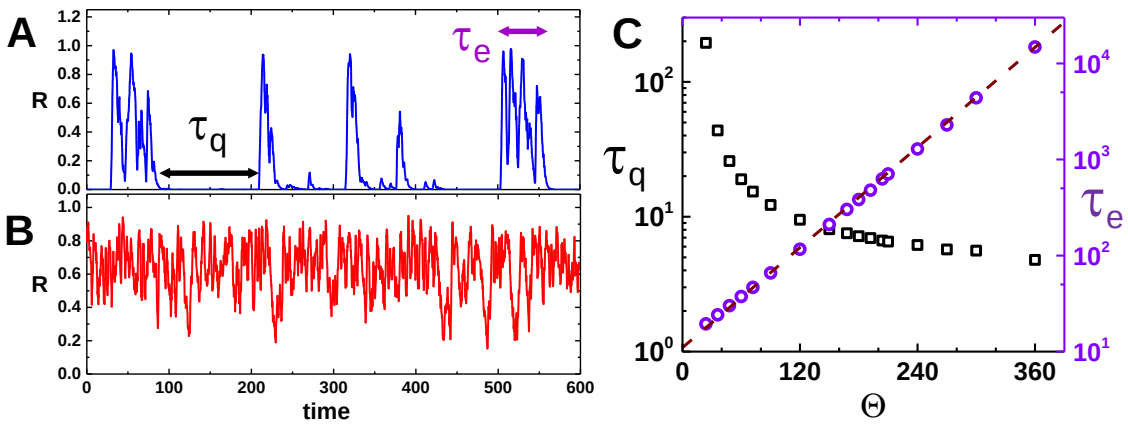

Figure 5.3: Temporal evolution of fractional horizontal mechanical energy, R exhibits intermittent switching (A) for $c = 1$ and $\Phi = 8$ and perpetually melted state (B) for $c = 4$ and $\Phi = 20$, $\gamma = 0.5$ in both cases. (C) The mean duration of quiescent (τ_q) and excited (τ_e) states for varying Φ (with $\gamma = 0.5$ and $c = 1.5$). The states are separated using threshold algorithm on the quantity A.

These equations recreate the three observed dynamical regimes. To directly compare with the numerical simulations, we define $R \equiv A/(A + B)$ as the fractional horizontal mechanical energy, in analogy with Δ_{xy} (Fig. 4.1B). For intermediate values of c and Φ, R exhibits intermittent behavior (Fig. 5.3A), whereas sufficiently increasing either parameter results in a perpetually excited, equipartitioned state ($A \sim B$) (Fig. 5.3B). The dependence of the switching intensity on both parameters can be seen in Fig. 5.4. The heatmap shows that there is a distinct region where intermittent dynamics can be observed.

Before getting into details of these coupled equations,it is worthwhile to briefly mention some general characteristics of predator-prey systems. Classical, deterministic Lotka-Voltera systems usually exhibit cycles with decaying amplitude, but never intermittent fluctuations. Intermittent dynamics usually emerges once a third type of species is introduced to the system. If one introduces an additional prey or predator species or even just a resource as a separate species, the dynamics become chaotic with characteristic intermittent spiking in the number of species. For example, Vance [150] demonstrated that a Predator-Two-Prey model exhibits chaotic dynamics, as iden-

tified by "quasi-cyclic" fluctuations in relative numbers of predator and two preys. Gilpin [151] generalized these findings to a higher number of interacting prey and predator species and found that the quasi-cyclic nature of dynamics is due to a "spiral attractor", also known as a teacup attractor. This framework closely resembles, as one would have expected, Ed Lorenz's seminal work in chaos theory [152], where he showed that the three coupled variables, describing different variables of atmospheric flow, exhibit sensitive dependence on the initial conditions and nonperiodic oscillations. A three-species framework has also been successfully applied to understand chaotic dynamics in food-web systems [153], intermittent precipitation in aerosol-cloud-rain climate models [154] and the recurrence of turbulent "puffs" in transitional pipe flow [26].

In our system, we only have two species. The role of the third species is assumed by the demographic noise, the third term in 5.18. If one disregarded that term, intermittent fluctuations would disappear and the system would smoothly decay from some initial condition to eventual, complete extinction. This is easily seen if one adds up 5.17 and 5.18 and inspects the resulting equation -

$$\frac{d(A+B)}{dt} = -\gamma(A+B), \tag{5.19}$$

where the cumulative number of predator and prey species $(A+B)$ decays to zero at rate γ without any fluctuations.

The role of stochastic noise in the emergent dynamics of ecological systems has been actively studied in the last 50 years. Demographic stochasticity, representing the random nature of birth and death events, has been found to induce quasi-cycles [142, 143] and even switching dynamics [155]. In a similar vein, the environmental noise can enable coexistence of competing species [156] and in other cases, can drive the species to extinction [157]. Thus, after including the demographic noise for "prey" populations, the cycling behavior was somewhat anticipated.

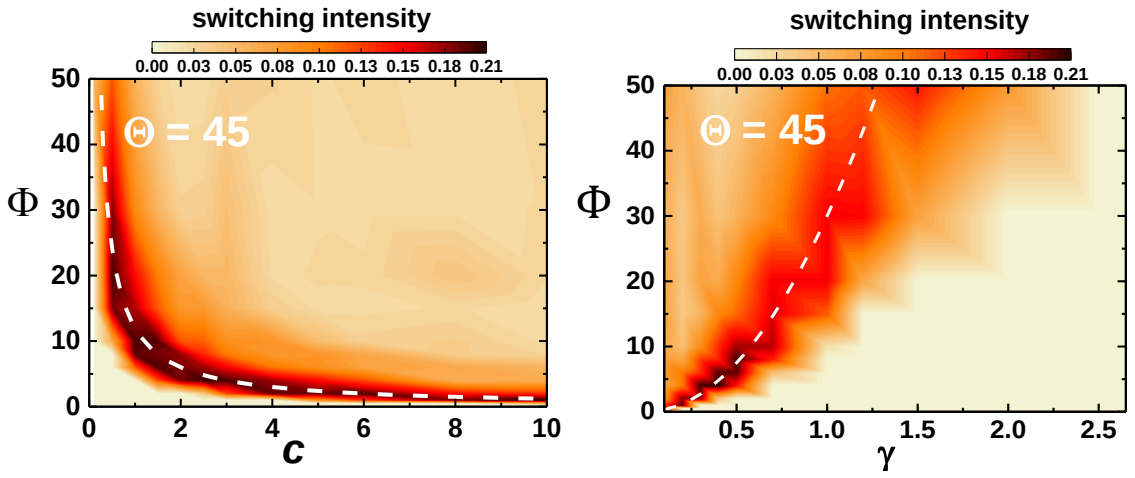

Figure 5.4: (Left) Switching intensity of R for constant $\gamma = 0.5$ and a range of Φ and c. (Right) Switching intensity of R for constant c = 1.5 and a range of Φ and γ.

5.3.1 Dimensionless Number

In a similar manner to the particle-based simulations, the dynamics in our minimal model can be described by a single dimensionless number,

$$\Theta = c\Phi/\gamma^2, \tag{5.20}$$

where the numerator signifies the collective effect of disorder (c) and driving (Φ) and the denominator is a dissipation term. Intermittent dynamics are only observed for $20 \lesssim \Theta \lesssim 120$ (Fig. 5.4), in analogy to transitional pipe flow, where intermittent turbulence is observed for intermediate Reynolds numbers ($1700 \lesssim \mathrm{Re} \lesssim 2300$) [158].

5.3.2 Critical Dynamics and Lifetime Statistics in the Minimal Model

As mentioned above, there have been continuous attempts to find links between intermittent turbulence and thermodynamic theories pertaining to critical phase transitions. Schertzer et al. showed that intermittency in turbulent flows can be ascribed to the collective effect of "renormalized viscosity" and "renormalized forcing" [134].

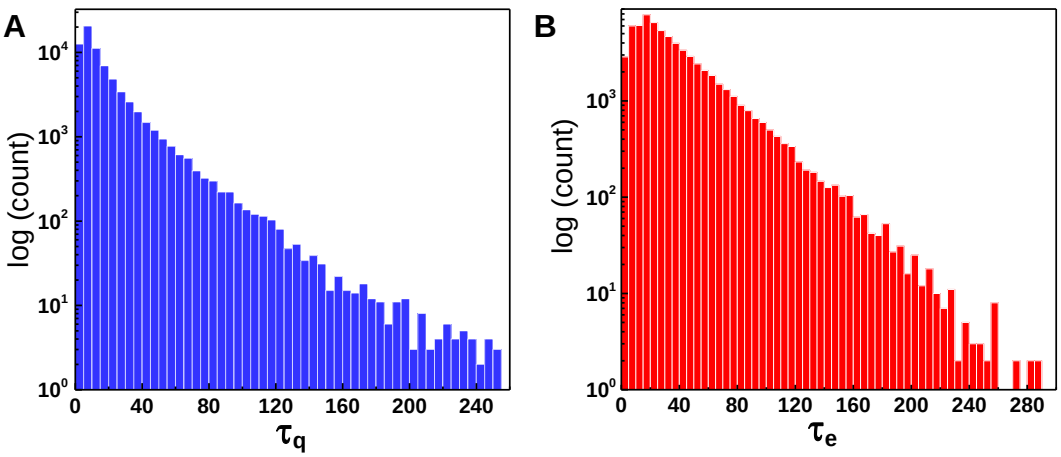

Figure 5.5: Distributions of durations of quiescent (τ_q) and excited (τ_e) states for $\Theta = 48$. Both τ_q and τ_e follow exponential distribution for large time scales.

Other works have found [159] a close connection between intermittent turbulence and self-organized criticality [132, 133], an iconic model to study "avalanche" dynamics in driven media.

Over the last 30 years, the connection between the intermittent turbulence and directed percolation (DP) has become gradually clearer [25, 26, 160–162]. More precisely, intermittent turbulent flow in a pipe is in the same universality class as DP. The analogy becomes a lot more evident, if one pictures turbulent puffs as excited states and laminar flow as absorbing state. Relating intermittent turbulence to DP became possible by investigating the statistical features of the temporal behavior. Namely, for intermittent turbulence with spatially-separated, coexisting, independent "puffs", the lifetime of the turbulent state were found to scale super-exponentially with Reynolds number [9, 26].

The excited (turbulent) and quiescent (laminar) states in our minimal model are separated using a threshold algorithm. Throughout an entire time series, we define the excited state as times when $A/\langle B\rangle > 0.02$, where $\langle B\rangle$ represents the average over the entire time series. After the initial threshold, some excited (quiescent) periods are very short. Quiescent periods that are shorter than 3 time units are identified

and removed while the two neighboring excited periods are concatenated. The remaining short excited periods which are less than 3 time unites are not counted in the distributions. An example of distributions for quiescent and excited periods with $\Theta = 48$ are presented in Fig. 5.4. The entire time series is 10^6 time units. For a given Θ in our minimal model, the probability distribution of both excited (τ_e) and quiescent (τ_q) state lifetimes have exponential tails Fig.5.5, and the mean lifetime of the excited state scales exponentially with Θ (Fig. 5.3C). This scaling originates from the memory-less noise driving the system. If our many-body system took spatial parameters into considerations and could support multiple excited, gas-like regions simultaneously, we would expect extreme value statistics and subsequently, super-exponential behavior [162].

Chapter 6

Summary

The vast majority of natural complex phenomena resist reductionist explanations. There is no single formula that can predict the duration and extent of the next draught, ice age, epidemic outbreak, or financial crash. The path of understanding the behavior of climate, epidemic outbreaks, financial crashes, social networks and fluid flows is hindered by a large number of degrees of freedom. Since emergent behaviors are due to the collective effects of a huge number of constituent elements, our minds and scientific tools fall short in relating the local interactions between the elements to the emergent spatio-temporal, global behavior. Both experimentally and conceptually, a solution that would allow one to scratch the surface of this seemingly impossible task lies in model systems, which would not have all *all* the features of the real system, but the essential ones to manifest emergent behavior.

Our experimental discovery, and subsequent numerical and theoretical work, can serve as a model system for a well-known classical physics phenomenon - transitional turbulence in wall-bounded geometries. The coherent laminar fluid flow, upon increasing the flow velocity, will start exhibiting transient patches of turbulence that travel downstream in the pipe and eventually decay back into laminar flow. The non-trivial nature of the "puffs" lies in the statistical distribution of their spatial and temporal sizes - some get to expand throughout the whole system and some stay the same size for most of their journey before they become laminar again. We discovered that a crystalline layer made out of microscopic charged particles, upon

coherent oscillation in the vertical direction, experiences intermittent switching to a melted, gas-like phase, which persists for some amount of time before the system re-crystallizes into a "laminar" state. The switching persists for hours. Similar to the transition to turbulence, spatio-temporal intermittent dynamics emerge in our system due to coupling between *external driving* and *structural imperfections*. In fluid flow, both driving and inhomogeneities are due to external factors - a pressure drop or shear is usually applied by an external agent and structural imperfections are due to wall roughness. In dusty plasma systems, driving is due to the spontaneous vertical oscillations, the mechanism and results of which can be found in Chapter 3. Furthermore, the structural heterogeneities in dusty plasma crystals arise due to the inherent distribution of particle sizes. The coupling mechanism between structural imperfections and external driving is investigated using molecular dynamics simulations and the results are presented in Chapter 4.

We utilized normal mode analysis and found that quenched disorder, arising from the distribution of particle sizes, gives rises to localized vibrational modes that are polarized in the vertical direction. We found that intermittent dynamics is maximized for some intermediate fraction of the localized modes. These modes become excited even for low intensities of external driving and transfer energy to orthonormal modes, resulting in a transition to a melted state. This way we are able to quantify the non-equilibrium response of the system by measuring it's equilibrium properties. Defining similar relations in most other complex systems is an impossible task, as most complex systems are not strongly-coupled, preventing any characterization or even conceptualization of equilibrium properties.

Our simulations also reveal that intermittent dynamics can be manifested under stochastic forcing. This is not necessarily a surprising result as similar behavior is omnipresent in ecological systems, however, it highlights the potential of applying the the framework of our model system to more complicated, complex systems. Another vital insight provided by the numerical simulations is that the melting transition is governed by the scattering event, which can be measured by calculating the minimal horizontal distance between any two particles in the system.

Once we observe that the scattering event is necessary for the melting to occur,

we show how energies in orthogonal directions exchange due to scattering events. If one models the vertical and horizontal mechanical energies as interacting species, the conventional predation term ends can be derived using scattering theory. Furthermore, we calculate the "death terms" as dissipated powers and find that death terms are linear functions of the number of species. Finally, the demographic noise term sustains the prey population (vertical mechanical energy). The resulting system of equations recreates the intermittent switching dynamics observed in the experiments and simulations.

Altogether, the experiment, simulation, and theoretical model represent an example of how highly non-linear phenomena can emerge in simple laboratory systems. The simple, lab-based system can then come to characterize the essential ingredients of emergence in complex systems.

Appendix A

Appendix A

This appendix contains Fortran codes for the molecular dynamics simulation for electrostatic case and a simplified scenario.

A.1 Code for Electrostatic Simulation

```
PROGRAM Dynamics DUSTY TOY MODEL

      DOUBLE PRECISION PI,E
      INTEGER BNN

      PARAMETER (BNN=500)
      PARAMETER (PI=3.14159265358979323846264 3D0)
      PARAMETER (E=2.71828182845904523536028 74D0)
C
      DOUBLEPRECISION, ALLOCATABLE, DIMENSION(:) :: R,M,Q
      DOUBLEPRECISION, ALLOCATABLE, DIMENSION(:,:) :: DELTAX,X,A,V,XOLD
      INTEGER, ALLOCATABLE, DIMENSION(:,:) :: IJARRAY

      DOUBLE PRECISION TOTALTIME,DELTAT
      DOUBLE PRECISION TEMPDIST
      DOUBLE PRECISION VNORM,VOLT,VEF,CHIV,CHIH
      DOUBLE PRECISION TEMPGSUM,TEMPVEC(3),BETA,MAXTIME,FF,FA
      DOUBLE PRECISION SKN,FD,RAND1,RAND2,KEZ,KEXY,POTZ,POTR,POTI,DQ
      DOUBLE PRECISION TTERM,ALPHA,GAMMA,EPSILON,DEN,GRAV,LAMBDA,QT
      INTEGER ENDER
      INTEGER J,I,K,NPAR,STEPS,NEWPOS,WPOS
```

```
      INTEGER WRITER,WFREQ

      OPEN(800,FILE="tempin.dat",STATUS="OLD",ACTION="READ",
     *FORM="UNFORMATTED",ACCESS="STREAM")

      OPEN(801,FILE="dusty_positions.dat",STATUS="REPLACE",
     *ACTION="WRITE",FORM="UNFORMATTED",ACCESS="STREAM")
      CLOSE(801)

      OPEN(801,FILE="dusty_positions.dat",STATUS="OLD",ACTION="WRITE",
     *FORM="UNFORMATTED",ACCESS="STREAM",POSITION="APPEND")

      OPEN(802,FILE="dusty_energy.dat",STATUS="REPLACE",ACTION="WRITE",
     *FORM="UNFORMATTED",ACCESS="STREAM")
      CLOSE(802)

      OPEN(802,FILE="dusty_energy.dat",STATUS="OLD",ACTION="WRITE",
     *FORM="UNFORMATTED",ACCESS="STREAM",POSITION="APPEND")

      READ(800,END=9) NPAR,WFREQ,WPOS

      ALLOCATE(X(3,NPAR),A(3,NPAR),R(NPAR),V(3,NPAR),XOLD(3,NPAR))
      ALLOCATE(DELTAX(3,NPAR),M(NPAR),Q(NPAR))
      ALLOCATE(IJARRAY(2,BNN*NPAR))

      READ(800,END=9) DELTAT,LAMBDA,VOLT,VEF,CHIV,CHIH,GAMMA,FD,FA,FF
      READ(800,END=9) MAXTIME,(R(I),I=1,NPAR),((X(J,I),J=1,3),I=1,NPAR)

9     CONTINUE

      CLOSE(800)

      TOTALTIME=0D0
      STEPS=0
      WRITER=1
      DEN=1510.0
      GRAV=9.81
      EPSILON=8.85D-12

10    CONTINUE

      SKN=0.5*3*LAMBDA
```

```
      DO I=1,NPAR
         M(I)=4*PI*DEN*R(I)**3/3
         Q(I)=4*EPSILON*PI*R(I)*VOLT
      ENDDO

      A=0D0
      V=0D0

C     Contruct Neighbor Lists
13    CONTINUE

      A=0D0
      XOLD=X
      POTI=0D0
      POTR=0D0
      POTZ=0D0

      NEWPOS=1
      DO I=2,NPAR
         DO J=1,I-1
            TEMPVEC(:)=X(:,I)-X(:,J)
            TEMPDIST=DSQRT(TEMPVEC(1)*TEMPVEC(1)+TEMPVEC(2)*
     *      TEMPVEC(2)+TEMPVEC(3)*TEMPVEC(3))
            IF(TEMPDIST.GT.(SKN+3*LAMBDA)) CYCLE
            IJARRAY(1,NEWPOS)=I
            IJARRAY(2,NEWPOS)=J
            NEWPOS=NEWPOS+1
            IF(TEMPDIST.LT.(3*LAMBDA)) THEN
             POTI=POTI+(4*EPSILON*PI*R(I)*R(J)*(9/(E**(TEMPDIST/LAMBDA)
     *       *TEMPDIST)+(-15*LAMBDA+4*TEMPDIST)/(E**3*LAMBDA**2))*
     *       VOLT**2)/9
               TEMPGSUM=(4*E**(-3-TEMPDIST/LAMBDA)*EPSILON*PI*R(I)*R(J)
     *       *(4*E**(TEMPDIST/LAMBDA)*TEMPDIST**2-9*E**3*LAMBDA*(LAMBDA
     *       +TEMPDIST))*VOLT**2)/(9*LAMBDA**2*TEMPDIST**3)
               A(:,I)=A(:,I)-(TEMPVEC(:)*TEMPGSUM)/M(I)
               A(:,J)=A(:,J)+TEMPVEC(:)*TEMPGSUM/M(J)
            ENDIF
         ENDDO
      ENDDO

      CALL RANDOM_NUMBER(RAND1)
      CALL RANDOM_NUMBER(RAND2)
```

```
      RAND1=DSQRT(-2*DLOG(1-RAND1))*COS(2*PI*RAND2)
      DO I=1,NPAR
         QT=Q(I)
         POTR=POTR+0.5*CHIH*QT*(X(1,I)**2+X(2,I)**2)
         POTZ=POTZ-(VEF*X(3,I)-0.5*CHIV*X(3,I)**2)*QT+GRAV*M(I)*X(3,I)
         A(1,I)=A(1,I)-CHIH*QT*X(1,I)/M(I)
         A(2,I)=A(2,I)-CHIH*QT*X(2,I)/M(I)
         A(3,I)=A(3,I)-GRAV+(VEF-CHIV*X(3,I))*QT/M(I)+
     *   RAND1*(FD+FA*SIN(2*PI*FF*TOTALTIME))/M(I)
         A(:,I)=A(:,I)-GAMMA*V(:,I)
      ENDDO

C     END construct neighbor list

C      IF(MOD(STEPS-1,50).EQ.0) WRITE(*,700) MAXVAL(ABS(DELTAX))

      IF(WRITER.EQ.0) THEN
         WRITER=1
         GOTO 70
      ENDIF

58    CONTINUE

      IF((MOD(STEPS,WFREQ).EQ.0).AND.(WPOS.EQ.1)) THEN
         WRITE(801) ((X(J,I),J=1,3),I=1,NPAR)
      ENDIF

      IF(MOD(STEPS,WFREQ).EQ.0) THEN
         KEXY=0D0
         KEZ=0D0
         DO I=1,NPAR
            KEXY=KEXY+0.5*M(I)*(V(1,I)**2+V(2,I)**2)
            KEZ=KEZ+0.5*M(I)*(V(3,I)**2)
         ENDDO
         WRITE(802) TOTALTIME,KEXY/NPAR,KEZ/NPAR,POTZ/NPAR,
     *   POTR/NPAR,POTZ/NPAR
      ENDIF

      X=X+DELTAT*V+(5D-1)*A*DELTAT**2
      V=V+A*DELTAT*5D-1
      DELTAX=ABS(X-XOLD)
```

```
      IF((MAXVAL(DELTAX).GE.(SKN/2D0)).OR.(MOD(STEPS+1,1000).EQ.0)) THEN
         WRITER=0
         GOTO 13
      ENDIF

      A=0D0
      POTI=0D0
      POTR=0D0
      POTZ=0D0

      DO K=1,NEWPOS-1
         I=IJARRAY(1,K)
         J=IJARRAY(2,K)
         TEMPVEC(:)=X(:,I)-X(:,J)
         TEMPDIST=DSQRT(TEMPVEC(1)*TEMPVEC(1)+TEMPVEC(2)*
     *   TEMPVEC(2)+TEMPVEC(3)*TEMPVEC(3))
         IF(TEMPDIST.GT.(3*LAMBDA)) CYCLE
           POTI=POTI+(4*EPSILON*PI*R(I)*R(J)*(9/(E**(TEMPDIST/LAMBDA)
     *       *TEMPDIST)+(-15*LAMBDA+4*TEMPDIST)/(E**3*LAMBDA**2))*
     *       VOLT**2)/9
          TEMPGSUM=(4*E**(-3-TEMPDIST/LAMBDA)*EPSILON*PI*R(I)*R(J)
     *       *(4*E**(TEMPDIST/LAMBDA)*TEMPDIST**2-9*E**3*LAMBDA*(LAMBDA
     *       +TEMPDIST))*VOLT**2)/(9*LAMBDA**2*TEMPDIST**3)
         A(:,I)=A(:,I)-(TEMPVEC(:)*TEMPGSUM)/M(I)
         A(:,J)=A(:,J)+TEMPVEC(:)*TEMPGSUM/M(J)
      ENDDO

      CALL RANDOM_NUMBER(RAND1)
      CALL RANDOM_NUMBER(RAND2)
      RAND1=DSQRT(-2*DLOG(1-RAND1))*COS(2*PI*RAND2)
      DO I=1,NPAR
         QT=Q(I)
         POTR=POTR+0.5*CHIH*QT*(X(1,I)**2+X(2,I)**2)
         POTZ=POTZ-(VEF*X(3,I)-0.5*CHIV*X(3,I)**2)*QT+GRAV*M(I)*X(3,I)
         A(1,I)=A(1,I)-CHIH*QT*X(1,I)/M(I)
         A(2,I)=A(2,I)-CHIH*QT*X(2,I)/M(I)
         A(3,I)=A(3,I)-GRAV+(VEF-CHIV*X(3,I))*QT/M(I)+
     *   RAND1*(FD+FA*SIN(2*PI*FF*TOTALTIME))/M(I)
         A(:,I)=A(:,I)-GAMMA*V(:,I)
      ENDDO

70    CONTINUE
```

```
      V=V+A*DELTAT*5D-1

      STEPS=STEPS+1
      TOTALTIME=STEPS*DELTAT

C      IF(STEPS.GT.200) GOTO 100

      IF(TOTALTIME.GT.MAXTIME) GOTO 100

      IF(MOD(STEPS,WFREQ*500).EQ.0) THEN
         WRITE(*,700) 100*TOTALTIME/MAXTIME
      ENDIF

      GOTO 58

100   CONTINUE

      CLOSE(801)
      CLOSE(802)

700   FORMAT(F7.2)
701   FORMAT(A)//
702   FORMAT(I10)//

      END//
```

The program writes two files - one containing the positions of the particles over MAXTIME time and another one containing timestamp, average horizontal kinetic energy per particle, average vertical kinetic energy per particle, average horizontal potential energy per particle, average vertical potential energy per particle.

A.2 Code for Simplified Model Simulation

```
      DOUBLE PRECISION PI,E
      INTEGER BNN

      PARAMETER (BNN=500)
      PARAMETER (PI=3.14159265358979323846264 3D0)
      PARAMETER (E=2.71828182845904523536028 74D0)
C
      DOUBLEPRECISION, ALLOCATABLE, DIMENSION(:) :: M
      DOUBLEPRECISION, ALLOCATABLE, DIMENSION(:,:) :: DELTAX,X,A,V,XOLD
      INTEGER, ALLOCATABLE, DIMENSION(:,:) :: IJARRAY

      DOUBLE PRECISION TOTALTIME,DELTAT
      DOUBLE PRECISION TEMPDIST
      DOUBLE PRECISION KV,KH,UNOT
      DOUBLE PRECISION TEMPGSUM,TEMPVEC(3),BETA,MAXTIME,FF,FA
      DOUBLE PRECISION SKN,FD,RAND1,RAND2,KEZ,KEXY,POTZ,POTR,POTI
      DOUBLE PRECISION TTERM,GAMMA,EPSILON,LAMBDA
      INTEGER ENDER
      INTEGER J,I,K,NPAR,STEPS,NEWPOS,WPOS
      INTEGER WRITER,WFREQ
      INTEGER, ALLOCATABLE :: SEED(:)
      INTEGER T,N,CLOCK

      N=1
      CALL RANDOM_SEED(SIZE=N)
      ALLOCATE(SEED(N))
      CALL SYSTEM_CLOCK(COUNT=CLOCK)
      SEED = 0.2*CLOCK+3*T
      CALL RANDOM_SEED(PUT=SEED)

      OPEN(800,FILE="tempin.dat",STATUS="OLD",ACTION="READ",
     *FORM="UNFORMATTED",ACCESS="STREAM")

      OPEN(801,FILE="dusty_positions.dat",STATUS="REPLACE",
     *ACTION="WRITE",FORM="UNFORMATTED",ACCESS="STREAM")
      CLOSE(801)

      OPEN(801,FILE="dusty_positions.dat",STATUS="OLD",ACTION="WRITE",
     *FORM="UNFORMATTED",ACCESS="STREAM",POSITION="APPEND")
```

```
      OPEN(802,FILE="dusty_energy.dat",STATUS="REPLACE",ACTION="WRITE",
     *FORM="UNFORMATTED",ACCESS="STREAM")
      CLOSE(802)

      OPEN(802,FILE="dusty_energy.dat",STATUS="OLD",ACTION="WRITE",
     *FORM="UNFORMATTED",ACCESS="STREAM",POSITION="APPEND")

      READ(800,END=9) NPAR,WFREQ,WPOS

      ALLOCATE(X(3,NPAR),A(3,NPAR),V(3,NPAR),XOLD(3,NPAR))
      ALLOCATE(DELTAX(3,NPAR),M(NPAR))
      ALLOCATE(IJARRAY(2,BNN*NPAR))

      READ(800,END=9) DELTAT,LAMBDA,KV,KH,UNOT,GAMMA,FD,FA,FF
      READ(800,END=9) MAXTIME,(M(I),I=1,NPAR),((X(J,I),J=1,3),I=1,NPAR)

9     CONTINUE

      CLOSE(800)

      TOTALTIME=0D0
      STEPS=0
      WRITER=1

      EPSILON=8.85D-12

10    CONTINUE

      SKN=0.5*3*LAMBDA


      A=0D0
      V=0D0

C     Contruct Neighbor Lists
13    CONTINUE

      A=0D0
      XOLD=X
      POTI=0D0
      POTR=0D0
      POTZ=0D0
```

```
      NEWPOS=1
      DO I=2,NPAR
         DO J=1,I-1
            TEMPVEC(:)=X(:,I)-X(:,J)
            TEMPDIST=DSQRT(TEMPVEC(1)*TEMPVEC(1)+TEMPVEC(2)*
     *      TEMPVEC(2)+TEMPVEC(3)*TEMPVEC(3))
            IF(TEMPDIST.GT.(SKN+3*LAMBDA)) CYCLE
            IJARRAY(1,NEWPOS)=I
            IJARRAY(2,NEWPOS)=J
            NEWPOS=NEWPOS+1
            IF(TEMPDIST.LT.(3*LAMBDA)) THEN
             POTI=POTI+(LAMBDA*UNOT)/(E**(TEMPDIST/LAMBDA)*TEMPDIST)+
     *       ((-15*LAMBDA+4*TEMPDIST)*UNOT)/(9.*E**3*LAMBDA)
             TEMPGSUM=-(((-4*TEMPDIST**2)/(E**3*LAMBDA) + (9*(LAMBDA +
     *        TEMPDIST))/E**(TEMPDIST/LAMBDA))*UNOT)/(9.*TEMPDIST**3)
              A(:,I)=A(:,I)-(TEMPVEC(:)*TEMPGSUM)/M(I)
              A(:,J)=A(:,J)+TEMPVEC(:)*TEMPGSUM/M(J)
            ENDIF
         ENDDO
      ENDDO

      CALL RANDOM_NUMBER(RAND1)
      CALL RANDOM_NUMBER(RAND2)
      RAND1=DSQRT(-2*DLOG(1-RAND1))*COS(2*PI*RAND2)
      DO I=1,NPAR

         POTR=POTR+0.5*KH*(X(1,I)**2+X(2,I)**2)
         POTZ=POTZ+0.5*KV*X(3,I)**2
         A(1,I)=A(1,I)-KH*X(1,I)/M(I)
         A(2,I)=A(2,I)-KH*X(2,I)/M(I)
         A(3,I)=A(3,I)-KV*X(3,I)/M(I)+
     *   RAND1*(FD+FA*SIN(2*PI*FF*TOTALTIME))/M(I)
         A(:,I)=A(:,I)-GAMMA*V(:,I)
      ENDDO

C     END construct neighbor list

C      IF(MOD(STEPS-1,50).EQ.0) WRITE(*,700) MAXVAL(ABS(DELTAX))

      IF(WRITER.EQ.0) THEN
         WRITER=1
```

```
         GOTO 70
       ENDIF

58     CONTINUE

       IF((MOD(STEPS,WFREQ).EQ.0).AND.(WPOS.EQ.1)) THEN
          WRITE(801) ((X(J,I),J=1,3),I=1,NPAR)
       ENDIF

       IF(MOD(STEPS,WFREQ).EQ.0) THEN
          KEXY=0D0
          KEZ=0D0
          DO I=1,NPAR
             KEXY=KEXY+0.5*M(I)*(V(1,I)**2+V(2,I)**2)
             KEZ=KEZ+0.5*M(I)*(V(3,I)**2)
          ENDDO
          WRITE(802) TOTALTIME,KEXY/NPAR,KEZ/NPAR,POTZ/NPAR,
      *   POTR/NPAR
       ENDIF

       X=X+DELTAT*V+(5D-1)*A*DELTAT**2
       V=V+A*DELTAT*5D-1
       DELTAX=ABS(X-XOLD)

       IF((MAXVAL(DELTAX).GE.(SKN/2D0)).OR.(MOD(STEPS+1,1000).EQ.0)) THEN
          WRITER=0
          GOTO 13
       ENDIF

       A=0D0
       POTI=0D0
       POTR=0D0
       POTZ=0D0

       DO K=1,NEWPOS-1
          I=IJARRAY(1,K)
          J=IJARRAY(2,K)
          TEMPVEC(:)=X(:,I)-X(:,J)
          TEMPDIST=DSQRT(TEMPVEC(1)*TEMPVEC(1)+TEMPVEC(2)*
      *   TEMPVEC(2)+TEMPVEC(3)*TEMPVEC(3))
          IF(TEMPDIST.GT.(3*LAMBDA)) CYCLE
            POTI=POTI+(LAMBDA*UNOT)/(E**(TEMPDIST/LAMBDA)*TEMPDIST)+
```

```
     *       ((-15*LAMBDA+4*TEMPDIST)*UNOT)/(9.*E**3*LAMBDA)
           TEMPGSUM=-(((-4*TEMPDIST**2)/(E**3*LAMBDA) + (9*(LAMBDA +
     *        TEMPDIST))/E**(TEMPDIST/LAMBDA))*UNOT)/(9.*TEMPDIST**3)
         A(:,I)=A(:,I)-(TEMPVEC(:)*TEMPGSUM)/M(I)
         A(:,J)=A(:,J)+TEMPVEC(:)*TEMPGSUM/M(J)
       ENDDO

       CALL RANDOM_NUMBER(RAND1)
       CALL RANDOM_NUMBER(RAND2)
       RAND1=DSQRT(-2*DLOG(1-RAND1))*COS(2*PI*RAND2)
       DO I=1,NPAR
         POTR=POTR+0.5*KH*(X(1,I)**2+X(2,I)**2)
         POTZ=POTZ+0.5*KV*X(3,I)**2
         A(1,I)=A(1,I)-KH*X(1,I)/M(I)
         A(2,I)=A(2,I)-KH*X(2,I)/M(I)
         A(3,I)=A(3,I)-KV*X(3,I)/M(I)+
     *   RAND1*(FD+FA*SIN(2*PI*FF*TOTALTIME))/M(I)
         A(:,I)=A(:,I)-GAMMA*V(:,I)
       ENDDO

70     CONTINUE

       V=V+A*DELTAT*5D-1

       STEPS=STEPS+1
       TOTALTIME=STEPS*DELTAT

C       IF(STEPS.GT.200) GOTO 100

       IF(TOTALTIME.GT.MAXTIME) GOTO 100

       IF(MOD(STEPS,WFREQ*500).EQ.0) THEN
         WRITE(*,700) 100*TOTALTIME/MAXTIME
       ENDIF

       GOTO 58

100    CONTINUE

       CLOSE(801)
       CLOSE(802)
```

```
700   FORMAT(F7.2)
701   FORMAT(A)
702   FORMAT(I10)

      END
```

The program writes two files - one containing the positions of the particles over MAXTIME time and another one containing timestamp, average horizontal kinetic energy per particle, average vertical kinetic energy per particle, average horizontal potential energy per particle, average vertical potential energy per particle.

A.3 Fortran Code for Stochastic Electric Field Oscillations

```
 PROGRAM Dynamics Dusty E-Field Fluctuations

       DOUBLE PRECISION PI,E
       INTEGER BNN

       PARAMETER (BNN=500)
       PARAMETER (PI=3.14159265358979323846264 3D0)
       PARAMETER (E=2.71828182845904523536028 74D0)
C
       DOUBLEPRECISION, ALLOCATABLE, DIMENSION(:) :: R,M,Q
       DOUBLEPRECISION, ALLOCATABLE, DIMENSION(:,:) :: DELTAX,X,A,V,XOLD
       INTEGER, ALLOCATABLE, DIMENSION(:,:) :: IJARRAY


       DOUBLE PRECISION TOTALTIME,DELTAT
       DOUBLE PRECISION TEMPDIST
       DOUBLE PRECISION VNORM,VOLT,VEF,CHIV,CHIH
       DOUBLE PRECISION TEMPGSUM,TEMPVEC(3),BETA, MAXTIME
       DOUBLE PRECISION SKN,FD,RAND1,RAND2,KEZ,KEXY,POTZ,POTR,POTI
C      define rigid body rotation om (omega)
       DOUBLE PRECISION GAMMA,ALPHA,EPSILON,DEN,GRAV,LAMBDA,QT
       INTEGER ENDER
       INTEGER J,I,K,NPAR,STEPS,NEWPOS,WPOS
       INTEGER WRITER,WFREQ
       INTEGER, ALLOCATABLE :: SEED(:)
       INTEGER T,N,CLOCK

       OPEN(800,FILE="tempin.dat",STATUS="OLD",ACTION="READ",
      *FORM="UNFORMATTED",ACCESS="STREAM")

       OPEN(801,FILE="dusty_positions.dat",STATUS="REPLACE",
      *ACTION="WRITE",FORM="UNFORMATTED",ACCESS="STREAM")
       CLOSE(801)

       OPEN(801,FILE="dusty_positions.dat",STATUS="OLD",ACTION="WRITE",
      *FORM="UNFORMATTED",ACCESS="STREAM",POSITION="APPEND")

       OPEN(802,FILE="dusty_energy.dat",STATUS="REPLACE",ACTION="WRITE",
```

```
     *FORM="UNFORMATTED",ACCESS="STREAM")
      CLOSE(802)

      OPEN(802,FILE="dusty_energy.dat",STATUS="OLD",ACTION="WRITE",
     *FORM="UNFORMATTED",ACCESS="STREAM",POSITION="APPEND")

      READ(800,END=9) NPAR,WFREQ,WPOS

      ALLOCATE(X(3,NPAR),A(3,NPAR),R(NPAR),V(3,NPAR),XOLD(3,NPAR))
      ALLOCATE(DELTAX(3,NPAR),M(NPAR),Q(NPAR))
      ALLOCATE(IJARRAY(2,BNN*NPAR))

      READ(800,END=9) DELTAT,LAMBDA,VOLT,VEF,CHIV
      READ(800,END=9) CHIH,GAMMA,ALPHA
      READ(800,END=9) MAXTIME,(R(I),I=1,NPAR),((X(J,I),J=1,3),I=1,NPAR)

9     CONTINUE

      CLOSE(800)

      TOTALTIME=0D0
      STEPS=0
      WRITER=1
      DEN=1510.0
      GRAV=9.81
      EPSILON=8.85D-12
      EL=1.6021766D-19
C

      N=1
      CALL RANDOM_SEED(SIZE=N)
      ALLOCATE(SEED(N))
      CALL SYSTEM_CLOCK(COUNT=CLOCK)
      SEED = 0.2*CLOCK+3*T
      CALL RANDOM_SEED(PUT=SEED)

      WRITE(*,700) ALPHA,GAMMA,VEF


10    CONTINUE

      SKN=0.5*3*LAMBDA
```

```
      DO I=1,NPAR
         M(I)=4*PI*DEN*R(I)**3/3
         Q(I)=4*EPSILON*PI*R(I)*VOLT
      ENDDO

      A=0D0
      V=0D0

C     Contruct Neighbor Lists
13    CONTINUE

      A=0D0
      XOLD=X
      POTI=0D0
      POTR=0D0
      POTZ=0D0

      NEWPOS=1
      DO I=2,NPAR
         DO J=1,I-1
            TEMPVEC(:)=X(:,I)-X(:,J)
            TEMPDIST=DSQRT(TEMPVEC(1)*TEMPVEC(1)+TEMPVEC(2)*
     *      TEMPVEC(2)+TEMPVEC(3)*TEMPVEC(3))
            IF(TEMPDIST.GT.(SKN+3*LAMBDA)) CYCLE
            IJARRAY(1,NEWPOS)=I
            IJARRAY(2,NEWPOS)=J
            NEWPOS=NEWPOS+1
           IF(TEMPDIST.LT.(3*LAMBDA)) THEN
             POTI=POTI+(4*EPSILON*PI*R(I)*R(J)*(9/(E**(TEMPDIST/LAMBDA)
     *       *TEMPDIST)+(-15*LAMBDA+4*TEMPDIST)/(E**3*LAMBDA**2))*
     *       VOLT**2)/9
               TEMPGSUM=(4*E**(-3-TEMPDIST/LAMBDA)*EPSILON*PI*R(I)*R(J)
     *       *(4*E**(TEMPDIST/LAMBDA)*TEMPDIST**2-9*E**3*LAMBDA*(LAMBDA
     *       +TEMPDIST))*VOLT**2)/(9*LAMBDA**2*TEMPDIST**3)
               A(:,I)=A(:,I)-(TEMPVEC(:)*TEMPGSUM)/M(I)
               A(:,J)=A(:,J)+TEMPVEC(:)*TEMPGSUM/M(J)
            ENDIF
         ENDDO
      ENDDO

      CALL RANDOM_NUMBER(RAND1)
      CALL RANDOM_NUMBER(RAND2)
```

```
      RAND1=DSQRT(-2*DLOG(1-RAND1))*COS(2*PI*RAND2)
      VEF1 = VEF*(1+ALPHA*RAND1)

      DO I=1,NPAR
         QT=Q(I)
         POTR=POTR+0.5*CHIH*QT*(X(1,I)**2+X(2,I)**2)
         POTZ=POTZ-(VEF1*X(3,I)-0.5*CHIV*X(3,I)**2)*QT+GRAV*M(I)*X(3,I)
         A(1,I)=A(1,I)-CHIH*QT*X(1,I)/M(I)
         A(2,I)=A(2,I)-CHIH*QT*X(2,I)/M(I)
         A(3,I)=A(3,I)-GRAV+(VEF1-CHIV*X(3,I))*QT/M(I)
         A(:,I)=A(:,I)-GAMMA*V(:,I)
      ENDDO

C     END construct neighbor list

C      IF(MOD(STEPS-1,50).EQ.0) WRITE(*,700) MAXVAL(ABS())

      IF(WRITER.EQ.0) THEN
         WRITER=1
         GOTO 70
      ENDIF

58    CONTINUE
C     writing stuff to a file
      IF((MOD(STEPS,WFREQ).EQ.0).AND.(WPOS.EQ.1)) THEN
         WRITE(801) ((X(J,I),J=1,3),I=1,NPAR)
      ENDIF

      IF(MOD(STEPS,WFREQ).EQ.0) THEN
         KEXY=0D0
         KEZ=0D0
         DO I=1,NPAR
            KEXY=KEXY+0.5*M(I)*(V(1,I)**2+V(2,I)**2)
            KEZ=KEZ+0.5*M(I)*(V(3,I)**2)
         ENDDO
         WRITE(802) TOTALTIME,KEXY/NPAR,KEZ/NPAR,
     *   POTR/NPAR,POTZ/NPAR,RAND1
      ENDIF

      X=X+DELTAT*V+(5D-1)*A*DELTAT**2
      V=V+A*DELTAT*5D-1
      DELTAX=ABS(X-XOLD)
```

```
 IF((MAXVAL(DELTAX).GE.(SKN/2D0)).OR.(MOD(STEPS+1,1000).EQ.0)) THEN
    WRITER=0
    GOTO 13
 ENDIF

 A=0D0
 POTI=0D0
 POTR=0D0
 POTZ=0D0

 DO K=1,NEWPOS-1
    I=IJARRAY(1,K)
    J=IJARRAY(2,K)
    TEMPVEC(:)=X(:,I)-X(:,J)
    TEMPDIST=DSQRT(TEMPVEC(1)*TEMPVEC(1)+TEMPVEC(2)*
*   TEMPVEC(2)+TEMPVEC(3)*TEMPVEC(3))
     IF(TEMPDIST.GT.(3*LAMBDA)) CYCLE
      POTI=POTI+(4*EPSILON*PI*R(I)*R(J)*(9/(E**(TEMPDIST/LAMBDA)
*       *TEMPDIST)+(-15*LAMBDA+4*TEMPDIST)/(E**3*LAMBDA**2))*
*       VOLT**2)/9
       TEMPGSUM=(4*E**(-3-TEMPDIST/LAMBDA)*EPSILON*PI*R(I)*R(J)
*       *(4*E**(TEMPDIST/LAMBDA)*TEMPDIST**2-9*E**3*LAMBDA*(LAMBDA
*       +TEMPDIST))*VOLT**2)/(9*LAMBDA**2*TEMPDIST**3)
    A(:,I)=A(:,I)-(TEMPVEC(:)*TEMPGSUM)/M(I)
    A(:,J)=A(:,J)+TEMPVEC(:)*TEMPGSUM/M(J)
 ENDDO

 CALL RANDOM_NUMBER(RAND1)
 CALL RANDOM_NUMBER(RAND2)
 RAND1=DSQRT(-2*DLOG(1-RAND1))*COS(2*PI*RAND2)
 VEF1 = VEF*(1+ALPHA*RAND1)
 DO I=1,NPAR
    QT=Q(I)
    POTR=POTR+0.5*CHIH*QT*(X(1,I)**2+X(2,I)**2)
    POTZ=POTZ-(VEF1*X(3,I)-0.5*CHIV*X(3,I)**2)*QT+GRAV*M(I)*X(3,I)
    A(1,I)=A(1,I)-CHIH*QT*X(1,I)/M(I)
    A(2,I)=A(2,I)-CHIH*QT*X(2,I)/M(I)
    A(3,I)=A(3,I)-GRAV+(VEF1-CHIV*X(3,I))*QT/M(I)
    A(:,I)=A(:,I)-GAMMA*V(:,I)
 ENDDO
```

```
70    CONTINUE

      V=V+A*DELTAT*5D-1

      STEPS=STEPS+1
      TOTALTIME=STEPS*DELTAT

C      IF(STEPS.GT.200) GOTO 100

      IF(TOTALTIME.GT.MAXTIME) GOTO 100

      IF(MOD(STEPS,WFREQ*500).EQ.0) THEN
         WRITE(*,700) 100*TOTALTIME/MAXTIME
      ENDIF

      GOTO 58

100   CONTINUE

      CLOSE(801)
      CLOSE(802)

700   FORMAT(F7.2)
701   FORMAT(A)
702   FORMAT(I10)

      END
```

The program writes two files - one containing the positions of the particles over MAXTIME time and another one containing timestamp, average horizontal kinetic energy per particle, average vertical kinetic energy per particle, average horizontal potential energy per particle, average vertical potential energy per particle.

Bibliography

[1] G. Gogia and J. C. Burton, Emergent bistability and switching in a nonequilibrium crystal, *Phys. Rev. Lett.*, **119**, 178004 (2017).

[2] F. F. Chen, J. D. Evans, and D. Arnush, A floating potential method for measuring ion density, *Physics of Plasmas*, **9**, 1449–1455 (2002).

[3] N. Goldenfeld and L. P. Kadanoff, Simple lessons from complexity, *Science*, **284**, 87–89 (1999).

[4] J.-R. Petit, J. Jouzel, D. Raynaud, N. I. Barkov, J.-M. Barnola, I. Basile, M. Bender, J. Chappellaz, M. Davis, G. Delaygue, et al., Climate and atmospheric history of the past 420,000 years from the vostok ice core, antarctica, *Nature*, **399**, 429 (1999).

[5] E. H. van Nes, W. J. Rip, and M. Scheffer, A theory for cyclic shifts between alternative states in shallow lakes, *Ecosystems*, **10**, 17 (2007).

[6] O. Reynolds, Xxix. an experimental investigation of the circumstances which determine whether the motion of water shall be direct or sinuous, and of the law of resistance in parallel channels, *Philos. Trans. Royal Soc.*, pages 935–982 (1883).

[7] O. Reynolds, On the dynamical theory of incompressible viscous fluids and the determination of the criterion., *Proc. R. Soc. Lond.*, **56**, 40 (1894).

[8] G. Gogia, W. Yu, and J. C. Burton, Intermittent "turbulence" in a many-body system (2019).

[9] K. Avila, D. Moxey, A. de Lozar, M. Avila, D. Barkley, and B. Hof, The onset of turbulence in pipe flow, *Science*, **333**, 192 (2011).

[10] M. Eckert, The troublesome birth of hydrodynamic stability theory: Sommerfeld and the turbulence problem, *The European Physical Journal H*, **35**, 29–51 (2010).

[11] G. I. Taylor, Stability of a viscous liquid contained between two rotating cylinders, *Proc. R. Soc. Lond.*, **223**, 289 (1923).

[12] S. Grossmann, D. Lohse, and C. Sun, High–reynolds number taylor-couette turbulence, *Annu. Rev. Fluid Mech.*, **48**, 53 (2016).

[13] J. Nikuradze, Laws of flow in rough pipes, *vDI Forschungsheft*, **361** (1933).

[14] L. D. Landau, in On the problem of turbulencevolume 44, page 311 (1944).

[15] E. Hopf, A mathematical example displaying features of turbulence, *Commun. Pure Appl. Math*, **1**, 303 (1948).

[16] A. N. Kolmogorov, The local structure of turbulence in incompressible viscous fluid for very large reynolds numbers, *Cr. Acad. Sci. URSS*, **30**, 301 (1941).

[17] N. Goldenfeld, Roughness-induced critical phenomena in a turbulent flow, *Phys. Rev. Lett.*, **96**, 044503 (2006).

[18] D. Ruelle and F. Takens, On the nature of turbulence, *Les rencontres physiciens-mathématiciens de Strasbourg-RCP25*, **12**, 1 (1971).

[19] M. J. Feigenbaum, The onset spectrum of turbulence, *Physics Letters A*, **74**, 375 (1979).

[20] J.-P. Eckmann, Roads to turbulence in dissipative dynamical systems, *Reviews of Modern Physics*, **53**, 643 (1981).

[21] J. P. Gollub and H. L. Swinney, Onset of turbulence in a rotating fluid, *Physical Review Letters*, **35**, 927 (1975).

[22] M. Lessen, S. G. Sadler, and T.-Y. Liu, Stability of pipe poiseuille flow, *The Physics of Fluids*, **11**, 1404–1409 (1968).

[23] I. J. Wygnanski and F. Champagne, On transition in a pipe. part 1. the origin of puffs and slugs and the flow in a turbulent slug, *Journal of Fluid Mechanics*, **59**, 281–335 (1973).

[24] I. Wygnanski, M. Sokolov, and D. Friedman, On transition in a pipe. part 2. the equilibrium puff, *Journal of Fluid Mechanics*, **69**, 283–304 (1975).

[25] Y. Pomeau, Front motion, metastability and subcritical bifurcations in hydrodynamics, *Physica D*, **23**, 3 (1986).

[26] H.-Y. Shih, T.-L. Hsieh, and N. Goldenfeld, Ecological collapse and the emergence of travelling waves at the onset of shear turbulence, *Nat. Phys.*, **12**, 245 (2016).

[27] W. Crookes, On radiant matter; a lecture delivered to the british association for the advancement of science, *American Journal of Science and Arts*, **18**, 241 (1879).

[28] L. Tonks and I. Langmuir, Oscillations in ionized gases, *Phys. Rev.*, **33**, 195 (1929).

[29] B. A. Smith, L. Soderblom, R. Batson, P. Bridges, J. Inge, H. Masursky, E. Shoemaker, R. Beebe, J. Boyce, G. Briggs, et al., A new look at the saturn system: The voyager 2 images, *Science*, **215**, 504 (1982).

[30] G. S. Selwyn, J. Singh, and R. Bennett, In situ laser diagnostic studies of plasma-generated particulate contamination, *J. Vac. Sci. Technol. A*, **7**, 2758 (1989).

[31] H. Setyawan, M. Shimada, Y. Hayashi, and K. Okuyama, Removal of particles during plasma processes using a collector based on the properties of particles suspended in the plasma, *J. Vac. Sci. Technol. A*, **23**, 388 (2005).

[32] J. Winter, Dust in fusion devices-experimental evidence, possible sources and consequences, *Plasma Phys. Control. Fusion*, **40**, 1201 (1998).

[33] J. Mahmoodi, P. K. Shukla, N. L. Tsintsadze, and D. D. Tskhakaya, Dispersion properties of a dusty plasma containing nonspherical rotating dust grains, *Phys. Rev. Lett.*, **84**, 2626–2629 (2000).

[34] P. N. Pusey and W. Van Megen, Phase behaviour of concentrated suspensions of nearly hard colloidal spheres, *Nature*, **320**, 340 (1986).

[35] H. Thomas, G. Morfill, V. Demmel, J. Goree, B. Feuerbacher, and D. Möhlmann, Plasma crystal: Coulomb crystallization in a dusty plasma, *Phys. Rev. Lett.*, **73**, 652 (1994).

[36] J. Chu and I. Lin, Direct observation of coulomb crystals and liquids in strongly coupled rf dusty plasmas, *Phys. Rev. Lett.*, **72**, 4009 (1994).

[37] A. Ivlev, H. Löwen, G. Morfill, and C. P. Royall, *Complex plasmas and colloidal dispersions: particle-resolved studies of classical liquids and solids* (World Scientific) (2012).

[38] U. Gasser, E. R. Weeks, A. Schofield, P. Pusey, and D. Weitz, Real-space imaging of nucleation and growth in colloidal crystallization, *Science*, **292**, 258 (2001).

[39] G. Joyce, M. Lampe, and G. Ganguli, Instability-triggered phase transition to a dusty-plasma condensate, *Physical review letters*, **88**, 095006 (2002).

[40] A. Melzer, A. Homann, and A. Piel, Experimental investigation of the melting transition of the plasma crystal, *Phys. Rev. E*, **53**, 2757 (1996).

[41] P. Kaplan, J. Rouke, A. Yodh, and D. Pine, Entropically driven surface phase separation in binary colloidal mixtures, *Phys. Rev. Lett.*, **72**, 582 (1994).

[42] C. Killer, T. Bockwoldt, S. Schütt, M. Himpel, A. Melzer, and A. Piel, Phase separation of binary charged particle systems with small size disparities using a dusty plasma, *Physical Review Letters*, **116**, 115002 (2016).

[43] P. Schall, I. Cohen, D. A. Weitz, and F. Spaepen, Visualization of dislocation dynamics in colloidal crystals, *Science*, **305**, 1944 (2004).

[44] V. Nosenko and S. Zhdanov, Dynamics of dislocations in a 2d plasma crystal, *Contrib. Plasm. Phys.*, **49**, 191 (2009).

[45] A. Piel and A. Melzer, Dynamical processes in complex plasmas, *Plasma Phys. Control. Fusion*, **44**, R1 (2001).

[46] J. Pieper and J. Goree, Dispersion of plasma dust acoustic waves in the strong-coupling regime, *Phys. Rev. Lett.*, **77**, 3137 (1996).

[47] R. Sakthivel, C. Chun, and J. Lee, New travelling wave solutions of burgers equation with finite transport memory, *Zeitschrift für Naturforschung A*, **65**, 633 (2010).

[48] R. W. Batterman and C. C. Rice, Minimal model explanations, *Philosophy of Science*, **81**, 349 (2014).

[49] A. Ross and D. McKenzie, Predator-prey dynamics stabilised by nonlinearity explain oscillations in dust-forming plasmas, *Scientific reports*, **6**, 24040 (2016).

[50] J. Schulze, B. Heil, D. Luggenhölscher, T. Mussenbrock, R. Brinkmann, and U. Czarnetzki, Electron beams in asymmetric capacitively coupled radio frequency discharges at low pressures, *J. Phys. D*, **41**, 042003 (2008).

[51] E. C. Whipple, Potentials of surfaces in space, *Rep. Prog. Phys*, **44**, 1197 (1981).

[52] P. K. Shukla and A. Mamun, *Introduction to dusty plasma physics* (CRC Press) (2015).

[53] C. Schmidt, O. Arp, and A. Piel, Spatially extended void-free dusty plasmas in a laboratory radio-frequency discharge, *Phys. Plasmas*, **18**, 013704 (2011).

[54] D. Block, J. Carstensen, P. Ludwig, W. J. Miloch, F. Greiner, A. Piel, M. Bonitz, and A. Melzer, Wake formation and wake field effects in complex plasmas, *Contributions to Plasma Physics*, **52**, 804 (2012).

[55] R. Kompaneets, G. E. Morfill, and A. V. Ivlev, Wakes in complex plasmas: A self-consistent kinetic theory, *Phys. Rev. E*, **93**, 063201 (2016).

[56] S. V. Vladimirov and M. Nambu, Attraction of charged particulates in plasmas with finite flows, *Phys. Rev. E*, **52**, R2172 (1995).

[57] A. Melzer, V. Schweigert, and A. Piel, Transition from attractive to repulsive forces between dust molecules in a plasma sheath, *Phys. Rev. Lett.*, **83**, 3194 (1999).

[58] M. Lampe, G. Joyce, G. Ganguli, and V. Gavrishchaka, Interactions between dust grains in a dusty plasma, *Phys. Plasmas*, **7**, 3851 (2000).

[59] A. Ivlev, J. Bartnick, M. Heinen, C.-R. Du, V. Nosenko, and H. Löwen, Statistical mechanics where newton's third law is broken, *Phys. Rev. X*, **5**, 011035 (2015).

[60] J. Goree, G. Morfill, V. Tsytovich, and S. Vladimirov, Theory of dust voids in plasmas, *Phys. Rev. E*, **59**, 7055 (1999).

[61] L. Couëdel, V. Nosenko, A. Ivlev, S. Zhdanov, H. Thomas, and G. Morfill, Direct observation of mode-coupling instability in two-dimensional plasma crystals, *Physical Review Letters*, **104**, 195001 (2010).

[62] B. Liu, J. Goree, V. Nosenko, and L. Boufendi, Radiation pressure and gas drag forces on a melamine-formaldehyde microsphere in a dusty plasma, *Phys. Plasmas*, **10**, 9 (2003).

[63] H. Rothermel, T. Hagl, G. E. Morfill, M. H. Thoma, and H. M. Thomas, Gravity compensation in complex plasmas by application of a temperature gradient, *Phys. Rev. Lett.*, **89**, 175001 (2002).

[64] P. Hargis Jr, K. Greenberg, P. Miller, J. Gerardo, J. Torczynski, M. Riley, G. Hebner, J. Roberts, J. K. Olthoff, J. Whetstone, et al., The gaseous electronics conference radio-frequency reference cell: A defined parallel-plate radio-frequency system for experimental and theoretical studies of plasma-processing discharges, *Rev. Sci. Instrum.*, **65**, 140 (1994).

[65] J. K. Olthoff and K. Greenberg, The gaseous electronics conference rf reference cell—an introduction, *J. Res. Natl. Inst. Stand. Technol.*, **100**, 327 (1995).

[66] C. A. Schneider, W. S. Rasband, and K. W. Eliceiri, Nih image to imagej: 25 years of image analysis, *Nature methods*, **9**, 671–675 (2012).

[67] D. Allan, T. Caswell, N. Keim, and C. van der Wel, trackpy: Trackpy v0.3.2. zenodo., *trackpy: Trackpy v0.3.2. Zenodo.* (2016).

[68] C.-R. Du, V. Nosenko, H. M. Thomas, Y.-F. Lin, G. E. Morfill, and A. V. Ivlev, Slow dynamics in a quasi-two-dimensional binary complex plasma, *Phys. Rev. Lett.*, **123**, 185002 (2019).

[69] A. V. Ivlev, U. Konopka, G. Morfill, and G. Joyce, Melting of monolayer plasma crystals, *Phys. Rev. E*, **68**, 026405 (2003).

[70] S. Zhdanov, A. Ivlev, and G. Morfill, Mode-coupling instability of two-dimensional plasma crystals, *Phys. Plasmas*, **16**, 083706 (2009).

[71] B. Liu, J. Goree, and Y. Feng, Mode coupling for phonons in a single-layer dusty plasma crystal, *Phys. Rev. Lett.*, **105**, 085004 (2010).

[72] L. Couëdel, S. Zhdanov, A. Ivlev, V. Nosenko, H. Thomas, and G. Morfill, Wave mode coupling due to plasma wakes in two-dimensional plasma crystals: In-depth view, *Phys. Plasmas*, **18**, 083707 (2011).

[73] T. Röcker, A. Ivlev, R. Kompaneets, and G. Morfill, Mode coupling in two-dimensional plasma crystals: Role of the wake model, *Phys. Plasmas*, **19**, 033708 (2012).

[74] NOAA, Magnetic field calculators (2020).

[75] J. Pavlu, A. Velyhan, I. Richterova, Z. Nemecek, J. Safrankova, I. Cermak, and P. Zilavy, Mass-loss rate for mf resin microspheres, *IEEE transactions on Plasma Science*, **32**, 704–708 (2004).

[76] T. Çağatay, M. Turcotte, M. B. Elowitz, J. Garcia-Ojalvo, and G. M. Süel, Architecture-dependent noise discriminates functionally analogous differentiation circuits, *Cell*, **139**, 512 (2009).

[77] C.-S. Wong, J. Goree, Z. Haralson, and B. Liu, Strongly coupled plasmas obey the fluctuation theorem for entropy production, *Nature Physics*, **14**, 21–24 (2018).

[78] S. Nunomura, T. Misawa, N. Ohno, and S. Takamura, Instability of dust particles in a coulomb crystal due to delayed charging, *Phys. Rev. Lett.*, **83**, 1970 (1999).

[79] A. Ivlev, U. Konopka, and G. Morfill, Influence of charge variation on particle oscillations in the plasma sheath, *Phys. Rev. E*, **62**, 2739 (2000).

[80] S. Takamura, T. Misawa, N. Ohno, S. Nunomura, M. Sawai, K. Asano, and P. Kaw, Dynamic behaviors of dust particles in the plasma–sheath boundary, *Phys. Plasmas*, **8**, 1886 (2001).

[81] A. Samarian, B. James, S. Vladimirov, and N. Cramer, Self-excited vertical oscillations in an rf-discharge dusty plasma, *Physical Review E*, **64**, 025402 (2001).

[82] O. Vaulina, A. Samarian, A. Nefedov, and V. Fortov, Self-excited motion of dust particles in a inhomogeneous plasma, *Physics Letters A*, **289**, 240–244 (2001).

[83] D. Resendes, G. Sorasio, and P. Shukla, Dynamics of dust particles in plasma sheaths, *Phys. Plasmas*, **9**, 2988 (2002).

[84] G. Sorasio, D. P. Resendes, and P. K. Shukla, Induced oscillations of dust grains in a plasma sheath under low pressures, *Phys. Lett. A*, **293**, 67–73 (2002).

[85] G. Sorasio, R. A. Fonseca, and D. P. Resendes, in P. K. Shukla, editor, Dust grain oscillation in plasma sheaths under low pressurespages 37–70 (Nova Science Publishers), 1st edition (2002).

[86] A. V. Ivlev, U. Konopka, and G. Morfill, Influence of charge variation on particle oscillations in the plasma sheath, *Phys. Rev. E*, **62**, 2739 (2000).

[87] M. Pustylnik, N. Ohno, S. Takamura, and R. Smirnov, Modification of the damping rate of the oscillations of a dust particle levitating in a plasma due to the delayed charging effect, *Phys. Rev. E*, **74**, 046402 (2006).

[88] V. Godyak, R. Piejak, and B. Alexandrovich, Measurement of electron energy distribution in low-pressure rf discharges, *Plasma Sources Sci. Technol.*, **1**, 36 (1992).

[89] V. Demidov, S. V. Ratynskaia, and K. Rypdal, Electric probes for plasmas: The link between theory and instrument, *Rev. Sci. Instrum.*, **73**, 3409 (2002).

[90] F. F. Chen, in Langmuir probe diagnosticsvolume 2 (2003).

[91] R. L. Merlino, Understanding langmuir probe current-voltage characteristics, *Am. J. Phys.*, **75**, 1078–1085 (2007).

[92] F. F. Chen, Langmuir probes in rf plasma: surprising validity of oml theory, *Plasma Sources Science and Technology*, **18**, 035012 (2009).

[93] K. Wiesemann, A short introduction to plasma physics, *arXiv preprint arXiv:1404.0509* (2014).

[94] A. Melzer and J. Goree, in R. Hippler, H. Kersten, M. Schmidt, and K. H. Schoenbach, editors, Fundamentals of dusty plasmaspages 157–206 (Wiley), 2nd edition (2008).

[95] T. Nitter, T. K. Aslaksen, F. Melandso, and O. Havnes, Levitation and dynamics of a collection of dust particles in a fully ionized plasma sheath, *IEEE T. Plasma Sci.*, **22**, 159–172 (1994).

[96] C. Zafiu, A. Melzer, and A. Piel, Measurement of the ion drag force on falling dust particles and its relation to the void formation in complex (dusty) plasmas, *Phys. Plasmas*, **10**, 1278 (2003).

[97] A. V. Ivlev, S. K. Zhdanov, S. A. Khrapak, and G. E. Morfill, Ion drag force in dusty plasmas, *Plasma Phys. Control. Fusion*, **46**, B267 (2004).

[98] I. L. Semenov, A. G. Zagorodny, and I. V. Krivtsun, Ion drag force on a dust grain in a weakly ionized collisional plasma, *Phys. Plasmas*, **20**, 013701 (2013).

[99] T. Nitter, Levitation of dust in rf and dc glow discharges, *Plasma Sources Sci. Technol.*, **5**, 93 (1996).

[100] A. Melzer, in Forces and trapping of dust particlespages 31–57 (Springer Nature, Switzerland AG) (2019).

[101] S. A. Khrapak, A. V. Ivlev, S. K. Zhdanov, , and G. E. Morfill, Hybrid approach to the ion drag force, *Phys. Plasmas*, **12**, 042308 (2005).

[102] L. Patacchini and I. H. Hutchinson, Fully self-consistent ion-drag-force calculations for dust in collisional plasmas with an external electric field, *Phys. Rev. Lett.*, **101**, 025001 (2008).

[103] S. Barnes, J. H. Keller, J. C. Forster, J. A. O'Neill, and D. K. Coultas, Transport of dust particles in glow-discharge plasmas, *Phys. Rev. Lett.*, **68**, 313 (1992).

[104] I. H. Hutchinson, Collisionless ion drag force on a spherical grain, *Plasma Phys. Control. Fusion*, **48**, 185 (2006).

[105] S. A. Khrapak, A. V. Ivlev, G. E. Morfill, and H. M. Thomas, Ion drag force in complex plasmas, *Phys. Rev. E*, **66**, 046414 (2002).

[106] E. Faudot, J. Ledig, J. Moritz, S. Heuraux, N. Lemoine, and S. Devaux, Experimental measurements of the rf sheath thickness with a cylindrical langmuir probe, *Phys. Plasmas*, **26**, 083503 (2019).

[107] S.-B. Wang and A. E. Wendt, Sheath thickness evaluation for collisionless or weakly collisional bounded plasmas, *IEEE Trans. Plasma Sci.*, **27**, 1358–1365 (1999).

[108] V. Land, L. S. Matthews, T. W. Hyde, and D. Bolser, Fluid modeling of void closure in microgravity noble gas complex plasmas, *Phys. Rev. E*, **81**, 056402 (2010).

[109] A. Douglass, V. Land, L. Matthews, and T. Hyde, Dust particle charge in plasma with ion flow and electron depletion near plasma boundaries, *Phys. Plasmas*, **18**, 083706 (2011).

[110] A. Douglass, V. Land, K. Qiao, L. Matthews, and T. Hyde, Determination of the levitation limits of dust particles within the sheath in complex plasma experiments, *Phys. Plasmas*, **19**, 013707 (2012).

[111] M. S. Benilov, The child–langmuir law and analytical theory of collisionless to collision-dominated sheaths, *Plasma Sources Sci. Technol.*, **18**, 014005 (2009).

[112] P. A. Miller and M. E. Riley, Dynamics of collisionless rf plasma sheaths, *J. Appl. Phys.*, **82**, 3689 (1997).

[113] A. Ivlev, R. Sütterlin, V. Steinberg, M. Zuzic, and G. Morfill, Nonlinear vertical oscillations of a particle in a sheath of a rf discharge, *Phys. Rev. Lett.*, **85**, 4060 (2000).

[114] T. S. Basha and A. Abbas, Charging times for dust particles in plasma, *Euro. J. Phys.*, **10**, 151 (1989).

[115] R. W. Batterman, Asymptotics and the role of minimal models, *The British Journal for the Philosophy of Science*, **53**, 21–38 (2002).

[116] U. Frisch, B. Hasslacher, and Y. Pomeau, Lattice-gas automata for the navier-stokes equation, *Phys. Rev. Lett.*, **56**, 1505 (1986).

[117] E. Bitzek, P. Koskinen, F. Gähler, M. Moseler, and P. Gumbsch, Structural relaxation made simple, *Phys. Rev. Lett.*, **97**, 170201 (2006).

[118] W. Kob and H. C. Andersen, Testing mode-coupling theory for a supercooled binary lennard-jones mixture i: The van hove correlation function, *Phys. Rev. E*, **51**, 4626 (1995).

[119] E. R. Weeks, Introduction to the colloidal glass transition, *ACS Macro Letters*, **6**, 27–34 (2017).

[120] M. Scheffer, J. Bascompte, W. A. Brock, V. Brovkin, S. R. Carpenter, V. Dakos, H. Held, E. H. Van Nes, M. Rietkerk, and G. Sugihara, Early-warning signals for critical transitions, *Nature*, **461**, 53 (2009).

[121] M. Scheffer, S. R. Carpenter, T. M. Lenton, J. Bascompte, W. Brock, V. Dakos, J. Van de Koppel, I. A. Van de Leemput, S. A. Levin, E. H. Van Nes, M. Pescual, and J. Vandermeer, Anticipating critical transitions, *Science*, **338**, 344–348 (2012).

[122] L. Dai, K. S. Korolev, and J. Gore, Slower recovery in space before collapse of connected populations, *Nature*, **496**, 355 (2013).

[123] S. Kefi, V. Guttal, W. A. Brock, S. R. Carpenter, A. M. Ellison, V. N. Livina, D. A. Seekell, M. Scheffer, E. H. van Nes, and V. Dakos, Early warning signals of ecological transitions: methods for spatial patterns, *PloS one*, **9**, e92097 (2014).

[124] T. J. Cline, D. A. Seekell, S. R. Carpenter, M. L. Pace, J. R. Hodgson, J. F. Kitchell, and B. C. Weidel, Early warnings of regime shifts: evaluation of spatial indicators from a whole-ecosystem experiment, *Ecosphere*, **5**, 1 (2014).

[125] F. A. Lindemann, The calculation of molecular vibration frequencies, *Phys. Z.*, **11**, 609–612 (1910).

[126] D. R. Nelson, *Defects and geometry in condensed matter physics* (Cambridge University Press) (2002).

[127] S. Henkes, C. Brito, and O. Dauchot, Extracting vibrational modes from fluctuations: a pedagogical discussion, *Soft Matter*, **8**, 6092 (2012).

[128] A. Bottinelli and J. L. Silverberg, How to: Using mode analysis to quantify, analyze, and interpret the mechanisms of high-density collective motion, *Front. Appl. Math.*, **3**, 26 (2017).

[129] J. C. Burton and S. R. Nagel, Echoes from anharmonic normal modes in model glasses, *Phys. Rev. E*, **93**, 032905 (2016).

[130] D. Mukamel, *Phase transitions in nonequilibrium systems* (2000).

[131] T. Li and M. G. Raizen, Brownian motion at short time scales, *Annalen der Physik*, **525**, 281–295 (2013).

[132] P. Bak, C. Tang, and K. Wiesenfeld, Self-organized criticality: An explanation of the 1/f noise, *Phys. Rev. Lett.*, **59**, 381 (1987).

[133] P. Bak, C. Tang, and K. Wiesenfeld, Self-organized criticality, *Phys. Rev. A*, **38**, 364 (1988).

[134] D. Schertzer, S. Lovejoy, F. Schmitt, Y. Chigirinskaya, and D. Marsan, Multifractal cascade dynamics and turbulent intermittency, *Fractals*, **5**, 427–471 (1997).

[135] L. Gammaitoni, P. Hänggi, P. Jung, and F. Marchesoni, Stochastic resonance, *Reviews of modern physics*, **70**, 223 (1998).

[136] R. Benzi, G. Parisi, A. Sutera, and A. Vulpiani, Stochastic resonance in climatic change, *Tellus*, **34**, 10 (1982).

[137] B. McNamara, K. Wiesenfeld, and R. Roy, Observation of stochastic resonance in a ring laser, *Phys. Rev. Lett.*, **60**, 2626 (1988).

[138] K. Wiesenfeld, D. Pierson, E. Pantazelou, C. Dames, and F. Moss, Stochastic resonance on a circle, *Physical Review Letters*, **72**, 2125 (1994).

[139] M. Perc, M. Gosak, and M. Marhl, Periodic calcium waves in coupled cells induced by internal noise, *Chem. Phys. Lett.*, **437**, 143–147 (2007).

[140] J. K. Douglass, L. Wilkens, E. Pantazelou, and F. Moss, Noise enhancement of information transfer in crayfish mechanoreceptors by stochastic resonance, *Nature*, **365**, 337 (1993).

[141] B. J. Gluckman, T. I. Netoff, E. J. Neel, W. L. Ditto, M. L. Spano, and S. J. Schiff, Stochastic resonance in a neuronal network from mammalian brain, *Phys. Rev. Lett.*, **77**, 4098 (1996).

[142] R. Nisbet and W. Gurney, A simple mechanism for population cycles, *Nature*, **263**, 319–320 (1976).

[143] O. N. Bjørnstad, R. M. Nisbet, and J.-M. Fromentin, Trends and cohort resonant effects in age-structured populations, *J. Anim. Ecol.*, **73**, 1157–1167 (2004).

[144] P. L. Chesson, Coexistence of competitors in spatially and temporally varying environments: a look at the combined effects of different sorts of variability, *Theoretical Population Biology*, **28**, 263–287 (1985).

[145] S. P. Hart, S. J. Schreiber, and J. M. Levine, How variation between individuals affects species coexistence, *Ecology letters*, **19**, 825–838 (2016).

[146] C. Boettiger, From noise to knowledge: how randomness generates novel phenomena and reveals information, *Ecology letters*, **21**, 1255–1267 (2018).

[147] A. J. Lotka, Contribution to the theory of periodic reactions, *The Journal of Physical Chemistry*, **14**, 271 (1910).

[148] V. Volterra, *Variazioni e fluttuazioni del numero d'individui in specie animali conviventi* (C. Ferrari) (1926).

[149] A. J. McKane and T. J. Newman, Predator-prey cycles from resonant amplification of demographic stochasticity, *Phys. Rev. Lett.*, **94**, 218102 (2005).

[150] R. R. Vance, Predation and resource partitioning in one predator–two prey model communities, *The American Naturalist*, **112**, 797–813 (1978).

[151] M. E. Gilpin, Spiral chaos in a predator-prey model, *Am. Nat.*, **113**, 306–308 (1979).

[152] E. N. Lorenz, Deterministic nonperiodic flow, *J. Atmos. Sci.*, **20**, 130–141 (1963).

[153] A. Hastings and T. Powell, Chaos in a three-species food chain, *Ecology*, **72**, 896–903 (1991).

[154] I. Koren and G. Feingold, Aerosol–cloud–precipitation system as a predator-prey problem, *Proceedings of the National Academy of Sciences*, **108**, 12227 (2011).

[155] M. J. Keeling, P. Rohani, and B. T. Grenfell, Seasonally forced disease dynamics explored as switching between attractors, *Physica D*, **148**, 317–335 (2001).

[156] P. L. Chesson and R. R. Warner, Environmental variability promotes coexistence in lottery competitive systems, *The American Naturalist*, **117**, 923–943 (1981).

[157] P. Foley, Predicting extinction times from environmental stochasticity and carrying capacity, *Conservation Biology*, **8**, 124–137 (1994).

[158] R. Kerswell, Recent progress in understanding the transition to turbulence in a pipe, *Nonlinearity*, **18**, R17 (2005).

[159] V. M. Uritsky, M. Paczuski, J. M. Davila, and S. I. Jones, Coexistence of self-organized criticality and intermittent turbulence in the solar corona, *Physical review letters*, **99**, 025001 (2007).

[160] Y. Pomeau, The long and winding road, *Nat. Phys.*, **12**, 198 (2016).

[161] D. Barkley, Theoretical perspective on the route to turbulence in a pipe, *J. Fluid Mech.*, **803** (2016).

[162] N. Goldenfeld and H.-Y. Shih, Turbulence as a problem in non-equilibrium statistical mechanics, *Journal of Statistical Physics*, **167**, 575–594 (2017).